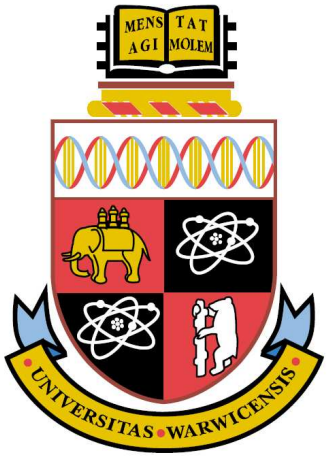

Heteroepitaxial growth of MnSb on III-V semiconductor substrates

by

Stuart Andrew Hatfield

Thesis

Submitted to the University of Warwick

for the degree of

Doctor of Philosophy

Department of Physics

December 2006

THE UNIVERSITY OF
WARWICK

Contents

Acknowledgments vi

Declarations vii

Abbreviations ix

Abstract xi

Chapter 1 Introduction 1

1.1 Background . . . 1

1.1.1 Spintronics . . . 1

1.1.2 Materials for spin injection . . . 2

1.2 Aims and organisation of thesis . . . 5

1.3 Conventions and notation . . . 6

1.3.1 Directions and planes . . . 6

1.3.2 Surface reconstruction notation . . . 7

1.3.3 Mono-layers and bi-layers . . . 9

1.3.4 Vacuum definitions . . . 9

1.4 Experimental techniques . . . 9

1.4.1 Ultra high vacuum . . . 9

1.4.2 Molecular beam epitaxy . . . 11

1.4.3 Reflection high energy electron diffraction . . . 15

1.4.4 X-ray photoelectron spectroscopy . . . 20

1.4.5 Scanning electron microscopy . . . 25

1.4.6 Scanning tunnelling microscopy . . . 27

1.5 Crystallography and surface structures of III-V semiconductors . . . 29
1.5.1 III-V semiconductor structure . . . 29
1.5.2 III-V surface reconstructions . . . 31
1.5.3 Electron counting . . . 33
1.6 Crystallography and surface structures of Manganese pnictides . . . 35
1.6.1 Manganese pnictide structure . . . 35
1.6.2 Literature search of Mn pnictide growth and structure . . . 36

Chapter 2 System design, commissioning and calibration 40
2.1 System overview . . . 40
2.2 Experimental Details . . . 41
2.2.1 Sample mounting and cleaning . . . 41
2.2.2 Tip etching . . . 43
2.2.3 Sample preparation for cross sectional scanning electron microscopy 44
2.3 Effusion cell calibrations . . . 44
2.4 Reflection high energy electron diffraction calibrations . . . 50
2.5 Epitaxial growth calibrations . . . 53
2.6 Scanning tunnelling microscope calibration . . . 56
2.7 Additional Systems . . . 58

Chapter 3 Heteroepitaxial growth of MnSb on GaAs 60
3.1 Introduction . . . 60
3.2 MnSb/GaAs(111)B . . . 61
3.2.1 Surface preparation of GaAs(111)B . . . 61
3.2.2 Growth of MnSb/GaAs(111)B . . . 63
3.2.3 Ex situ analysis of MnSb/GaAs(111)B . . . 67
3.3 Characterisation of MnSb/GaAs(111)B . . . 71
3.3.1 X-ray diffraction of MnSb/GaAs(111)B . . . 72
3.3.2 Magnetic measurements of MnSb/GaAs(111)B . . . 73
3.3.3 Valence band of MnSb/GaAs(111)B . . . 76
3.3.4 Growth mode of MnSb/GaAs(111)B . . . 77
3.4 MnSb/GaAs(001) . . . 83

3.5 Summary 85

Chapter 4 Surface structures of MnSb **86**

4.1 Introduction 86

4.2 MnSb(0001) 87

4.2.1 MnSb(0001) surface morphology 87

4.2.2 Scanning tunnelling microscopy imaging of MnSb(0001) surfaces 87

4.2.3 Surface reconstructions of MnSb(0001) 92

4.3 MnSb($1\bar{1}01$) 96

4.3.1 MnSb($1\bar{1}01$) surface morphology 96

4.3.2 Scanning tunnelling microscopy imaging of MnSb($1\bar{1}01$) surfaces 97

4.3.3 Surface reconstructions of MnSb($1\bar{1}01$) surfaces 99

4.4 Literature survey of relevant reconstructions 103

4.5 Discussion of structures for MnSb surfaces 106

4.5.1 Surface termination 106

4.5.2 Bonding configurations at surfaces 107

4.5.3 Modified electron counting 108

4.6 Models for MnSb(0001) surface reconstructions 110

4.7 Summary 113

Chapter 5 Heteroepitaxial growth of MnSb on InP(001) **114**

5.1 Introduction 114

5.2 Surface preparation of InP 116

5.3 Growth of MnSb/InP(001) 119

5.3.1 Experimental details 119

5.3.2 Growth surfaces and orientations 119

5.4 Ex situ analysis of MnSb/InP(001) samples 123

5.4.1 Microscopy of MnSb/InP(001) 123

5.4.2 Chemical analysis of MnSb/InP(001) 130

5.4.3 Growth modes and phase compositions 133

5.5 Summary 140

Chapter 6 Conclusions and future work **142**

6.1 Overview 142

6.2 Future work 144

Appendix A Growth rate equation **156**

Appendix B RHEEDprofile.m **158**

Appendix C MBE-STM system tasks **162**

Acknowledgments

The writing of this thesis and the work carried out in the past three (and a bit) years has only been possible with support from a number of people. The first thanks should go to Dr Gavin Bell, my supervisor, without whom neither this project nor MADGEneto (A.K.A **the** chamber) would exist. Gavin has taught me a great deal in the last three years, including the dark arts of ultra high vacuum, surface science and a stunning amount of obscure trivia! Most importantly (for this thesis at least), Gavin has 'encouraged' me to rediscover the correct use of the English language. He has also provided much amusement by denying the obvious similarity between Frank Zappa and Freddie Mercury.

In a place where equipment fails with neither reason nor warning, someone always ends up fixing lots of things lots of times. The place is the room of 422, and the man is Rob Johnston. Rob's unparalleled technical expertise has allowed MADGEneto to transcend from aluminium foil holder to data collection "giant". For this he is thanked, in addition to the copious quantities of tea he has provided, and the invention of gullibilium. I should also thank Prof. Chris McConville for his help, his Aladdin's cave of samples and convincing me to do a Physics PhD in the first place. My thanks also go to the other victims of the 422 curse: Marc, Matt and Marcus, for sharing my 'turbo-pump-slowing-down' paranoia as well as team HMC: Tim, Louis, Paul and Phil for "T". Extra thanks to Tim for answering my "this may be stupid but.." questions, and general LaTex wizardry. I am extremely grateful to Steve York, Dave Walker and Jenny Wooldridge for assistance with non UHV techniques.

A PhD (and life generally) would be pretty dull if there was no one to share a few civilized beverages with, and for that I thank all my friends from Warwick and elsewhere for pub O'clock, many games of pool and other much needed distractions.

The last thanks must go to my family, in particular my parents and grandparents for aid (financial and otherwise) throughout my (rather prolonged) academic career. Without all of you I could not have achieved any of this. Good news! I think that I am finally ready to leave Warwick and discover the world. Well...perhaps one more year...

Declarations

I declare that this thesis reports my research carried out in the Department of Physics at the University of Warwick between October 2003 and December 2006 under the Supervision of Dr G. R. Bell. The research reported here has not been submitted either wholly or in part in this or any other academic institution for admission to a higher degree.

The XRD data in Chapter 3 were obtained by Dr D. Walker, and the magnetic measurements carried out with the assistance of Ms J. Wooldridge. SEM images presented in Chapter 5 were obtained with the assistance of Mr S. York. All other experimental work and all data analysis were carried out by the author.

.....

Stuart Hatfield

December 2006

The work from this thesis has been presented in the following refereed journal and conferences.

- *Growth by molecular beam epitaxy and interfacial reactivity of MnSb on InP(001)* **S. A. Hatfield** and G. R. Bell *J. Cryst. Growth, Volume 296, November 2006, Pages 165-173*

- *Multiple phase formation during MBE growth of MnSb on InP* **S. A. Hatfield** and G. R. Bell *Poster presentation at the 14th international conference on molecular beam epitaxy , 3-8 September 2006, Waseda University, Tokyo, Japan*

- *Heteroepitaxial growth of MnSb on InP* **S. A. Hatfield** and G. R. Bell *Poster presentation at the Condensed Matter and Materials Physics conference, 20-21 April 2006, Exeter University, UK*

Work carried out by the author during this PhD, but not presented in this thesis has been published in the following refereed journal

- *Photoelectron spectroscopy study of $Ga_{1-x}Mn_xAs$(001) surface oxide and low temperature cleaning* **S. A. Hatfield**, T. D. Veal, C. F. McConville, G. R. Bell, K. W. Edmonds, R. P. Campion, C. T. Foxon, and B. L. Gallagher, *Surface Science, Volume 585, Issues 1-2, July 2005, Pages 66-74*

Abbreviations

2D ... Two dimensional

3D ... Three dimensional

AFM ... Atomic force microscope

BEP ... Beam equivalent pressure

BFG ... Beam flux gauge

DOS ... Density of states

DFT ... Density functional theory

DMS ... Dilute magnetic semiconductor

EDX ... Energy dispersive analysis of X-rays

FET ... Field effect transistor

FWHM ... Full width half maximum

GMR ... Giant magnetoresistance

HMF ... Half metallic ferromagnet

HWE ... Hot wall epitaxy

IBA ... Ion bombard and anneal

IMFP ... Inelastic mean free path

MBE ... Molecular beam epitaxy

MEC ... Modified electron counting

MRAM ... Magnetic random access memory

PLD ... Pulsed laser deposition

RHEED ... Reflection high energy electron diffraction

SEM ... Scanning electron microscopy

SQUID ... Superconducting quantum interference device

STM ... Scanning tunnelling microscope

TEM ... Transmission electron diffraction

TOA ... Take off angle

TSP ... Titanium sublimation pump

UHV ... Ultra high vacuum

VBM ... Valence band maximum

VSM ... Vibrating sample magnetometer

XPS ... X-ray photoelectron spectroscopy

XRD ... X-ray diffraction

Abstract

Heteroepitaxial growth of ferromagnetic MnSb on a variety of semiconducting III-V substrates has been investigated using a custom built MBE-STM system which has been commissioned and tested as part of this project. Characterisation of MnSb layers and their surface structures has been achieved using reflection high energy electron diffraction (RHEED), scanning tunnelling microscopy (STM), scanning electron microscopy (SEM), X-ray diffraction (XRD) and magnetic measurements.

Epitaxial MnSb was successfully grown on GaAs(111)B and (001) substrates. The growth rate and surface stoichiometry have a strong dependence on the beam equivalent pressure ratio ($J_{\mathrm{Sb/Mn}}$) of Sb and Mn. For $J_{\mathrm{Sb/Mn}}$<6, highly Mn rich surfaces are formed and the growth rate is Sb limited, whilst above $J_{\mathrm{Sb/Mn}} = 6$, near stoichiometric surfaces are formed. A set of standard growth conditions was defined ($J_{\mathrm{Sb/Mn}} = 8$, $T = 400$°C) which results in growth orientations of MnSb(0001) on GaAs(111)B substrates and MnSb($1\bar{1}01$) on GaAs(001). The MnSb(0001) layers have a ferromagnetic moment of 3.6 μ_{B} per Mn atom and a Curie temperature in excess of 400 K, in good agreement with bulk MnSb ($\mu = 3.5\ \mu_{\mathrm{B}}$, $T_{\mathrm{C}} = 587$ K). The initial growth mode of MnSb(0001)/GaAs(111)B was observed by RHEED and STM, and proceeds by nucleation and subsequent coalescence of flat topped 3D islands.

The MnSb(0001) and MnSb($1\bar{1}01$) surfaces exhibit a number of previously unreported surface reconstructions. On MnSb(0001) these reconstructions, ordered from Mn rich to Sb rich are: $(\sqrt{3} \times \sqrt{3})$R30°, $(2\sqrt{3} \times 2\sqrt{3})$R30°, (2×2), (1×1) and triple domain (1×4). On MnSb($1\bar{1}01$) a distorted (4×2) and a (1×2) symmetry are observed. The surface termination and bonding configurations at these surfaces are discussed in some detail and a number of models for the (2×2) and triple domain (1×4) proposed.

MnSb was also grown on the pseudo-lattice matched InP(001) substrate. The growth is hindered by the high chemical reactivity between the over-layer and substrate. At high growth temperatures (>300°C), multiple growth phases are observed by SEM, which are determined to be MnSb, prevalent at lower temperatures and $\mathrm{In}_{1-x}\mathrm{Mn}_x\mathrm{Sb}$ ($x \ll 1$) at higher temperatures. The presence of $\mathrm{In}_{1-x}\mathrm{Mn}_x\mathrm{Sb}$ indicates In out diffusion from the substrate, and is explained by comparisons to endotaxial growth of MnSb/GaSb in the literature. At temperatures $\sim$ 300°C a single MnSb phase is achieved with faint RHEED patterns indicating a growth orientation similar to MnSb($1\bar{1}00$). The quality of the over-layers grown in this single phase region is low compared to those grown on GaAs, with polycrystalline morphology and a rough interface observed by cross sectional SEM.

Chapter 1

Introduction

1.1 Background

1.1.1 Spintronics

The flow and manipulation of electronic charge in devices has been used for many years, with the invention of the transistor in 1947 at Bell Laboratories heralding the beginning of modern electronics [1]. It was not until recent decades that the possibility of using the spin of electrons in addition to the charge was considered. This important development led to spintronics (spin electronics), which has opened the way for a wide range of new device structures, in addition to improvements in power usage, speed and efficiency of existing devices. Some spin based electronic devices have already been incorporated into current technology. GMR (giant magnetoresistance) [2, 3] read heads were incorporated into commercial hard disks in 2000, while MRAM (magnetic random access memory) is well developed and will allow for high speed non-volatile data storage [4], with faster write speeds than the current non-volatile Flash memory, and without the rewrite fatigue problems. More sophisticated devices are envisaged, such as the spin valve [5], spin logic gates and entrapment of single electrons for quantum computing. It is highly desirable for these devices to be compatible with existing semiconductor technology, and as such many of these structures are likely to involve a combination of magnetic and semiconducting materials.

Three major requirements have been identified for the realisation of more advanced spin based semiconductor devices. These are

- 1. injection of spin polarised currents into a semiconductor based device
- 2. spin-coherent transport of spin polarised currents within semiconductors
- 3. manipulation and detection of spin polarised currents in devices

For the second requirement, the spin-coherent lifetime (the time before a spin polarised current becomes de-polarised due to scattering events) within the semiconductor must be sufficiently long to be used in a spintronic device. This has been studied by both experimental and theoretical techniques [6, 7]. In GaAs the spin-coherent lifetime is found to be sufficiently long for device purposes, and as such this requirement is generally believed to be solved. One caveat to this is that the lifetimes in different semiconductors are likely to be rather different, and for devices requiring III-V materials other than the well studied GaAs, problems may still arise. Requirement 3 necessitates a method by which the device can be used to affect a spin polarised current in order to achieve useful functionality, and subsequently to be able to detect the state of the polarised current. Spin polarised currents can be made to flow in exactly the same way as conventional currents by application of a longitudinal electric field, or made to precess by the application of a transverse electric field (the Rashba effect), as described by Datta and Das [8]. Preferential detection of spin polarised currents can be achieved using ferromagnetic contacts, while the polarisation of currents in a range of device structures has been analysed by electroluminescence [9, 10] and photoluminescence [11] of spin LED structures. Spin polarisation can also be measured by Andreev reflection, which detects the conductivity suppression of spin polarised currents through superconducting contacts [12, 13]. Detection and manipulation of spin polarised currents are therefore well developed. The final requirement for realisation of active spintronic devices is the injection of spin polarised currents into a semiconductor based device. While this can be achieved optically in III-Vs [6], a solid state method is desirable. This is considered to be the outstanding issue with regard to the development of spintronic devices, with no clear solution discovered to date.

1.1.2 Materials for spin injection

Electrons have an intrinsic spin, which can have two states, spin up ($s = \frac{1}{2}$) or spin down ($s = \text{-}\frac{1}{2}$). In an unpolarised current, the number of electrons in each spin state is equal. The number of spin up electrons with an energy E is expressed by the density of states (DOS) $N_{\uparrow}(E)$, and those with spin down by $N_{\downarrow}(E)$. Since current flow is the movement of electrons close to the Fermi level, the polarisation of a current P is

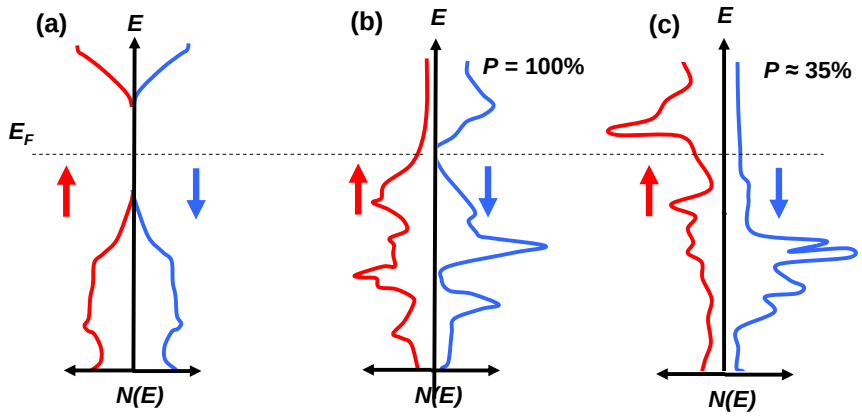

Figure 1.1: Spin up and spin down density of states for (a) a semiconductor (GaAs), (b) a half metallic ferromagnet (NiMnSb) and (c) a ferromagnet (MnSb). Reproduced from [14, 15, 16]

given by

$$P = \frac{N_{\uparrow}(E_F) - N_{\downarrow}(E_F)}{N_{\uparrow}(E_F) + N_{\downarrow}(E_F)} \tag{1.1}$$

In order to act as a source of spin polarised current, a solid state spin injector is required to have unequal spin up and spin down DOS at the Fermi level. Figure 1.1 shows the DOS for three classes of materials. Panel a illustrates an intrinsic semiconductor. The DOS at the Fermi level is zero, and current flow is only achieved by excitation of electrons from the filled valence band maximum (VBM) to the empty conduction band minimum (CBM). The definition of spin polarisation in Equation 1.1 is therefore undefined for an intrinsic semiconductor. A spin polarised current may be obtained if circularly polarised light is used to excite the electrons of one spin state preferentially, although this is not a solid state method. Panel b shows a half metallic ferromagnetic (HMF) material, an example of which is the semi-heusler alloy NiMnSb [17]. HMFs demonstrate a metallic DOS for spin up (majority spin), and a semiconducting DOS for spin down (minority spins). As a result of this unusual band structure, HMFs demonstrate 100% spin polarisation at the Fermi level. The third material illustrated in panel c is a ferromagnet, in which the spin up and spin down DOS are different due to the exchange interaction between spins. As a result these materials exhibit an overall magnetic moment as well as spin polarisation at the Fermi level.

Four types of ferromagnetic materials are identified for potential spin injection: dilute magnetic semiconductors (DMS), ferromagnetic metals, ferromagnetic alloys and

half metallic ferromagnets. DMSs are formed by doping III-V semiconductors with magnetic atoms such as Mn. In $Ga_{1-x}Mn_xAs$, the Mn takes up a substitutional Ga site and acts as an acceptor. The resulting holes mediate the ferromagnetism in the material [18]. The main advantage of DMS spin injectors is the obvious epitaxial compatibility with non-magnetic semiconductors in addition to the high degree of spin polarisation. Currents with $>$50% spin polarisation have been demonstrated for DMS spin injectors at low temperatures [19, 20]. The principle disadvantage of DMS materials is the currently low Curie temperatures, well below room temperature [21].

The other three injection materials would act as part of a hybrid system, in which non-semiconductor spin injectors are combined with semiconductors. A wide range of materials exist with suitable spin polarisation, including ferromagnetic metals such as Fe, ferromagnetic alloys, such as oxides (CrO_2) and pnictides (MnAs, MnSb), and HMFs such as NiMnSb. These materials demonstrate ferromagnetism with high Curie temperatures. In general, metals are more difficult to form epitaxially due to chemical intermixing at the interface [22]. With metals it is also hard to form inverse interfaces, where a semiconductor over-layer is grown onto a ferromagnet.

A number of problems exist for hybrid spintronic devices, arising as a result of the considerable structural, electronic and chemical differences between the injection material and the semiconductor. One universal problem for hybrid systems is the mechanism for spin injection. As a result of the conductivity mismatch between ferromagnetic materials and semiconductors, diffusive transport via ohmic contacts results in a dramatic reduction in spin polarisation. For MnSb ($\sigma_{MnSb} = 15.3\times10^6\ \Omega^{-1}\ m^{-1}$ [23]), the conductivity is a factor of $\sim$ 10 greater than that of typical III-V semiconductors ($\sigma_{GaAs} = 1.3\times10^5\ \Omega^{-1}\ m^{-1}$ [24]). In this case the majority of the voltage drop across a hybrid device will be over the semiconductor, resulting in mainly unpolarised current [25]. Injection through a Schottky barrier or tunnelling junction are believed to provide a solution to this problem, as demonstrated by Zhu *et al.* [10]. Other potential problems such as epitaxial compatibility and chemical stability at the interface vary from material to material.

A considerable body of work exists on the heteroepitaxial growth of MnAs on III-V materials for spin injection purposes, which is summarised in Section 1.6.2. MnAs is a ferromagnetic pnictide, with a Curie temperature above room temperature, and

a structure which is compatible with III-V(111) surfaces. Less work exists on MnSb, despite it appearing superior for spintronic purposes in a number of respects. While the Curie temperature of MnAs is only marginally above room temperature (318 K), that of MnSb is significantly higher at 587 K. This could be highly important for an on-chip device which may be heated by the surrounding electronics. In addition, MnAs has a structural phase transition between room temperature and typical growth temperatures, which is likely to lead to additional growth and processing problems. MnSb has only one structural phase in the relevant temperature and pressure ranges for MBE and processing.

1.2 Aims and organisation of thesis

Heteroepitaxial growth of MnSb over-layers on semiconductor substrates is the focus of this thesis. As already discussed, a number of issues must be resolved if MnSb is to be useful for spintronics. This work represents preliminary investigations into the structural aspects of the problem, namely the issues of epitaxial compatibility, interfacial and surface structures and chemical stability. The work was carried out using a custom built ultra high vacuum (UHV), molecular beam epitaxy (MBE) system.

The thesis is set out as follows. In this first chapter, experimental, theoretical and materials considerations are presented, with a summary of Mn pnictide epitaxial growth literature in Section 1.6.2. The UHV system used for this thesis was commissioned during this thesis, and as a result, a considerable proportion of the project was involved with calibration and optimisation of the system. The more important aspects of these calibrations are presented in Chapter 2. Chapter 3 deals with a heteroepitaxial study of MnSb on GaAs substrates. Although this combination has been studied by various groups, it is important to ensure that the new UHV system operates as expected, and to gain crucial experience with growth of this material. Chapter 4 presents work on surface structures and reconstructions of two MnSb surfaces grown on GaAs. These surface structures are expected to be highly important for inverse (semiconductor on ferromagnet) interface formation, in addition to being of general interest as a surface science study. The final experimental chapter, Chapter 5 presents a growth study of a previously unreported materials system, MnSb on InP. In Chapter 6, conclusions from

this project are drawn, and future work is discussed.

1.3 Conventions and notation

Throughout the literature of surface science and crystallography, a wide range of notations and conventions are used by different groups which make direct comparisons of sources problematic. For clarity, this section summarises the conventions and notations used throughout this thesis, highlighting variations used elsewhere.

1.3.1 Directions and planes

In this work, two crystal structures are studied. III-V materials exhibit the cubic zincblende structure (Figure 1.14), while MnSb has the hexagonal close packed NiAs structure (Figure 1.16). When referring to crystallographic directions either in the bulk or on the surface of these structures, a certain degree of ambiguity arises as a result of the numerous symmetry axes and equivalent directions. When dealing with surfaces it is particularly important to be precise regarding what constitutes a family of directions or planes. Since a surface represents a break in the bulk periodicity, families of directions on surfaces contain fewer members than in the 3D periodic bulk. For example, on a III-V semiconductor (001) surface, there is only two fold symmetry, and as such $<110>$ includes only [110] and its inverse $[\bar{1}\bar{1}0]$, but not [101] or [011] which both lie out of plane. Similarly $<1\bar{1}0>$ includes $[1\bar{1}0]$ and $[\bar{1}10]$. These two families are not equivalent as a result of the different bond directions of the atoms, and results in very different surface reconstructions. In various papers, the $\{001\}$ surfaces are typically labelled either (001) or (100). In this thesis, the plane is always defined as (001), with [100] and [010] directions lying in the plane. These should be labelled such that they obey a right handed basis set $[001]=[100]\wedge[010]$.

For the hexagonal NiAs structure, a four index system is commonly used. For NiAs structures the [ijkl] notation has three symmetrically identical directions ([i000], [0j00], [00k0]) in the hexagonal close packing plane, each rotated by 120° from the previous one. As a result of these non-orthogonal unit vectors, there are various ways of expressing the same direction in the close packed plane. The fourth direction, [000l], corresponds to the non-equivalent c axis perpendicular to the other three. It is essential

therefore not to confuse [0001], along which the lattice parameter is c, with [1000] along which it is a. In order to emphasise the inequivalence of these two, many groups write all directions in the hexagonal close packing plane as a combination of two or more of the in-plane directions. For example, [1000] may be written as $[2\bar{1}\bar{1}0]$. This convention prevents misunderstanding, and has been used throughout this thesis.

1.3.2 Surface reconstruction notation

Reconstructions form on surfaces in order to minimise surface energy, and result in tessellating structures covering the surface. These reconstructions are denoted by the distance over which atoms in identical chemical environments occur, also indicating the size of the tessellating structure. This is generally referred to as the periodicity of the surface. For an unreconstructed surface, this is the primitive unit mesh, described by the surface unit vectors $\underline{a_1}$ and $\underline{a_2}$. Two different notations may be used to represent the surface reconstructions. For a surface reconstruction described by the vectors $\underline{b_1}$ and $\underline{b_2}$, the relationship may be described as

$$\underline{b_1} = G_{11}\underline{a_1} + G_{12}\underline{a_2} \tag{1.2}$$

$$\underline{b_2} = G_{21}\underline{a_1} + G_{22}\underline{a_2} \tag{1.3}$$

The matrix G is defined

$$\mathbf{G} = \begin{pmatrix} G_{11} & G_{12} \\ G_{21} & G_{22} \end{pmatrix} \tag{1.4}$$

This matrix notation allows for any reconstruction to be defined [26], although it is somewhat cumbersome for the majority of simple surface reconstructions. A more convenient form is the Wood notation [27], in which the reconstructed surface symmetry is more closely related to that of the surface. In this case, the reconstruction is denoted (n×m), where

$$\underline{b_1} = n\underline{a_1} \tag{1.5}$$

and

$$\underline{b_2} = m\underline{a_2} \tag{1.6}$$

A number of extensions exist for the Wood notation. Centred (n×m), or c(n×m) has identical atomic environments on the corners of an (n×m) cell, as well as at the center of

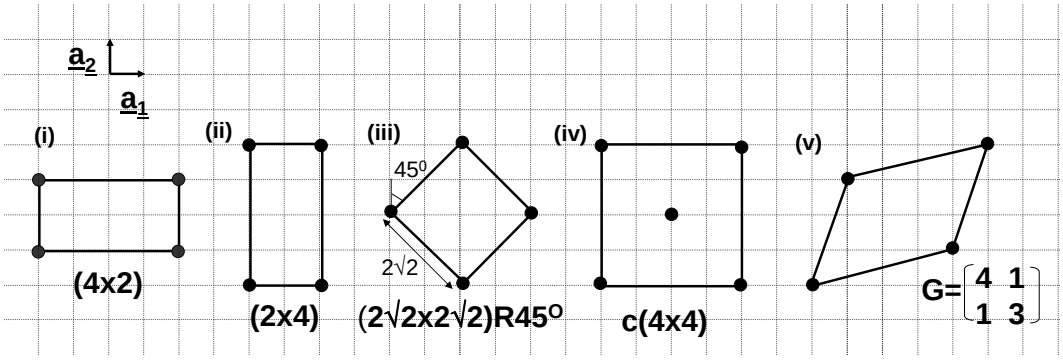

Figure 1.2: Reconstruction notations on a square lattice. The underlying lattice indicates the unreconstructed surface mesh. Black circles indicate identical chemical environments in the reconstruction. Reconstruction (v) is labelled with the matrix notation.

the cell. (n×m)Rθ is an (n×m) cell, rotated by θ from the surface unit mesh. Examples of these notations are shown in Figure 1.2.

For surfaces which demonstrate multiple domains, the notation $(n_1 \times m_1)/(n_2 \times m_2)$ may be used for the majority of cases on (001) surfaces. An example is the c(4×4)/a(1×3) transition region in the InSb(001) surface phase diagram (Figure 2.10) in which the two phases co-exist. For triple domains typical on hexagonal surfaces this notation is insufficient. Triple domains on hexagonal surfaces consist of identical reconstructions, each rotated by 120° from the previous one. This arises as a result of the three fold symmetry of the surface. In this thesis the notation td(n×m) is used to represent such a triple domain structure of (n×m). No analogous reconstruction arises on the (001) surface, since the surface is only two fold symmetric, and any double domains would be co-linear, and impossible to distinguish. Any (n×m)/(m×n) reconstructions on an (001) surface are required to have different reconstructions as a result of the different bonding directions.

A new surface reconstruction notation is used in this thesis. A distorted (n×m) or dis(n×m) is defined in Chapter 4. This reconstruction has similar dimensions to a (n×m), but with slightly different angles. This notation has been used in conjunction with matrix notation which describes the reconstruction completely. Examples of various simple reconstructions on a square lattice are illustrated in Figure 1.2. Reconstructions (i)-(iv) are labelled with the Wood notation, while (v) must be labelled with the matrix notation. Throughout this thesis the Wood notation is used, unless otherwise stated. It should be noted that reconstructions (iii) and (iv) in Figure 1.2 are equivalent.

1.3.3 Mono-layers and bi-layers

The use of the terms mono-layers and bi-layers can cause a certain amount of confusion if not properly defined. In this thesis mono-layer is used to define one layer of the material in question. One mono-layer of In for example refers to one atomic layer of In. One mono-layer of InSb refers to one mono-layer of In and one mono-layer of Sb. In the same way, a bi-layer is two mono-layers using the same convention. This distinction is particularly important for MnSb, since the unit cell in the c axis contains two inequivalent mono-layers of MnSb. Therefore a mono-layer of MnSb(0001) has a thickness of c/2.

1.3.4 Vacuum definitions

The terms in situ and ex situ have been used in this thesis according to the following definitions. In situ refers to events and techniques occurring within the growth system, and hence prior to any form of oxidation due to sample transfer between systems. Ex situ therefore refers to events outside the growth system although these experiments may still be in vacuo (under vacuum).

1.4 Experimental techniques

In this section the theory of the principle experimental techniques used throughout this thesis is presented. In addition, X-ray diffraction (XRD), a superconducting quantum interference device (SQUID) and vibrating sample magnetometer (VSM) are used in Chapter 3 for ex situ measurements. A brief description of the operation of these devices can be found in the relevant sections of Chapter 3.

1.4.1 Ultra high vacuum

Ultra high vacuum (UHV), with pressures of the order of 10^{-10} mbar, is essential for molecular beam epitaxy, for the formation of the molecular beams, in addition to preventing incorporation into the growth layer of atmospheric molecules such as O and C. Similarly, the majority of surface science techniques require UHV since even sub mono-layer quantities of atmospheric contaminants can seriously hinder or prevent entirely characterisation of the surface.

UHV systems can be pumped from atmospheric pressure (10^3 mbar) to roughing pressures ($\sim 10^{-3}$ mbar) using mechanical rotary pumps, which pump by compression and extraction of gas by oil sealed rotors. Pumping below 10^{-3} mbar requires pumps which do not rely upon viscous flow of gases, but instead molecular flow which is applicable at high vacuum. In molecular flow, the mean free path of the molecules is greater than the chamber dimensions, and the motion is dominated by molecules recoiling off the walls of the chamber with little or no interaction between each other [28]. High vacuum pressures of the order of 10^{-8} mbar can be achieved using a range of pumps. Turbomolecular pumps (turbo pumps) consist of a series of angled aluminium rotors spinning at high speed ($\sim$ 75 krpm). These spinning rotors skew the velocity distribution of desorbed molecules from the blades, with the net result of moving molecules towards a backing line pumped by a rotary pump, and away from the main chamber [28]. Ion pumps contain a number of parallel steel cylindrical anodes (Penning cells), with an array of thin titanium cathodes at the ends. A large magnetic field is applied parallel to the anodes, and a high voltage ($\sim$ 6kV) is applied to the electrodes. Electrons emitted from the anode are trapped in circular paths within the cylinders and so travel a distance greatly in excess of the mean free path, and ionise gas molecules in the cylinders. The ionised molecules are accelerated towards the cathode, and sputter titanium onto the pump surfaces. The ions become embedded in the titanium covered walls and eventually become buried by further sputtering events. In this manner, molecules are trapped on the surfaces of the pump, which results in a reduction in chamber pressure. In addition to pumping, the cathode current gives an indication of the number of ionisation events, and so ion pumps also act as pressure gauges [28]. A final pumping method is the combination of a cold trap with a titanium sublimation pump (TSP). The cold trap is an area of the chamber which is cooled by liquid nitrogen. At this lowered temperature, adsorbed molecules spend a longer time on the surface. The TSP is a heated filament of titanium, which sublimates titanium to cover the surfaces surrounding it, including the cold trap. This titanium buries adsorbed molecules, and acts as a 'sticky' surface, holding more molecules to the surface [28]. Using these pumping methods, pressures of the order of 10^{-8} mbar may be routinely achieved, after which the pressure is limited by the desorption of atmospheric gases, in particular H_2O, from the internal walls of the chamber. In order to reduce this effect, the chamber must be baked. During baking, the

entire chamber is heated to 150-200$^{\circ}C$ in order to desorb the atmospheric gases from the inner walls of the chamber. This results in an initial increase in chamber pressure during the desorbtion, which then reduces as the gases are pumped away. Upon cooling, the ultimate pressure of the chamber is improved, and pressures of 10^{-10}-10^{-11} mbar can be achieved.

1.4.2 Molecular beam epitaxy

III-V molecular beam epitaxy (MBE), first successfully achieved by Cho and Arthur in the later 1960's allows for in situ growth of ultra thin layers of crystalline material upon a substrate of the same (homoepitaxy) or different (heteroepitaxy) material [29]. The technological uses for growth and combination of semiconductor materials on atomic scales are vast, allowing for fabrication of opto-electronic devices such as light emitting diodes (LEDs) and laser structures. The main advantages of MBE are the ability to control the layer thickness of materials on the atomic scale, independent control of growth rate and substrate temperature and the ability to tailor lattice parameters and structures by the choice of substrate material.

MBE is a UHV technique, requiring vacuum to prevent contamination of the growth surface, and for the formation of the molecular beams which gives the technique its name. MBE is achieved by the incidence of one or more molecular beams, generated in effusion cells, upon a substrate material. An effusion cell consists of a heated crucible containing the source material which sublimates or evaporates to form a molecular beam. Materials display a temperature dependent vapor pressure, expressed by the Clausius-Clapeyron equation.

$$P = A\exp\left(\frac{-\Delta H}{RT}\right) \tag{1.7}$$

P is the beam equivalent pressure (BEP) measured by a gauge in the path of the molecular beam (a beam flux gauge, BFG). This is dependent upon ΔH the enthalpy of evaporation or sublimation as appropriate, R, the molar gas constant and the absolute temperature of the source material T.

The molecular beam is directed at the substrate material. The arrival rate r of an isotropic gas, pressure P, on a surface is expressed by the following equation, where m defines the mass of the atoms/molecules in the molecular beam, and all values are

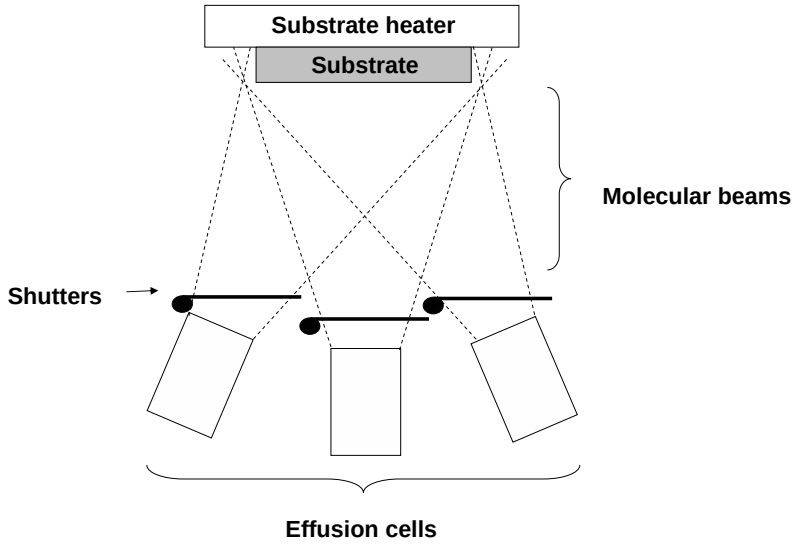

Figure 1.3: Schematic of the MBE setup

in SI units [30, 31].

$$r = \frac{1}{\sqrt{2\pi}} \frac{P}{\sqrt{k_{\mathrm{B}} T m}} \tag{1.8}$$

A modified version of this equation is used to express the arrival rate from a highly directional molecular beam with BEP P, and is derived fully in Appendix A.

$$r = \frac{4}{\sqrt{2\pi}} \frac{P}{\sqrt{k_{\mathrm{B}} T m}} \tag{1.9}$$

Using shutters or valves, the beams can be interrupt as required, and the growth halted. A schematic of the MBE setup is shown in Figure 1.3. The substrate is heated by a heating element behind the sample, allowing for various growth temperatures to be achieved.

At the substrate surface, the arriving atoms or molecules of the source materials can undergo a number of processes, summarised in Figure 1.4 [31]. Atoms weakly bound to the surface by van der Waals forces are said to be physisorbed, while those bound to the substrate by stronger chemical bonds are said to be chemisorbed. To become incorporated into the lattice, an atom must become chemisorbed at an epitaxial site and form bulk-like bonding configurations. The rate at which this occurs is the

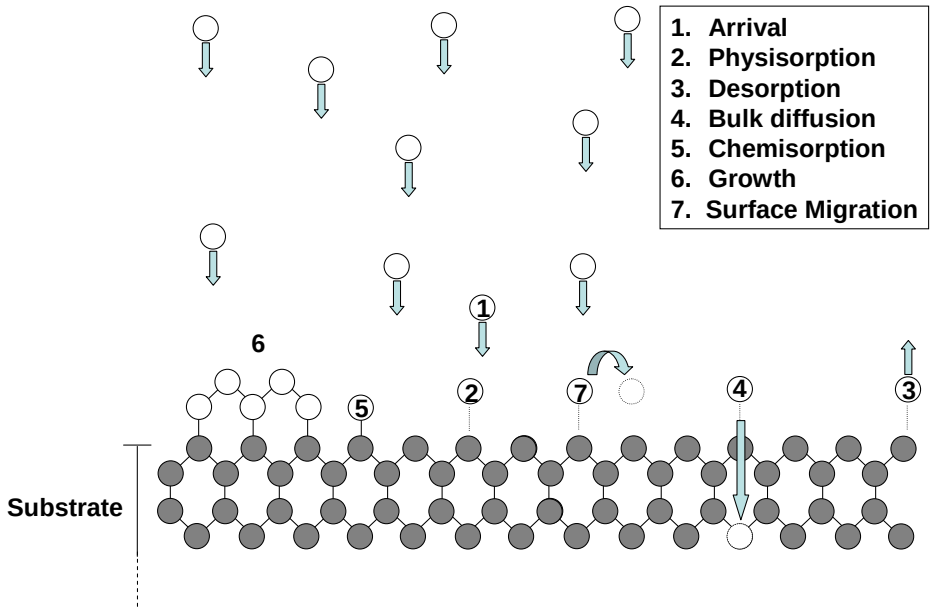

Figure 1.4: Illustration of some of the atomistic processes occurring during MBE

incorporation rate. Atoms and molecules may migrate across the surface, desorb back into the vacuum, or migrate into the crystal itself. Reactions between adatoms can occur as well, and this can be a crucial stage for breaking up large molecules. The rate of each of these processes (R) can be expressed by a barrier height for the particular process E_{b} and surface temperature T by the following expression.

$$R = \nu_0 \exp\left(\frac{-E_{\mathrm{b}}}{k_{\mathrm{B}}T}\right) \tag{1.10}$$

Here ν_0 is the attempt frequency which is associated with the lateral vibration frequency of the adatom (typically 10^{13} s^{-1}), and the other symbols have their usual meanings. Typical migration barriers on GaAs are $\sim$ 1eV.

The formation of new material by chemisorption and incorporation may result in a number of different growth modes, dependent upon a number of factors such as growth temperature, strain and surface energies of the different materials. Ideally for high quality interfaces, layer by layer growth is desirable, in which each growing atomic layer is completed before the next begins to grow. This is illustrated by the idealised Frank-van der Merwe growth mode shown in Figure 1.5a. Two other ideal growth modes are the 3D island (Volmer-Weber) and island plus wetting layer (Stranski-Krastanov)

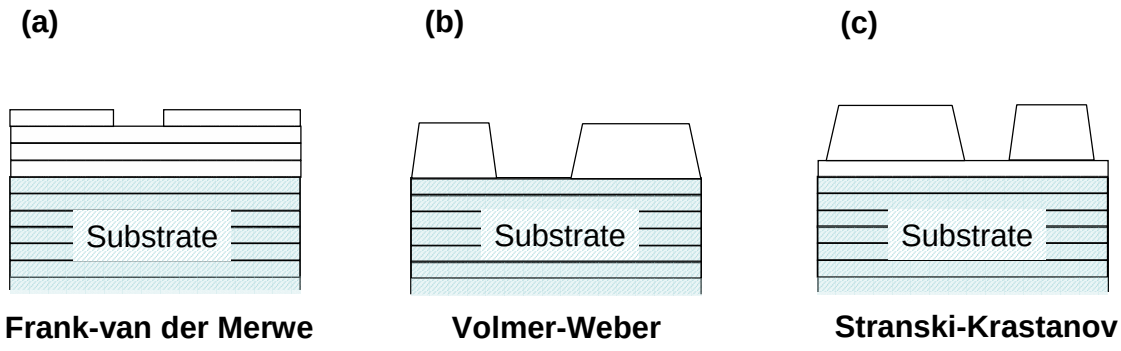

Figure 1.5: Ideal crystal growth modes, showing (a) Frank-van der Merwe (Layer-by-layer) growth, (b) Volmer-Weber (island) growth and (c) Stranski-Krastanov (layer plus island) growth modes [31, 34].

growth modes, also illustrated in Figure 1.5. In fact, growth modes are rather more complicated than these models. Many variations on the idealised models exist, such as coherent or incoherent 3D island growth, or layer-by-layer growth with strain relief by dislocations or large scale rippling. Another growth mode, termed endotaxy involves the growth of oriented crystallites *into* the substrate as a result of high chemical reactivity between the over-layer and substrate [32, 33]. This growth mode is discussed in more detail in Chapter 5.

In MBE, a number of parameters are involved in determining the quality, speed and mode of the growth. One previously mentioned is the rates of various processes such as migration, incorporation or reaction between different elemental species. These in turn are dependent upon the substrate temperature (T), in addition to the relative and absolute abundance of the growth elements, determined by the appropriate beam fluxes. A second parameter is the chemical potential at the surface, which again is closely linked to the BEP ratio (J) of the source materials in addition to the relative desorption rates at the growth temperature. A third parameter, important for heteroepitaxy is lattice mismatch between the substrate and over-layer. This mismatch corresponds to a difference in the lattice spacings or lattice structure of the two crystals at the interface, and can result in strained growth or defects in the over-layer structure. An example of structural mismatch is growth of a hexagonal crystal over-layer on a cubic substrate. For mismatch between crystals of the same symmetry, but different in-plane lattice

parameters a_{s} (substrate) and a_{o} (over-layer), the lattice mismatch f_{i} in direction i can be defined as follows [31].

$$f_{\mathrm{i}} = \frac{a_{\mathrm{si}} - a_{\mathrm{oi}}}{a_{\mathrm{oi}}}, \mathrm{i} = x, y \tag{1.11}$$

During MBE, a number of inequivalent rates are defined. The pressure measured by a beam flux gauge in the molecular beam is referred to as a beam equivalent pressure (BEP). Using Equation 1.9 an arrival rate can be calculated from this BEP. The incorporation rate of an elemental species is not necessarily proportional to the arrival rate of that species, but instead depends also upon the reaction kinetics at the surface and potentially the chemical abundance of another species. It is the incorporation rate which is then related to the growth rate of the material. For a situation in which the growth rate *is* simply related to the arrival rate of one species with BEP P, the growth rate may be expressed in the following equation.

$$GR = \frac{4}{\sqrt{2\pi}} \frac{PV_0}{\sqrt{k_{\mathrm{B}} T m}} \tag{1.12}$$

In this equation, V_0 is the volume per formula unit, m the mass of the molecule in the molecular beam and all other symbols have their usual meanings. The derivation for this equation is shown in Appendix A.

1.4.3 Reflection high energy electron diffraction

Reflection high energy electron diffraction (RHEED), is a valuable in situ technique routinely used in combination with MBE, and can be used to determine various physical properties of the surface during growth. RHEED is achieved by directing a high energy electron beam (10-20 keV) onto the sample surface at a grazing angle (approx. 1-3°), and detecting the diffracted beam on a phosphor screen beyond the surface. As a consequence of the grazing incidence of the electron beam, the electron gun and the phosphor screen are out of the path of the molecular beams in an MBE chamber. This means that in contrast to other electron diffraction techniques with different geometries such as low energy electron diffraction (LEED), RHEED can be carried out during growth. The geometry of RHEED can be seen in panel c of Figures 1.6 and 1.7. The diffraction pattern on the phosphor screen can be used to determine the physical state of the surface, including details of the in-plane lattice parameter and symmetry, surface

orientation and reconstruction periodicities.

For a near mono-energetic incident electron beam, wavevector $\underline{k}_{\mathrm{I}}$, the diffracted beam will have a range of energies, with a sharp elastic peak, a broad flat secondary electron tail and some well defined energy losses due to plasmon and phonon losses. These well defined losses will be small compared to the beam energy, and so are indistinguishable from the elastic peak. Diffraction features arise from the elastic peak, while the secondary tail contributes to the background intensity. Secondary electrons diffracted by bulk geometry give rise to Kikuchi features, distinct patterns in the background intensity which are highly characteristic of specific substrate orientations.

Diffracted elastic electrons must have a wavevector $\underline{k}_{\mathrm{F}}$ such that energy (Equation 1.15) and momentum (Equation 1.16) conservation are obeyed. Energy conservation can be expressed as follows.

$$E_{\mathrm{I}} = E_{\mathrm{F}} \tag{1.13}$$

$$E = \frac{\hbar^2 k^2}{2m} \tag{1.14}$$

Hence

$$|k_{\mathrm{I}}| = |k_{\mathrm{F}}| \tag{1.15}$$

Momentum conservation dictates that the electron may only change momentum by certain values which are dependent upon the reciprocal lattice of the scattering crystal. Allowed values of the momentum after scattering are therefore given by equation 1.16, in which $\underline{g}_{ijk}$ defines the reciprocal lattice of the crystal.

$$\underline{k}_{\mathrm{I}} = \underline{k}_{\mathrm{F}} + \underline{g}_{ijk} \tag{1.16}$$

The reciprocal lattice is defined as

$$\underline{g}_{ijk} = i\underline{a}_1^* + j\underline{a}_2^* + k\underline{a}_3^* \tag{1.17}$$

where *i*, *j* and *k* are integers, and $\underline{a}_{1,2,3}^*$ are the reciprocal lattice vectors. These are defined as

$$\underline{a}_1^* = 2\pi \frac{\underline{a}_2 \wedge \underline{a}_3}{a_1.(\underline{a}_2 \wedge \underline{a}_3)} \tag{1.18}$$

$$\underline{a}_2^* = 2\pi \frac{\underline{a}_3 \wedge \underline{a}_1}{\underline{a}_2.(\underline{a}_3 \wedge \underline{a}_1)} \tag{1.19}$$

$$\underline{a}_3^* = 2\pi \frac{\underline{a}_1 \wedge \underline{a}_2}{\underline{a}_3.(\underline{a}_1 \wedge \underline{a}_2)} \tag{1.20}$$

where $\underline{a}_{1,2,3}$ are real space lattice vectors for the crystal.

The solution to equations 1.15 and 1.16 can be obtained using the Ewald sphere construction. In this construction, the initial wavevector $\underline{k}_{\mathrm{I}}$ is drawn with its tail end on a point in reciprocal space. A sphere of radius $|k|$ is then drawn with its origin at the head end of the vector $\underline{k}_{\mathrm{I}}$. Diffraction is now allowed for all $\underline{k}_{\mathrm{F}}$ which begin at the origin of the sphere and end where the surface of the sphere and a reciprocal lattice point ($\underline{g}_{ijk}$) coincide. This construction ensures that the conditions in equations 1.15 and 1.16 are obeyed.

Transmission diffraction

Figure 1.6 shows a 2D cross section through an Ewald sphere construction for diffraction using RHEED geometry. The electron beam diffracts through a 3D island on the surface, which is sufficiently bulk-like to exhibit 3D periodicity, but small enough that it does not attenuate the beam. In this case, diffraction conditions are met when the Ewald sphere intersects a reciprocal lattice point. These beams then exit the material and are observed on the phosphor screen. The diffraction features correspond to the intersection of the Ewald sphere with reciprocal points, and as such appear as circular spots on the RHEED screen as illustrated in Figure 1.6b. These RHEED patterns are said to be 'spotty'. This type of diffraction is referred to as transmission diffraction, and is characteristic of a rough surface or the presence of small crystallites or 3D islands on the surface.

Surface diffraction

As a result of the disruption in periodicity represented by a surface, the conditions for diffraction are relaxed for diffraction from a surface. Since the periodicity perpendicular to the surface is broken, conservation of momentum is replaced by conservation of momentum parallel to the surface $\underline{k}^{||}$. This also results in a reduction of the reciprocal lattice to $\underline{g}_{ij}$

$$\underline{g}_{ij} = i\underline{a}_1^* + j\underline{a}_2^* \tag{1.21}$$

and conservation of momentum becomes

$$\underline{k}_{\mathrm{I}}^{||} = \underline{k}_{\mathrm{F}}^{||} + \underline{g}_{ij} \tag{1.22}$$

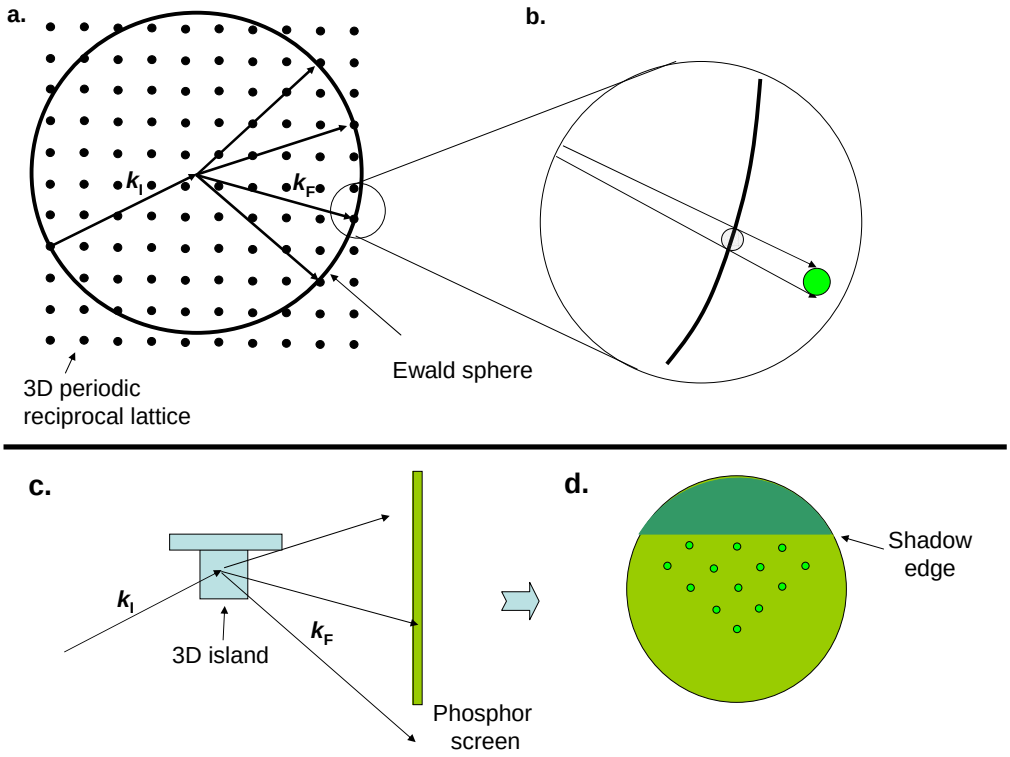

Figure 1.6: Transmission diffraction with the RHEED geometry. (a) Intersection of reciprocal lattice points with the Ewald sphere. (b) Illustration of the formation of spots due to lattice points. (c) Geometry of RHEED through a small 3D island on the surface. (d) Illustration of the RHEED screen for transmission diffraction.

This modifies the Ewald sphere construction such that rather than the intersection of the Ewald sphere with lattice points $\underline{g}_{ijk}$ defining allowed diffraction conditions, it is the intersection of infinitely long rods (perpendicular to $\underline{a}_1^*$ and $\underline{a}_2^*$, at positions $\underline{g}_{ij}$) with the Ewald sphere. The intersection of rows of reciprocal lattice rods with the Ewald sphere results in concentric rings of diffraction features on the RHEED screen. These are termed Laue zones. As a consequence of variations in electron energy, angular divergence from the electron source and surface disorder, the rods have a finite width. In the first Laue zone of a RHEED pattern, the rods are almost tangential to the Ewald sphere, and as a result diffraction 'streaks' are observed. Surface diffraction is illustrated in Figure 1.7. Figure 1.8 shows a typical RHEED pattern from a flat surface, illustrating the main features.

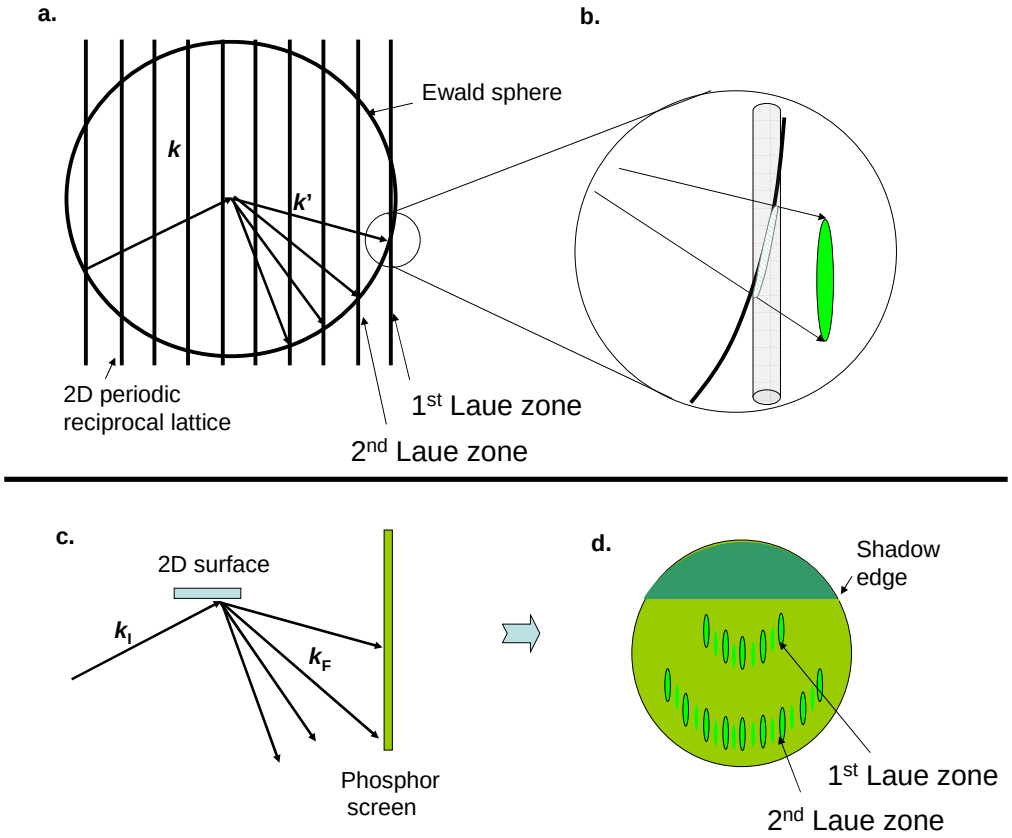

Figure 1.7: Surface diffraction with the RHEED geometry. (a) Intersection of reciprocal rods with the Ewald sphere. (b) Illustration of the formation of streaks due to the finite width of the rods. (c) Geometry of RHEED of a flat surface. (d) Illustration of the RHEED screen for surface diffraction.

Interpretation of RHEED patterns

A RHEED pattern then is the intersection of the reciprocal lattice with the Ewald sphere. The spacing of the RHEED streaks can give information regarding the periodicity of the surface, providing valuable information about the surface structure. As a result of the penetration of the electron beam into the bulk, RHEED streaks corresponding to the bulk terminated (1×1) surface mesh are typically brighter than those corresponding to the surface localised periodicity resulting from the surface reconstruction. These brighter features are termed the integer order streaks, and can be used as a reference for the surface reconstructions. A pattern showing only integer order streaks is referred to as a (1×1) reconstruction. Weaker fractional order streaks are located between the integer order streaks and indicate the periodicity of the surface reconstruction. This

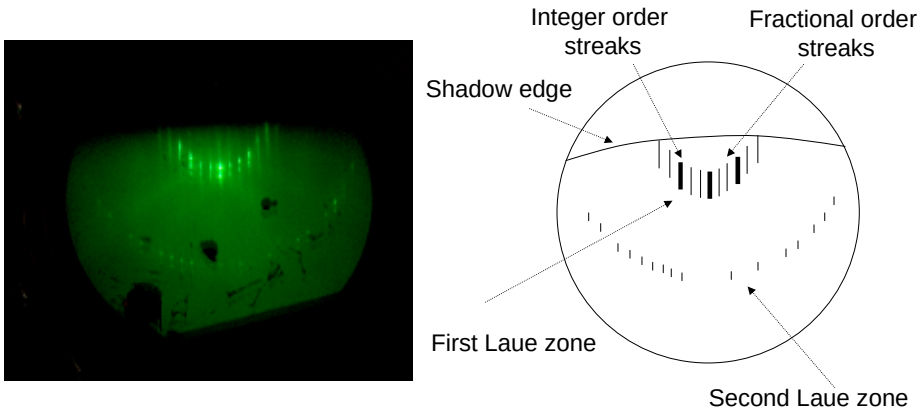

Figure 1.8: RHEED pattern obtained from an InSb(001) surface with the electron beam directed along the $(1\bar{1}0)$ direction, showing a 3$\times$ periodicity. The illustration on the right shows the main features of the pattern. Dark patches on the image are a result of damage to the phosphor screen.

smaller spacing in reciprocal space indicates the greater spacing in real space. For a pattern exhibiting n equally spaced streaks between the integer order streaks, a (n+1)$\times$ periodicity in real space is indicated. In the example shown in Figure 1.8, there are two fractional order streaks when viewed with the RHEED beam along the $(1\bar{1}0)$ direction. This indicates a 3$\times$ periodicity. As a result of the way in which RHEED patterns are formed, for a reconstruction on a surface defined by the real space vectors a_1 and a_2, the periodicity in the a_1 direction (i.e. n$\times$) is observed when the RHEED beam is aligned along the direction of a_2. This is important when labelling RHEED images, and the distinction between the periodicity direction and e-beam direction is crucial.

1.4.4 X-ray photoelectron spectroscopy

Whilst RHEED is able to provide valuable details concerning the flatness and structure of a surface, it gives no chemical information. In order to obtain details regarding the composition of the sample surface, spectroscopic techniques such as X-ray photoelectron spectroscopy (XPS) may be used. XPS uses X-rays to excite electrons from core states and eject them from the sample. The energy with which the electrons emerge are characteristic of the element and state from which they originate. Energy analysis of the photoelectrons allows for determination of the elemental composition of

a material. More detailed analysis allows for identification of different bonding configurations and some limited depth information to be obtained.

The electrons in an atom are localised into discrete energy levels, defined by the quantum numbers n (primary quantum number), l (orbital angular momentum quantum number), m (magnetic quantum number). Each energy level may be populated by up to two electrons of opposite spin $s = \pm\frac{1}{2}$. In addition, j (total angular momentum quantum number) is defined

$$j = l \pm \frac{1}{2} \tag{1.23}$$

Some electronic states with the relevant quantum numbers, in addition to electron populations are summarised in Table 1.1. In order to remove an electron from one of these core levels to the vacuum level, an energy in excess of the binding energy E_{BE} must be transferred to the electron. In XPS, X-rays of known energy $h\nu$ are used to excite electrons from the core levels into the vacuum, with any excess energy passed to the electron in the form of kinetic energy (E_{k}), which is expressed as

$$E_{\mathrm{k}} = h\nu - E_{\mathrm{BE}} \tag{1.24}$$

This is a rather oversimplified situation, since it takes no account of relaxation of other electrons in the atoms (intra-atomic relaxation, E_a), or the effect of the surrounding atoms (interatomic relaxation, E_r). As such a more complicated equation may be expressed.

$$E_{\mathrm{k}} = h\nu - E_{\mathrm{BE}} + E_a + E_r \tag{1.25}$$

State	Shell	State	n	l	j	No. of electrons
1s	K	K	1	0	1/2	2
2s	L	L1	2	0	1/2	2
$2p_{1/2}$		L2	2	1	1/2	2
$2p_{3/2}$		L3	2	1	3/2	4
3s	M	M1	3	0	1/2	2
$3p_{1/2}$		M2	3	1	1/2	2
$3p_{3/2}$		M3	3	1	3/2	4
$3d_{3/2}$		M4	3	2	3/2	4
$3d_{5/2}$		M5	3	2	5/2	6

Table 1.1: Data table showing the primary quantum number (n), orbital angular momentum quantum number (l), and total angular momentum quantum number (j) in addition to electron populations of a number of core states

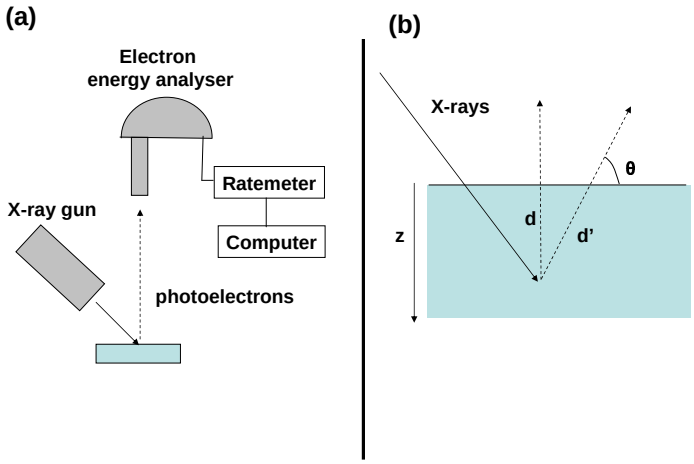

Figure 1.9: (a) Typical XPS setup with a take off angle (TOA) = 90°, (b) attenuation depth d', as a function of take off angle θ and sampling depth d

Changes in local environments of atoms may therefore lead to shifts in the kinetic energy of photoelectrons. This is termed a chemical shift.

The probability of a photoelectron originating from an atom at a depth d from the sample surface, emitted at an angle θ (illustrated in Figure 1.9b) reaching the surface without inelastic scattering is given by

$$I(d) = I(0)\exp\left(\frac{-d}{\lambda(E_{\mathrm{k}})\sin\theta}\right) \tag{1.26}$$

The inelastic mean free paths (IMFP) $\lambda(E_{\mathrm{k}})$ in solids are very short in the energy range typically observed in XPS (0-1486 eV), with $\lambda(1486eV)$ in GaAs only 22 Å. Because of the exponential decay of the probability distributions, photoelectrons are only detected to a depth of 3-4 $\lambda(E_{\mathrm{k}})$ and so the technique is highly surface sensitive.

Figure 1.9 shows the setup of a typical XPS experiment. The sample is irradiated with mono-energetic X-rays (typically Al Kα radiation, $h\nu$ = 1486.7 eV), and the electrons emitted at a take off angle (TOA) of θ from the plane are detected by an electron energy analyser. The analyser sweeps the pass energy of electrons detected, and obtains a spectrum, such as the one seen in Figure 1.10a. XPS spectra are typically plotted with binding energy ($h\nu - E_{\mathrm{k}}$) decreasing from left to right. Each peak in the spectrum corresponds to a state from Table 1.1 from one of the elements in the sample. Since the binding energy of each state is element specific, the positions of the peaks provide an elemental fingerprint, which allows the chemical compositions of samples to

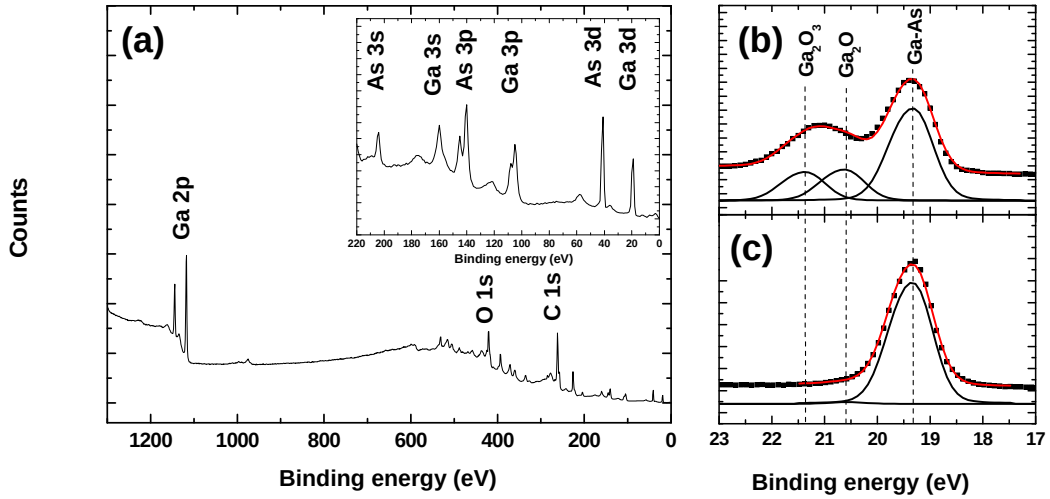

Figure 1.10: (a) Wide scan of an uncleaned GaAs wafer, and detailed scans of the Ga 3d peak for uncleaned (b) and cleaned (c) GaAs. Ga 3d spectra have been fitted with three peaks with FWHM = 0.76 eV and L:G = 16% [35].

be determined.

Interpretation of XPS spectra

Two types of XPS analysis are commonly used: elemental peak ratios, which allow for rough determination of the surface stoichiometry, and more detailed peak fitting which provides information regarding the chemical environments of different atoms.

In order to obtain elemental peak ratios, the area of one peak for each element is measured, normalized according to a number of factors, and then a ratio is obtained. A^p, the peak area is the integrated area under peak p, with an appropriate Shirley background subtracted from it [36]. In the present study, this was performed using the program XPSpeak 4.1 [37]. Once the peak areas have been obtained, they must be normalised according to the scan parameters dwell time (D_{scan}) and number of scans (n_{scan}), in addition to the atomic sensitivity factor (a_{asf}) which is obtained from the literature. The final parameter which determines the peak area is the probing depth, which in turn is dependent upon the IMFP $\lambda^p(E_{\mathrm{k}})$. Rigorously, the peak area depends upon a combination of IMFP and the concentration profile $c^p(z)$ of the element giving rise to the peak.

$$A^p \sim \int_0^\infty c^p(z)\exp\left(\frac{-z}{\lambda^p(E_{\mathrm{k}})\sin\theta}\right)dz \tag{1.27}$$

Clearly normalisation for this parameter requires exact knowledge of the structure of the surface region. It is possible to simulate possible structures and optimise the structure to fit the experimental data [35], although this method is time consuming and potentially overcomplicated. For the purpose of simple elemental peak ratios, it is sufficient to observe that the peak area calculated from Equation 1.27 for a uniform concentration profile ($c^p(z) = \text{constant}$) is proportional to $\lambda(E_\text{k})$. Under this simplification, the normalised peak area I^p may be expressed

$$I^p = \frac{A^p}{D_\text{scan} n_\text{scan} a_\text{asf} \lambda(E_\text{k})} \tag{1.28}$$

Following this normalisation for all peaks, ratios may be taken as usual. This method is very useful for a first approximation of the surface stoichiometry.

The second method of XPS analysis involves more detailed examination of the peak shapes. Atoms in different chemical environments experience different screening and relaxation effects, and as such present slightly different binding energies. An XPS peak may therefore be viewed as a number of superimposed peaks. An example is shown in Figure 1.10b. A number of shifted peaks formed from linear combinations of Lorentzian and Gaussian line shapes (pseudo-Voigt functions) of variable full width half maximum (FWHM) and mixing ratio (L:G) are fitted. These peak shapes simulate experimental and instrument broadening of the energy levels. Peak fitting involves attempting to fit the experimentally obtained spectra with a number of these peaks, under suitable constraints. Typically FWHM and L:G are constant for all peaks, and the binding energy shifts between peaks are informed by the literature. The suitability of a simulated fit may be judged either manually by ensuring the main features of the spectrum are present or by minimisation of a calculated χ^2 figure of merit provided by fitting programs. In practice a mixture of the two is typically used. In the majority of cases, at least two peaks are observed for a contaminated sample: the bulk bonding environment, and a higher binding energy oxide peak. Other peaks may appear as a result of different oxides, or surface related peaks. Figure 1.10 shows the Ga 3d spectra for uncleaned (b) and cleaned (c) GaAs. The uncleaned sample shows two oxide peaks which are no longer present after cleaning. In this manner the contamination of the surface may be determined, in addition to the presence or absence of other unusual bonding configurations.

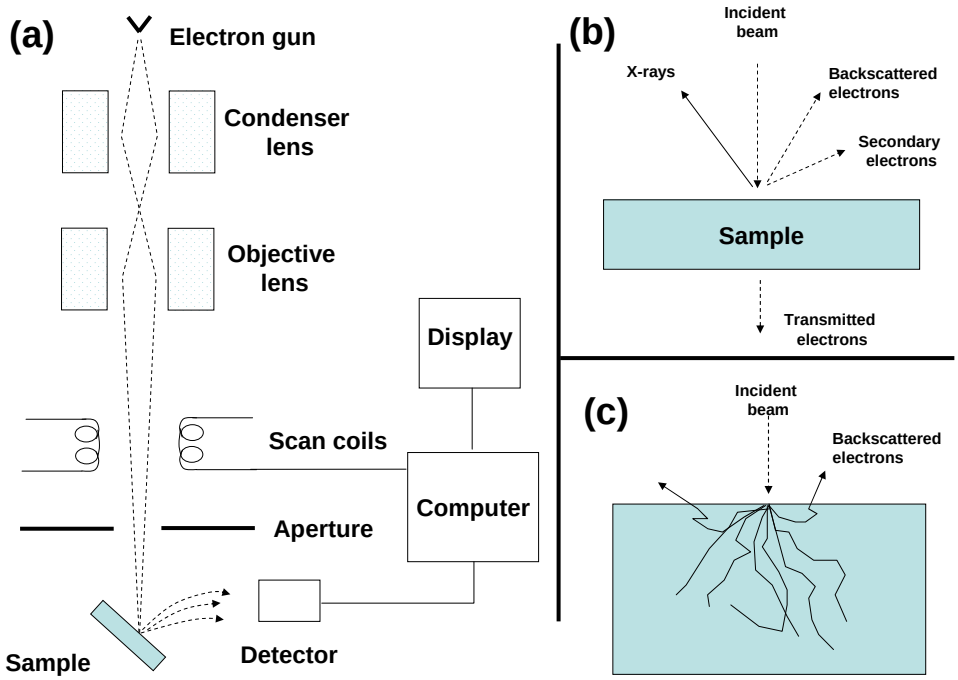

Figure 1.11: (a) Schematic of an SEM instrument, (b) Emission mechanisms used for SEM imaging, (c) Illustration of the random walk followed by primary electrons.

1.4.5 Scanning electron microscopy

A major strength of MBE is the ability to grow layers which have large terraces (>100 nm) separated by mono-layer steps. This morphological perfection is essential in quantum wells and other structures, although it is not unusual for other morphology to develop over long growth runs under imperfect growth conditions or in strained layers. As a result, surface features may vary in size from a few Å, to a few μm. Optical microscopes are limited in lateral resolution by the wavelength of light and so radiation with a shorter wavelength is required for improved resolution. To this end, electrons are used as the basis for a number of electron microscopies such as transmission electron microscopy (TEM) and scanning electron microscopy (SEM), which may resolve features down to the nm scale.

Electrons accelerated to tens of keV may be treated as electromagnetic waves of small wavelength, $\lambda \sim$ 0.001-0.01nm, which allows smaller objects to be resolved than is possible with optical microscopy. In SEM an electron beam is generated using either a thermionic electron gun (a heated metallic filament) or a field emission gun where

a high field is used to allow electrons to tunnel from the metal. These electrons are then extracted, accelerated and focussed using a series of electrodes. The beam from the electron gun is then manipulated by magnetic coils using the interaction of moving charge with magnetic fields. The coils act as a series of lenses, focussing the beam, which is then steered across the sample by the scan coils. The electron beam is rastered across the sample in order to build up an image. A schematic for an SEM instrument is shown in Figure 1.11a. The contrast mechanism at a point on an SEM image is determined by the detection rate of various types of emission when the electron beam is directed at the corresponding point on the sample. This forms an image which reflects not only the physical geometry and structure of the surface, but also some degree of elemental contrast. The various emission processes are discussed briefly below. As a result of the high attenuation of electron beams by gases, SEM is carried out in vacuum, at pressures better than $\sim 10^{-4}$ mbar.

When the electron beam hits a sample, the electrons may scatter either elastically (no loss of energy) or inelastically (energy lost to the material) with the sample material. Throughout these scattering events, the electrons carry out a random walk though the material, as illustrated in Figure 1.11c. This random walk defines the interaction volume, within which the beam has some interaction with the sample and is dependent upon the electron energy and density of the material. The width of the interaction volume calculated for 10 keV electrons in MnSb is 0.6 μm. As a result of this interaction, a number of emission processes occur. Secondary electrons are low energy electrons ($<$50 eV) which emerge from the sample. These may either be primary electrons which have lost almost all their energy by inelastic collisions and have random walked to the surface, or more likely, electrons from the sample which have gained a small quantity of energy from a primary electron. This is the most common detection mode used in SEM, since emission of secondary electrons is typically confined to the diameter of the electron beam, and as such provides the best spatial resolution. Resolution of the order of several nm may be obtained depending upon sample conductivity and spot size. Backscattered electrons are primary electrons which follow a random walk through the sample and back out of the surface. Because these are primary electrons, they have rather higher energies than the secondary electrons. Transmission electrons are primary electrons which are not halted when passing through a (thin) sample, and are the signal used for TEM.

As a result of electron excitation and relaxation caused by primary electrons passing through the sample, X-rays characteristic of the sample material are also emitted during SEM. This is the basis for energy dispersive analysis of X-rays (EDX). In EDX, the electron beam is directed at a point on the sample, and the X-ray energy spectrum is measured. This spectrum has characteristic peaks indicating the elements present in a similar fashion to XPS. The elemental composition of the material at that point can therefore be determined. Because of the low attenuation of X-rays, the detection volume of EDX is comparable to the interaction volume, and hence the resolution is considerably worse than that of secondary electron images. The EDX spectrum is also considerably less surface specific than XPS, which is problematic for study of thin films. By selection of the appropriate detection and hence contrast mode, features down to nm scales can be observed by SEM, as well as some elemental characterisation of different points of the sample.

1.4.6 Scanning tunnelling microscopy

Scanning tunnelling microscopy (STM), first implemented by Binnig and Rohrer in 1982, is now an essential technique for the surface science community, allowing the imaging of surfaces on the atomic scale, and in conjunction with other techniques allows for the determination of surface reconstructions. STM is based on the quantum tunnelling of electrons through gaps between conducting electrodes which is allowed at high electric fields ($\simeq 10^6$ Vcm^{-1}), or at very small separations ($<$ 1nm). In STM, an atomically sharp tip is brought close to a sample, and a voltage applied between the two (Figure 1.12). The electron wavefunction $\psi(x)$ with energy E observes a potential barrier of height V_{B} in the classically forbidden region between the tip and sample. From quantum mechanics, the behaviour of the electron may be expressed by the following time independent Schrödinger equation

$$\frac{-\hbar^2}{2m}\frac{d^2\psi(x)}{dx^2} + V(x)\psi(x) = E\psi(x) \tag{1.29}$$

Solving this at a distance d into the barrier where $x = d$ and $E < V$, gives the solution of the form:

$$\psi(x) = \exp(-\kappa d) \tag{1.30}$$

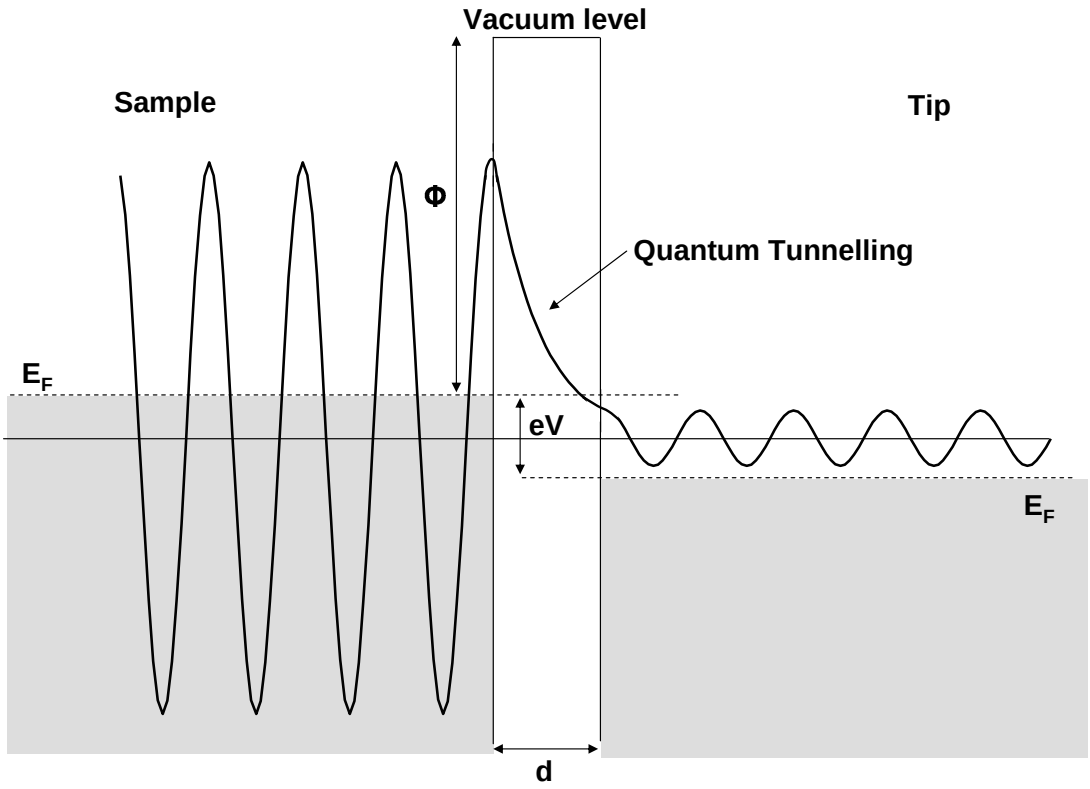

Figure 1.12: Illustration of the electron wavefunction in the tunneling region between a sample and STM tip. Reproduced from [38].

$$\kappa = \frac{\sqrt{2m(V_{\mathrm{B}} - E)}}{\hbar} \tag{1.31}$$

Substituting in the work function $\phi = (V_{\mathrm{B}} - E)$.

$$\kappa = \frac{\sqrt{2m\phi}}{\hbar} \tag{1.32}$$

Thus the wavefunction, and hence the current tunnelling through the barrier has an exponential dependence on the barrier width d. It is this high sensitivity of the tunnelling current on the tip-sample separation which is exploited in STM. Figure 1.12 illustrates the wavefunction for an electron passing through a tunnelling barrier.

Figure 1.13 shows the setup for the STM system used in this work (an Omicron STM-1). The position of the tip is controlled by piezoelectric crystals (piezos) whose extension can be controlled to an accuracy of $\sim$10 pm by application of an electric field. The x and y piezos operate in the plane of the sample, rastering the tip across the sample, while the z piezo controls the sample-tip distance d. When the biased sample and tip are sufficiently close, a tunnelling current is measured at the tip. The small (typically 100 pA -10 nA) tunnelling current is measured, amplified and converted into a voltage and then directed into a feedback loop, which drives the z piezo. This feedback loop moves the tip to a separation where the tunnelling current is equal to

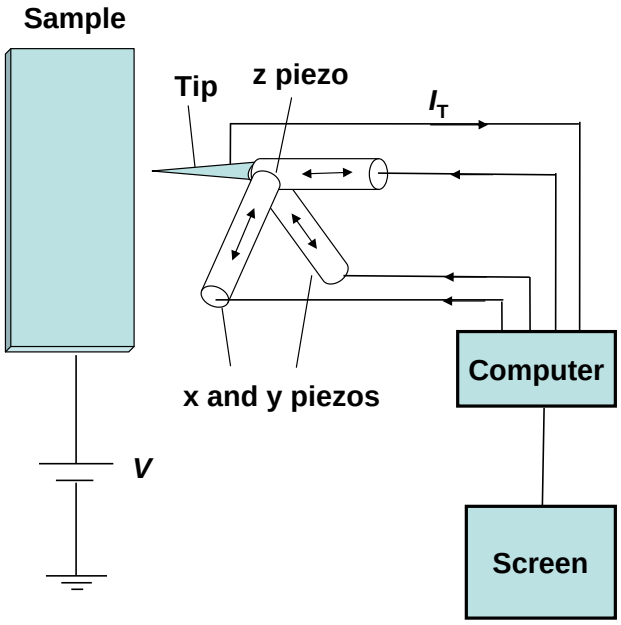

Figure 1.13: Schematic for the Omicron STM-1 instrument.

the setpoint (set by the user), and strives to maintain this separation. The tip is then rastered across the sample by applying a sawtooth profile voltage to the x and y piezos, and the extension of the z piezo is plotted as a function of the x and y positions. Since the tunnelling current is stabilised, any changes in the surface structure such as atomic steps or even changes in electron density due to dangling bonds are mapped by the scanning tip.

1.5 Crystallography and surface structures of III-V semiconductors

1.5.1 III-V semiconductor structure

As indicated by their name, III-V semiconductors consist of group III (Al, Ga, In) atoms bonded to group V (N, P, As, Sb). The band structure is such that there is an energy gap between the valence band maximum and conduction band minimum, allowing for versatile electronic properties, controllable through doping. III-V semicon-

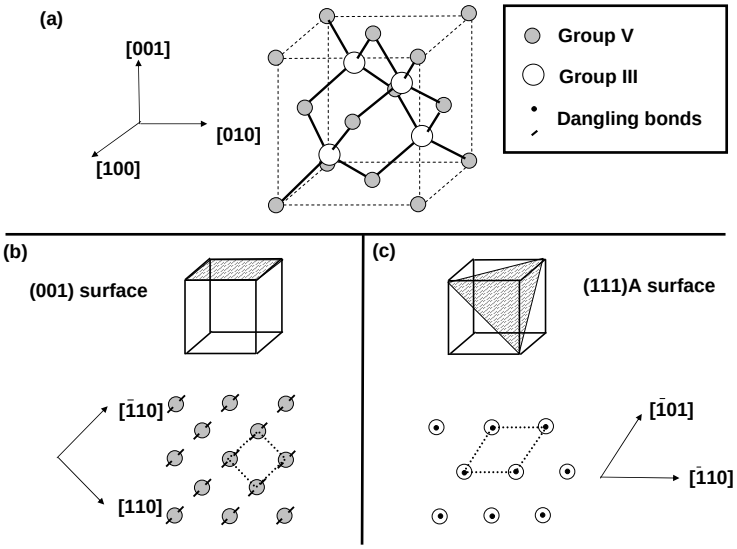

Figure 1.14: III-V zincblende crystal lattice (a) unit cell (b) (001) surface (c) (111)A surface.

ductors have the zincblende crystal structure, formed from a face centered cubic (fcc) arrangement with a two atom basis (a group V atom at (0,0,0) and a group III atom at $(\frac{1}{4}, \frac{1}{4}, \frac{1}{4})$). The unit cell for this structure is illustrated in Figure 1.14a. Each group III (V) atom is in a tetrahedral bonding configuration, with 4 sp^3 hybridised bonds to group V (III) atoms. On an (001) surface, the 'top' facing bonds (those directed from the atom towards the surface) of each group III atom are aligned along the [110] direction, while the 'bottom' facing bonds are along the $[1\bar{1}0]$. The opposite is true for the group V atoms. This convention is used for unambiguous labelling of the surface vectors, and hence surface reconstructions.

A surface represents a planar defect in the crystallographic lattice, resulting in uncompleted or 'dangling' bonds at the surface. Two low index surfaces are illustrated in Figure 1.14b and c. The (001) surfaces are formed from either group III or V atoms in a square surface lattice oriented along the [110] and $[1\bar{1}0]$ directions. Both the group III and V terminated layers have two dangling bonds per surface atom, and as such are expected to be approximately equivalent in terms of stability. (001) surfaces therefore may be either group III or V terminated, dependent upon the conditions, although as a result of the lower sublimation temperatures of group V elements, the surface after annealing in the absence of group V flux tends to be group III terminated.

The second low index plane shown is the (111)A. Similarly to (001) surfaces, the (111) surfaces have planes with a single elemental species. However, depending upon the orientation of the surface, the bonding configurations change. For (111) surfaces, group III atoms have only one top facing bond, while the group V have three. As a result (111) or (111)A surfaces are normally group III terminated due to minimisation of dangling bonds. The $(\bar{1}\bar{1}\bar{1})$ or (111)B surface is group V terminated since on this surface it is the group V atoms which have only one top facing bond. The (111)A and (111)B surfaces are therefore geometrically different surfaces, and cannot be derived from one another in the same way as different terminations of an (001) surface.

1.5.2 III-V surface reconstructions

For both surfaces shown in Figure 1.14, the (1×1) primitive unit cell for an unreconstructed surface is represented by a dotted line. It is energetically unfavorable for the crystal to retain this structure due to the dangling bonds. As a result, reconstructions characteristic of the material and surface occur to minimise the energy of the surface. Reconstructions appear as repeating tessellating structures, resulting in a larger unit cell on the surface.

By convention on (001) surfaces, a reconstruction (n×m) denotes a periodicity of n× along the $(1\bar{1}0)$ crystal direction and m× along the (110) crystal direction, as detailed in Section 1.3.2. For the (111) surfaces, the primitive lattice vectors are $(\bar{1}10)$ and $(01\bar{1})$. As a result of the high degree of rotational symmetry on the (111) surfaces, the reconstructions on these surfaces typically have the form (n×n) and little distinction regarding the allocation of the two primitive vectors in the reconstruction notation is made. Triple domain structures (td(n×m)) are also observed as a result of true three fold symmetry of (111) surfaces, although again the allocation of the n and m directions are unimportant.

A number of reconstructions of (001) and (111)B surfaces are shown in Figure 1.15 which demonstrate a range of reconstruction mechanisms. (2×4) reconstructions are observed on a number of materials, and various models have been proposed. On GaAs(001), the β2(2x4) model shown demonstrates dimer bonding [39]. The top facing bonds of the terminating element (As) form dimer bonds along the $<1\bar{1}0>$, which is the cause of the (2×m) periodicity. For a similar structure terminated with Ga dimers,

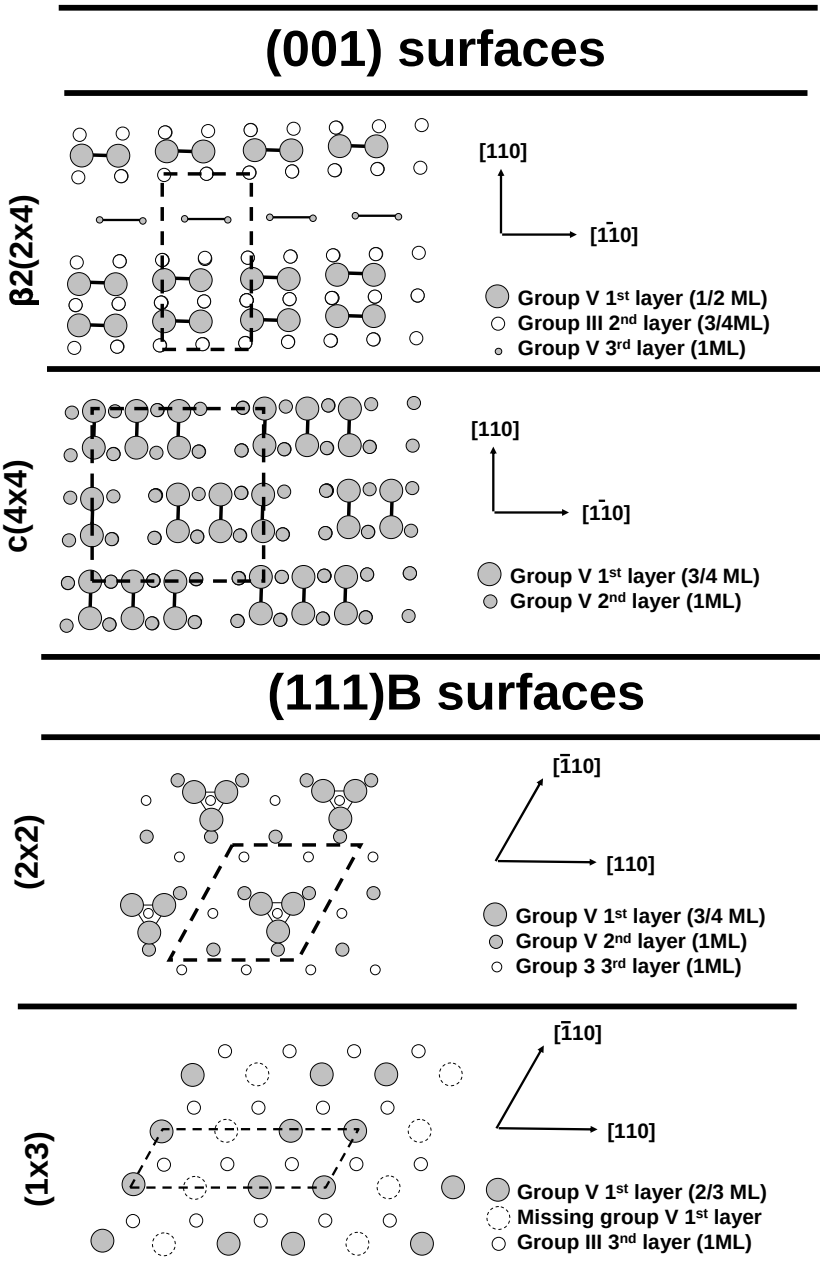

Figure 1.15: Surface reconstructions on the (001) and (111)B surface. Reconstruction unit cells are shown by dashed lines. Atom sizes indicate the proximity to the surface. Reproduced from [39, 40, 41, 42].

a (n×2) form is expected due to the different direction of the top facing Ga bonds. The 4× in the β2(2×4) appears as a result of two missing As dimer bonds and two missing 2nd layer Ga atoms, resulting in an exposed 3rd layer As dimer. The c(4×4), characteristic of InSb(001) has group V dimers above another layer of group V [40]. As a result of this double V layer, the group V dimer direction is not aligned along the expected $<1\bar{1}0>$ direction, but instead along the $<110>$. In c(4×4), groups of three group V dimers and a missing dimer tessellate in a staggered arrangement to form a brick pattern, forming the larger c(4×4) reconstruction.

On the (111)B surfaces, the (2×2) is a common reconstruction of many III-Vs (GaAs, InSb, InAs), and the structure proposed is a group V trimer on a full group V layer (as shown in Figure 1.15). Another (2×2) reconstruction, found on (111)A surfaces, is attributed to one missing group III atom per (2×2) unit cell in a group III terminated surface. The (1×3) shown in Figure 1.15 occurs on the (111)B surface, and has one, or possibly two missing rows of group V in every 3× spacing. This structure typically exhibits the triple domain structure. Other more complex reconstructions exist, such as the $(2\sqrt{3}\times2\sqrt{3})$R30° reconstruction (not shown here) observed on the InSb(111)A which incorporates 4 non-bulk like layers, and demonstrates inter-layer dimerisation and missing atoms [43].

1.5.3 Electron counting

On III-Vs, examination of surface reconstructions may be achieved by a combination of techniques, including STM, RHEED, XRD [44] and high resolution TEM [45]. Since none of these techniques provide direct, unambiguous models for the reconstructions, a method is required to check the suitability of a proposed surface reconstruction. One method used widely for III-V semiconductors is electron counting [46]. The predominant reason for surface reconstruction is to minimise the surface energy due to the dangling bonds. To first approximation, this means minimising the number of dangling bonds. In order to further reduce the energy, charge in the reconstruction may redistribute such that any group V dangling bonds are filled since the energy of these bonds are below the valence band maximum (VBM). Group III dangling bonds are emptied since the energy is above the VBM. The electron counting rule ensures that the number of electrons available exactly fulfills this criterion. Each III-V bond in the material con-

Reconstruction	III-III dimer	V-V dimer	III dangling	V dangling	Total electron counting
Excess(+)/ deficit(-)	-$\frac{2}{4}$e$^-$	+$\frac{2}{4}$e$^-$	+$\frac{3}{4}$e$^-$	-$\frac{3}{4}$e$^-$	
β2(2×4)	0	×3	×4	×6	0
c(4×4)	0	×30	0	×20	0
(2×2) trimer	0	×6	0	×4	0
(1×3) one missing row	0	0	×3	×2	+$\frac{3}{4}$e$^-$

Table 1.2: Electron counting for III-V surface reconstructions illustrated in Figure 1.15.

tains a total of 2 electrons (2e$^-$), with $\frac{3}{4}$e$^-$ from the group III and $\frac{5}{4}$e$^-$ from the group V on average. One tactic for electron counting is to count the number of non-bulk like bonding configurations, and calculate the excess (+) or deficit (-) of electrons due to each one. For example, a group V dangling bond has $\frac{5}{4}$e$^-$ from the V atom, but requires a total of 2e$^-$ in order to be filled (the energetically favorable state). Thus the deficit of a V dangling bond is -$\frac{3}{4}$e$^-$. A V-V dimer bond has a total of 2×$\frac{5}{4}$e$^-$ available, but only needs 2e$^-$. Thus the excess is +$\frac{2}{4}$e$^-$. If electron counting for a reconstruction is obeyed, the sum of the excess/defit from all non-bulk like bonds should be zero. Table 1.2 shows the excess/deficit of the different bonds, and the electron counting for the reconstructions shown in Figure 1.15. All these structures except the (1×3) obey the electron counting rule, giving confidence in their structures. The (1×3) reconstruction reduces the electron counting excess/deficit from $-\frac{9}{4}$ for an unreconstructed surface to +$\frac{3}{4}$ per (1×3) area. This model therefore seems more stable than the unreconstructed surface, even though it does not obey electron counting.

Certain elemental substitutions are allowed on III-V surfaces without altering the electron counting results. For any group III atom with one dangling bond, it is permitted to replace it with a group V . This is because the increase in valency from 3e$^-$ to 5e$^-$ is compensated by the presence of a group V dangling bond which must be filled, requiring 2e$^-$. The opposite is also true, allowing substitution of a group V with a group III under the same conditions. This is the basis for variations on structures illustrated in Figure 1.15, such as a version of the c(4×4) model in which rather than group V dimers, III-V hetero-dimers are present instead [47].

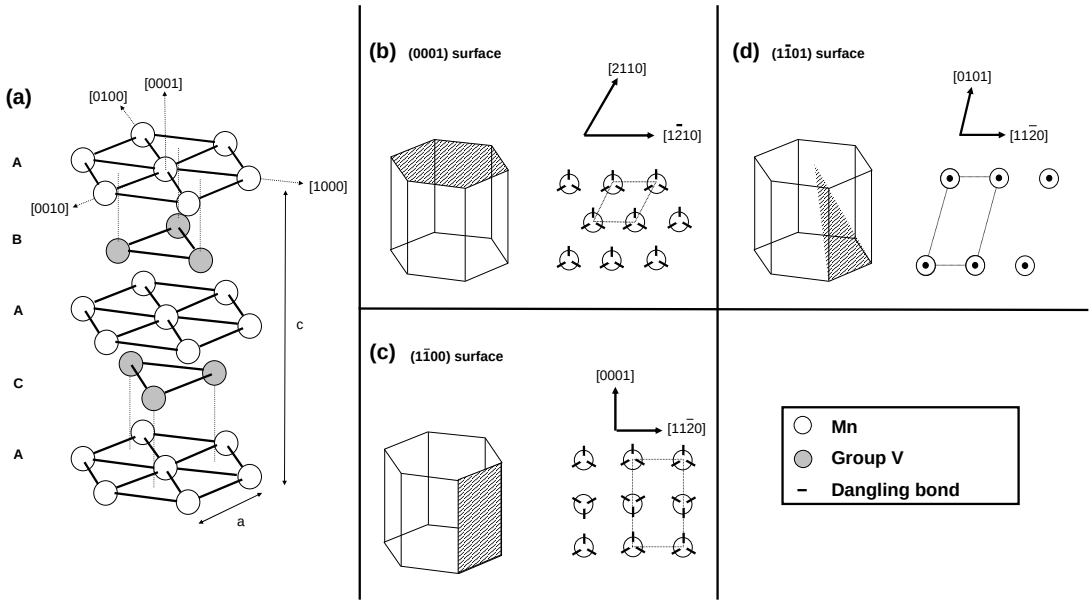

Figure 1.16: Exploded view of the MnX crystal with the NiAs structure, and schematics for three low index surfaces: (b) (0001), (c) (1$\bar{1}$00), (d) (1$\bar{1}$01).

1.6 Crystallography and surface structures of Manganese pnictides

1.6.1 Manganese pnictide structure

Manganese pnictides are a group of binary metallic ferromagnets containing Mn and a group V element. Mn pnictides have the chemical formula MnX (X = P, As, Sb etc.) and adopt a variety of structures. The most common is the NiAs structure which has alternating hexagonal close packed layers of Mn and X, stacked in the [0001] direction with spacing of $c/4$. The structure has a stacking order ABACA, in which A(Mn),B(X) and C(X) are the three different close packing positions for the hexagonal layers. Thus the Mn and X atoms are in octahedral and triangular prism bonding environments respectively, each forming six bonds to the other element. The lattice parameters are defined as a; the separation of nearest neighbours in the close packing plane and c, the separation between consecutive B (or C) layers. Hence c corresponds to a bi-layer of MnX. Figure 1.16 illustrates an exploded view of the structure, and three low index surfaces of the structure. A second structure demonstrated by certain MnX

Material	X	a(Å)	c(Å)	c/a	$T_{\mathrm{c}}(K)$	μ(0K)[50]	Structures
MnP	P	a = 5.916 b = 3.173	5.260	-	291	-	Orthorhomic [51]
MnAs	As	a = 5.72 b = 3.69 3.702	6.375 5.79	 1.56	 318	 3.4μ_{B}	MnP [52] at (318K<T<398K) NiAs elsewhere
MnSb	Sb	4.128	5.789	1.40	587	3.5μ_{B}	NiAs
MnBi	Bi	4.26	6.05	1.42	670	4μ_{B}	NiAs [53]

Table 1.3: Lattice parameters (a,c), curie temperatures (T_{C}), magnetic moment (μ) and structures for a number of Mn pnictides.

materials is an orthorhombic structure commonly referred to as the MnP structure. This orthorhombic structure can be related to a distorted NiAs lattice, in which one of the $[2\bar{1}\bar{1}0]$ directions is stretched such that there are two inequivalent lattice parameters in the (0001) plane labelled a and b [48]. This structure is adopted by MnP under most conditions and MnAs in the temperature range 318 K$<T<$398 K [49]. Table 1.3 shows the properties of a number of Mn pnictides.

Some studies have indicated that strained MnSb and MnBi with zincblende or tetragonal structures may be half metallic [54], which would provide the possibility of high spin polarisation in addition to high epitaxial compatibility with zincblende semiconductors. These strained materials clearly present further opportunities for spin injection.

1.6.2 Literature search of Mn pnictide growth and structure

A selection of growth papers for MnSb and MnAs are summarised in Table 1.4. The most extensively studied system is MnAs/GaAs(001). Both Ploog *et al.* and Tanaka *et al.* have studied a variety of aspects of the growth and characterisation of the MnAs layers including bulk properties such as the lattice structure by XRD [49, 55] and magnetic measurements using SQUID [56, 57], in addition to surface structure studies by atomic force microscopy (AFM) [55], magnetic force microscopy [58] and STM [59]. The growth of MnAs on GaAs(001) has been observed to grow in two different orientations, $(1\bar{1}00)$ and $(1\bar{1}01)$, dependent upon the growth conditions [57]. Both growth planes are indicated in Figure 1.16. A number of surface reconstructions on

the $(1\bar{1}00)$ growth plane have been observed by RHEED and STM [59]. These are (4×1), (2×1), (1×1) and (1×2) reconstructions in order of decreasing substrate temperature. The low temperature surfaces are believed to be As rich, and a 0.25ML As adatom model has been proposed for the (1×2) [59]. Growth of MnSb on GaAs(001) has also been covered in some detail, although only a single growth orientation $(1\bar{1}01)$ is obtained over a large range of substrate temperatures [60]. No surface reconstructions have been reported on this surface beyond the (1×1) characteristic of a highly disordered surface. Typically these surfaces appear rough from SEM [61] and AFM [62] measurements.

On the GaAs(111) growth surface, considerably flatter surfaces have been obtained due to the more favorable structural match between III-V(111) and MnX(0001) planes. The growth orientation is indeed found to be (0001)‖(111) in all cases, exhibiting (2×2) reconstructions on both MnAs [63] and MnSb [64]. In addition to this, Ouerghi *et al.* have observed a low temperature, As rich (1×3) triple domain reconstruction ($td(1\times3)$). Both this and the (2×2) have been observed directly with STM. The (2×2) shows triangular atomic scale structures which appear consistent with As trimers [63], while the $td(1\times3)$ appears as As rich 'sticks' lying on the surface in three equivalent surface directions [65]. The similarity between the As trimers of the MnAs(2×2) and those of the (2×2) reconstruction on III-V(111) was noted. To date, other than the (2×2) and a (1×1) which may be attributed to a highly disordered surface [66], no further reconstructions have been observed on MnSb(0001) surfaces. While the growth studies in the literature are predominantly on GaAs substrates, a number of other substrates have been studied, including Si [67], GaSb [32] and InP. Tanaka *et al* have successfully grown epitaxial MnAs on InP(001), which adopts the same $(\bar{1}100)$ growth orientation observed on the GaAs(001) substrate [68].

A variety of techniques have been used for epitaxial growth of MnAs and MnSb, including pulsed laser deposition (PLD), hot wall epitaxy (HWE) and most commonly molecular beam epitaxy (MBE). The growth parameters employed by different groups vary considerably, with temperatures from 50 °C to 500 °C, and X:Mn flux ratios between 2:1 up to 50:1 [69]. This large variation in growth parameters is problematic for determining the best conditions with which to begin this growth study. It is useful to note that in all cases, MnX growth is achieved with pnictide over-pressure, drawing obvious parallels with growth of III-Vs. By comparison then, the growth rate of MnX may

be expected to be Mn limited as a result of the pnictide overpressure, just as III-Vs are group III limited. Temperature appears to have considerable importance on the growth, in particular on (001) surfaces, and so will need to be studied. Various aids to the growth have been studied in the literature, including Mn pre-layers [70] and Hydrogen assisted growth [69], although these are rather more advanced techniques and require near optimal growth conditions before they can be assessed in any meaningful fashion.

MnX	Group	Substrate	Method	Substrate temperature (°C)	X:Mn flux ratio	GR (nm hr^{-1})	MnX growth plane	Surface	ref
MnSb	Tatsuoka *et al.*	GaAs(001)	HWE	350+	Sb rich		(0001)‖(111)	Rough(SEM)	[61, 71]
MnSb	Low *et al.*	GaAs(100)	MBE	410-490	Sb rich	90	(10.1)	Rough(AFM)	[62]
MnSb	Miyanishi *et al.*	GaAs(001)	MBE	50-400	4:1	144	$(1\bar{1}01)$	Rough(AFM)	[60]
MnSb	Ono *et al.*	GaAs(001) GaAs(111)B	MBE	300	2:1	108	$(1\bar{1}01)$ (0001)	(1×1) (2×2)	[64] [64]
MnSb	Liu *et al.*	GaAs(111)B	PLD	150-325	Sb rich		(0001)	(2×2)	[70]
MnSb	Tatsuoka *et al.*	GaAs(111)A	HWE	350+	Sb rich		(0001)	Smooth(SEM)	[61]
MnAs	Ploog *et al.*	GaAs(001)	MBE	250	80-480:1	10	$(1\bar{1}00)$	(4×1) (2×1) (1×1) (1×2)	[72, 55, 73]
MnAs	Tanaka *et al*	GaAs(001)	MBE	200-250	2-5:1		$(\bar{1}100)$ $(\bar{1}101)$		[49, 57]
MnAs	Morishita *et al*	GaAs(001)	MBE+AH	250	50:1		$(\bar{1}100)$		[69]
MnAs	Ploog *et al.*	GaAs(111)B	MBE	250	11-170:1	10	(0001)	(2×2)	[63, 73]
MnAs	Ouerghi *et al.*	GaAs(111)B	MBE	280		150	(0001)	(2×2) (3×1)	[65, 74]
MnAs	Tanaka *et al*	InP(001)	MBE	250			$(\bar{1}100)$		[68]

Table 1.4: Summary of the literature of growth parameters and orientations for MnSb and MnAs grown on III-V substrates. Growth rates have been converted into nm hr^{-1} for convenience.

Chapter 2

System design, commissioning and calibration

The MBE-STM system used for this thesis was partially assembled between 2002-2003 by Dr G. Bell, based around a recycled MBE chamber designed and built in 1982. The chamber has undergone many modifications in the following years and from 2003 onwards, was tested and calibrated by the author. What follows is a brief introduction to the system, followed by the major calibrations used to asses the capabilities and limitations of the system and the results obtained in this thesis.

2.1 System overview

The MBE-STM system consists of two separate vacuum chambers which are divided by a gate valve, and are individually pumped. The principal chamber is the MBE chamber, in which growth is carried out, in addition to analysis of surface reconstructions and lattice parameters by RHEED. Currently the chamber has three shuttered effusion cells: Mn, Sb and In. Cells are separated by a water cooling shroud, and in addition the lower external wall of the chamber is cooled with chilled water. A 15 keV electron gun (VG Ltd., UK) operated at 12.5 keV and a phosphor screen at a distance of 280 $\pm$ 10 mm from the sample position are used for diffraction. The phosphor screen has a shutter to prevent deposition on the screen which would reduce the quality of the RHEED images. Samples are held in the MBE chamber on a manipulator with radiative sample heating, temperature measurement (by two thermocouples) and x, y, z and azimuthal motion. Sample temperature is controlled by a feedback loop from one of the thermocouples to a d.c. power supply unit. The MBE chamber is pumped by an ion pump (diode type, 500 ls^{-1} pumping speed at $\sim 10^{-6}$ mbar) and a titanium sublimation pump (TSP)

with liquid nitrogen cooled cryo-panels. A schematic of the MBE chamber is shown in Figure 2.1a. The chamber has two internal cooling shrouds, one surrounding the cells (the cooling tank), the other above the first designed to operate as a cryo-panel. Both are attached to the MBE base flange, and are shown in Figure 2.4. At present both are cooled with flowing chilled water.

The second chamber contains the STM and sample/tip preparation facilities. This chamber is illustrated in Figure 2.1b. Pumping for the second chamber is achieved by a turbomolecular pump (300 ls^{-1} pumping speed) and an ion pump (triode type, 70 ls^{-1} pumping speed at $\sim 10^{-6}$ mbar). The microscope is an STM-1 (Omicron GmbH, Germany), with electronics and computer interface designed and built by Nanograph Systems Limited (Nottingham, UK). Sample preparation is achieved by grazing incidence ion bombarding using an AS10 ion gun (VSW Ltd., UK) operating at 20 mA emission current. Sample current is measured to be 3.4 μAcm^{-2}, and estimated sputter yield is $\sim$ 0.04 mono-layers s^{-1}. In addition to STM, the STM chamber also has an X-ray gun and electron energy analyser for XPS. Despite considerable effort, the XPS has not been operational since being attached to the system. The STM chamber also has a load lock for fast-entry of samples and a carousel for sample storage.

Both chambers are baked up to $\simeq 150^{\circ}C$ using wrapped heater tapes and each has a residual gas analyser (Vacuum Analyst, VSW Ltd., UK). Base pressure in the MBE chamber is 3×10^{-10} mbar. Samples are transferred using linear/rotary magnetically coupled arms (UHV Design Ltd. UK).

2.2 Experimental Details

2.2.1 Sample mounting and cleaning

Samples grown and studied in the MBE-STM chamber were all mounted on stainless steel sample plates. These sample plates consist of a lug for sample transfer, and a raised sample position in order to avoid shadowing of the RHEED electron beams by parts of the manipulator. A sample plate is shown in Figure 2.2a. Sample wafers are fixed to the sample plate by wetting both bonding surfaces with eutectic solution (61% Ga, 27% In, 12% Sn) and joining them with molten indium. Despite the low melting point of In ($157^{\circ}C$), samples remain attached to the sample plate even at high

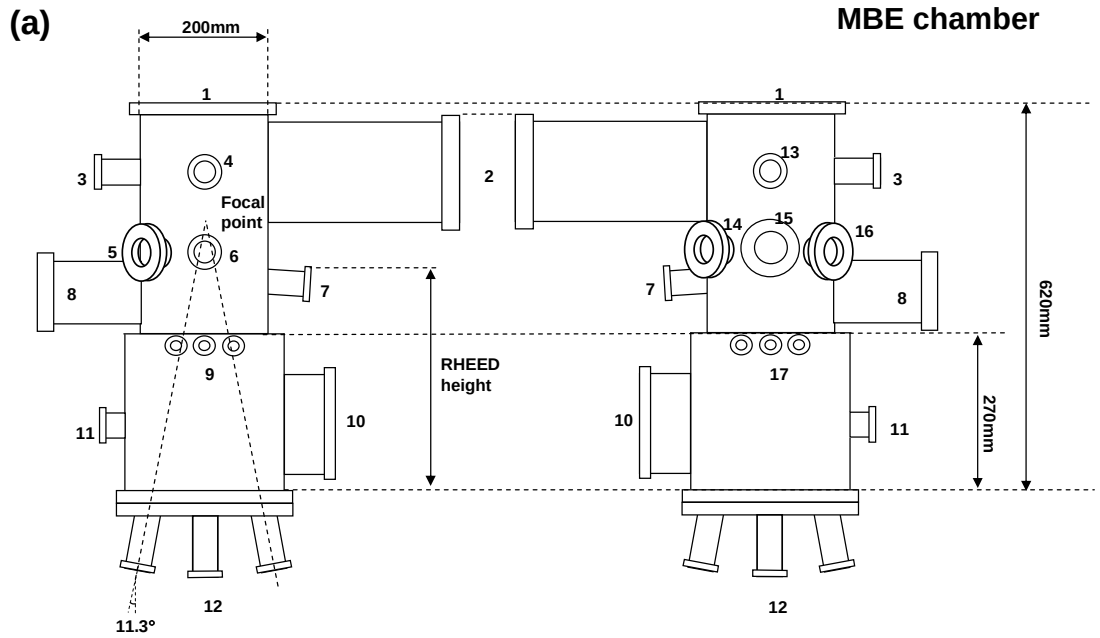

1. Manipulator
2. TSP + cryo-panel
3. Residual gas analyser
4. empty
5. Window
6. STM chamber entry
7. Electron gun
8. Phosphor screen
9. Cell shutters
10. Ion pump
11. Ion gauge
12. Effusion cells
13. Empty
14. Retractable beam flux gauge
15. Window
16. Empty
17. Cell shutters

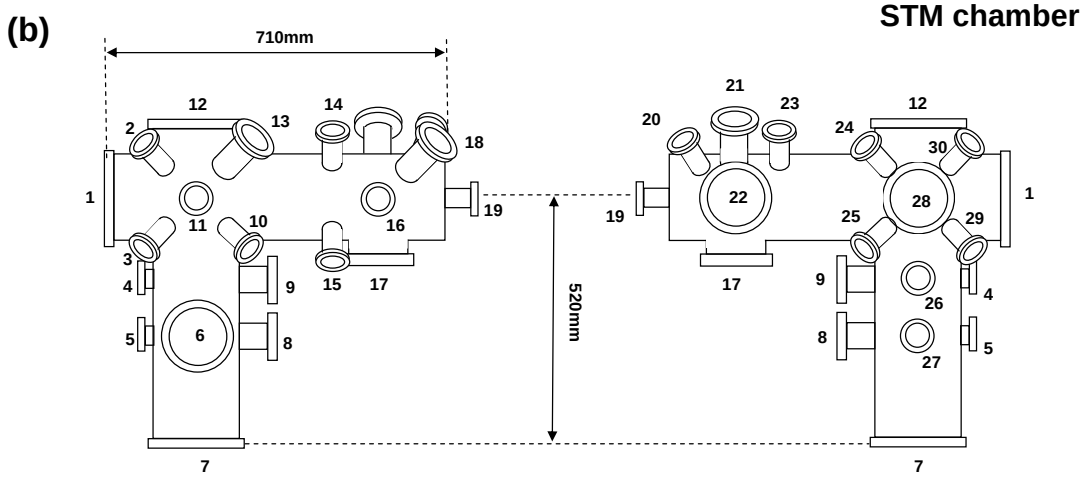

1. STM
2. Residual gas analyser
3. Ion gauge
4. Empty
5. Empty
6. Turbo pump
7. Titanium sublimation pump
8. Empty
9. Empty
10. Transfer arm earth
11. Transfer arm to MBE
12. Window
13. Window
14. Window
15. Ion gauge
16. Load lock
17. Ion pump
18. Window
19. Transfer arm
20. X-ray gun
21. Analyser
22. Cluster flange with electron gun and ion gun
23. e-beam heater
24. Empty
25. Empty
26. Empty
27. Empty
28. Gate valve to MBE chamber
29. Empty
30. Empty

Figure 2.1: Schematics of the MBE and STM chambers. Both chambers are shown from both sides.

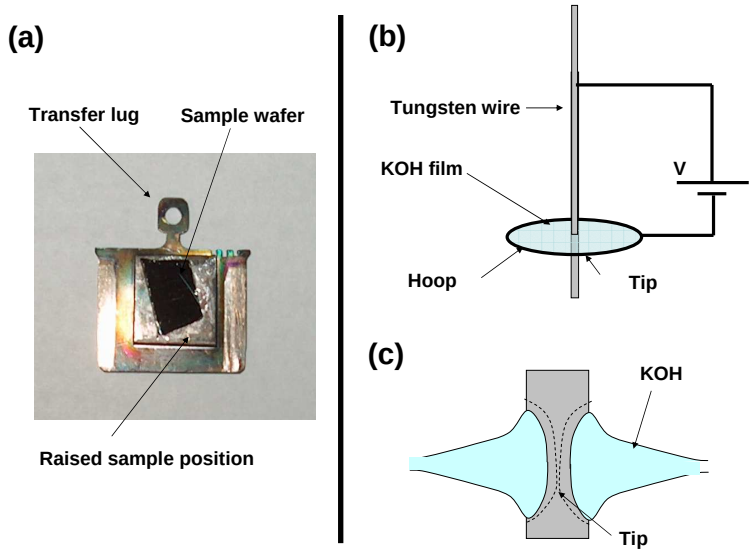

Figure 2.2: (a) Sample plate (b) tip etching setup (c) close view of etching

temperatures by surface tension. After mounting, the wafers are cleaned by rinsing in acetone, isopropanol and de-ionized water, and then dried under nitrogen in order to remove dust and debris from the wafer surface. In some cases debris had to be removed by gentle wiping of the surface using a cotton bud and acetone. These cleaning processes were found to be essential, since even small pieces of debris on the surface resulted in large regions of disrupted growth after MBE. No further chemical pretreatment was used.

2.2.2 Tip etching

Tungsten STM tips were prepared ex situ by electro-chemical etching. A 1.5 molar solution of KOH was used as a film spread within a hoop on the tip etching equipment and connected to the negative terminal of a power supply. Tungsten wire (0.4 mm diameter) was fixed through the middle of the hoop and KOH film, and connected to the positive terminal of the power supply. The setup is illustrated in Figure 2.2b. As the wire is etched away, the bottom section falls off and may be used as a tip. As a result of the shape of the meniscus of the KOH film around the tungsten wire, the etched wire forms an ideal tip shape, illustrated by dashed lines in Figure 2.2c. Ideal tips are sharp, but without a high aspect ratio which could result in tip vibrations,

hindering STM imaging. After drop-off, the tips are rinsed in de-ionised water to remove any remaining KOH. Tips are then crimped into tip holders, and transferred into the vacuum system on specially modified sample plates. Further in situ tip preparation is achieved by ion bombarding and high temperature annealing by e-beam heating. Success rate for tip preparation is low, with less than 50% allowing atomic steps to be resolved, and considerably less providing atomic resolution.

2.2.3 Sample preparation for cross sectional scanning electron microscopy

Cross sectional SEM allows for sample thickness and gross interface quality to be judged. In order to obtain a cross section, samples were cleaved by scoring the underside of the wafer with a diamond scribe, and cleaving towards the over-layer. For III-Vs, the cleavage planes are the nonpolar $\{110\}$ surfaces. The newly cleaved surface is then placed in the SEM in a modified sample holder and the edge imaged as normal. Since the cleave is a highly destructive process, large regions of the over-layer are disrupted either by delamination of the over-layer from the substrate or regions of debris making the layer thickness hard to measure. In all samples, regions of relatively undisturbed over-layer material were found by scanning along the length of the sample. Transmission electron microscopy (TEM) can be used to observe layer thickness in addition to detailed examination of interface quality and epitaxial orientation. However, sample preparation for TEM is considerably more time consuming, and for these studies the cross sectional SEM has been sufficient for growth layer thickness determination.

2.3 Effusion cell calibrations

The MBE chamber contains three effusion cells containing In, Sb and Mn. The Mn and In fluxes from the cells are atomic beams, while the Sb flux is predominantly Sb_4 molecules. All cells are either home-made or refurbished and hence require characterisation. The source material for each cell is held in a pyrolytic boron nitride crucible which is radiatively heated by either tungsten (the In and Sb cells) or graphite (Mn cell) filaments. The temperature of each cell is monitored by a thermocouple in contact with the base of the crucible. The temperature of the cells are controlled using Eurotherm controllers operating using PID (proportional, integral, derivative) feedback algorithms

and supplying a 0-10 V control voltage to the cell power supplies. The beams are controlled by rotary shutters above the cryo-panel, which are operated manually.

Evaporation (from the In source) or sublimation (from the Mn and Sb sources) in UHV results in a molecular beam, the beam equivalent pressure (BEP) of which is predicted by the Clausius-Clapeyron equation (Equation 1.7) described in Section 1.4.2. BEPs are determined from the difference in pressure measured by a retractable beam flux ionization gauge (BFG) positioned in the molecular beam approximately 140 mm above the cells and the ion gauge behind the water tank (♯11, Figure 2.1). BEP vs. thermocouple temperature calibrations for the three cells are shown in Figure 2.3. The panels on the right side of the figure show Arrhenius plots for the cells, the gradient of which provides $-\Delta H/R$. The black lines in the plots show the gradient expected for quoted values of ΔH for the appropriate material, while red lines show the best fit to the data.

The beam pressure calibrations agree with the exponential behaviour of the Clausius-Clapeyron equation, although the fitted (red) lines show a deviation from the constrained (black) lines. This is most likely due to a temperature discrepancy ($\Delta T = T_{\mathrm{S}} - T_{\mathrm{TC}}$) between the thermocouple temperature (T_{TC}) and the source material temperature (T_{S}) as a result of poor thermal contact between the thermocouple and crucible or temperature gradients across the cell. It is straightforward to calculate ΔT, which is $+55^{\circ}$C for the Mn cell, $+63^{\circ}$C for the Sb cell and $+111^{\circ}$C for the In cell. In all cases this discrepancy corresponds to the source material being at a higher temperature than the thermocouple, consistent with imperfect thermal contact between the thermocouple and crucible. Despite the temperature discrepancy, all cells exhibit controllable beam pressures in the desired range (10^{-8} to 10^{-6} mbar), which were stable within 5% over the period of an experiment (a number of hours). However, over a period of months the calibrations changed slightly, requiring regular re-calibration.

The pressure measured by the ionisation gauge corresponds to the current of ionised molecules flowing to a collector wire in the gauge, and is expressed as a pressure assuming that all molecules ionised are nitrogen (nitrogen equivalent pressures). The sensitivity to different molecules is related to their relative ionisation cross section, and therefore the number of electrons in the molecule [75]. For the materials used in this

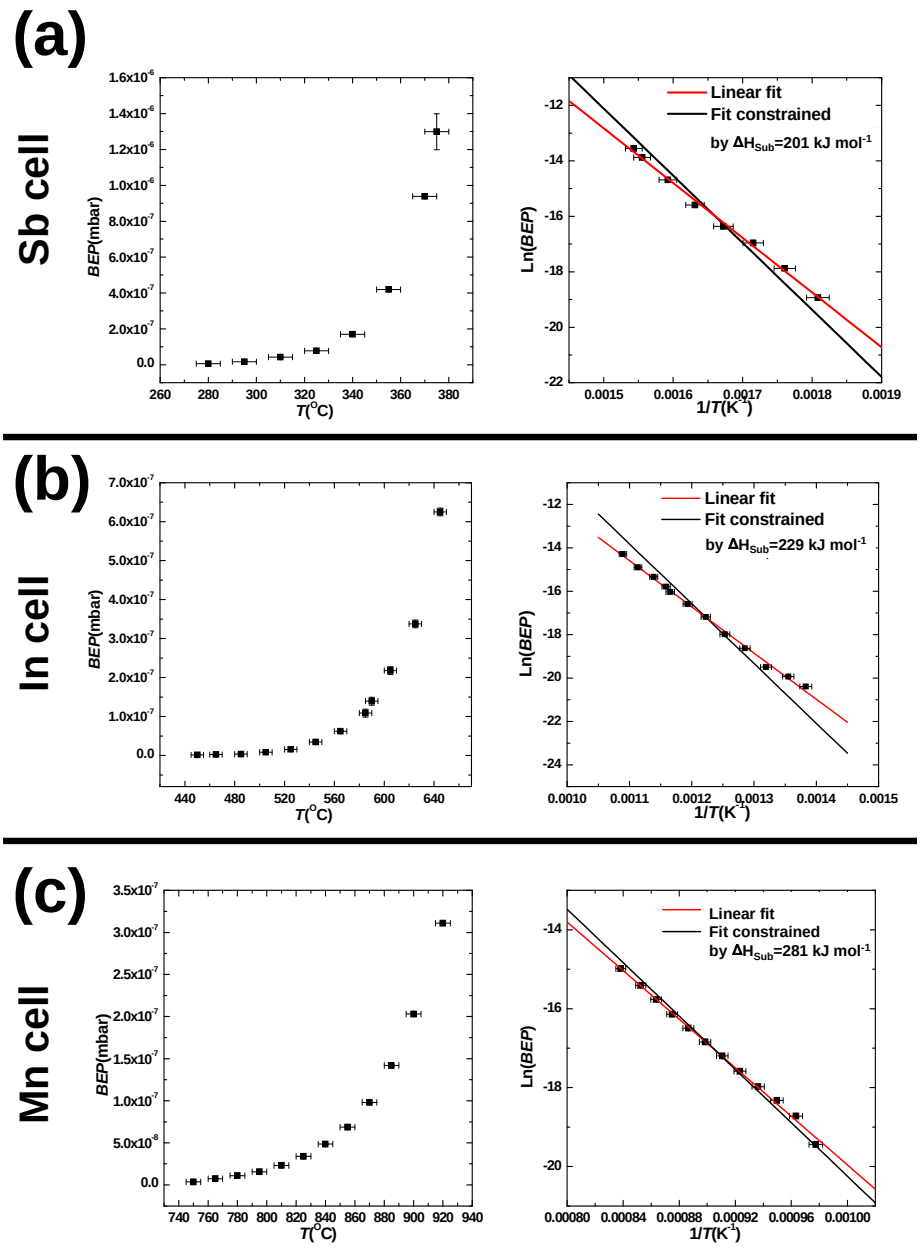

Figure 2.3: Effusion cell calibrations for (a) Sb cell (b) In cell and (c) Mn cell. Each panel shows BEP vs. T and the calculated Arrhenius plot showing linear fits (red lines) and fits constrained by the appropriate values of ΔH_{sub} or ΔH_{evap} (black lines).

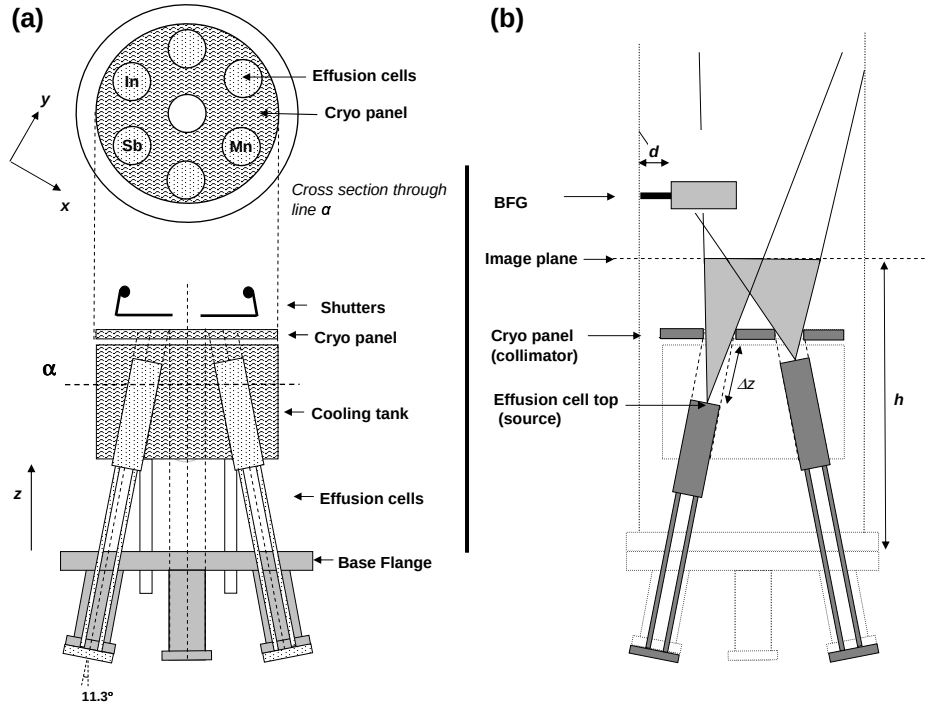

Figure 2.4: (a) Layout of the base flange, effusion cells and cooling shrouds (b) simplified diagram showing the collimated beams from two effusion cells at different Δz (only the beam from one point source per cell is shown).

thesis, the sensitivities, relative to N_2 are $S_{\mathrm{In}} = 2.3$, $S_{\mathrm{Sb}} = 2.4$, $S_{\mathrm{Sb_4}} = 8.2$ and $S_{\mathrm{Mn}} = 1.4$. Throughout this thesis pressures given are nitrogen equivalent pressures, and the appropriate sensitivities are only incorporated when growth rates are derived.

In addition to the beam pressure calibrations, flux uniformity is of great importance for MBE in order to grow consistently homogeneous layers. The layout of the cells and cooling shrouds are illustrated in Figure 2.4a. In order to examine the flux uniformity of the chamber, the flux from each cell was simulated using a Matlab program created by the author. Each cell was treated as 49 point sources distributed evenly across the cell surface. All sources are located at a height Δz below the cryo-panel, which acts as a collimator for the beams. Heights for the cells are $\Delta z_{Sb} = 50$ mm, $\Delta z_{In} = 100$ mm and $\Delta z_{Mn} = 100$ mm. Figure 2.4b shows the main features of the beam flux from two cells at different distances from the cryo-panel. The flux at each point on an image plane at height h from the base flange was calculated depending upon the line of sight from each point source, adjusted for a cosine dependence on the emergence angle. This model provides a series of 2D flux maps at varying heights

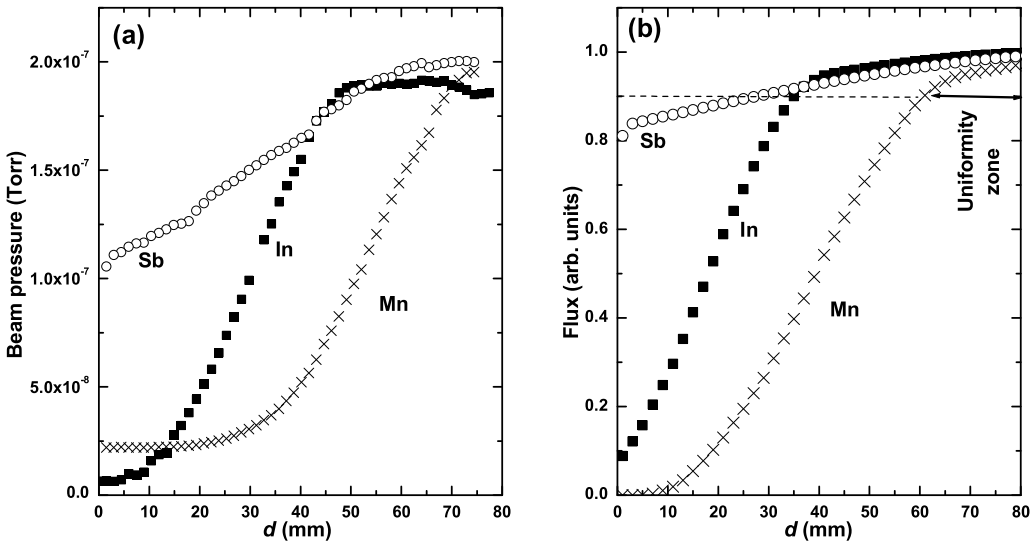

Figure 2.5: Beam flux profiles for the effusion cells (a) measured experimental using the BFG and (b) simulated.

for each cell. In order to verify the accuracy of this simple model, experimental beam flux profiles for the cells were compared to the simulated BFG profiles. To obtain each point in the simulated BFG profile, a 2D section of the simulated flux map was summed over an appropriately positioned rectangular area of 30 mm $\times$20 mm to represent the detection zone of the BFG at a position d from the side of the chamber (as illustrated in Figure 2.4b). Experimental values were obtained by measuring the pressure of the BFG at different positions, d(mm) from the side of the chamber. The profiles and the simulations are shown in Figure 2.5. The qualitative agreement is good, with the Sb flux showing the broad peak predicted, and sharper peaks for the In and Mn cells. The simulation also predicts well the difference in position of the onset of the In and Mn flux peaks. The reason for the remarkable difference between the Sb compared to the In and Mn profiles is the shorter distance between the Sb cell and the aperture in the cryo-panel (Δz_{Sb}), resulting in a less collimated beam. It is apparent that flatter, more uniform beams may be obtained at some future date by extending the In and Mn cells towards the cryo-panel and hence reducing the collimating effect.

Having verified that the simple line of sight model for the fluxes is in reasonable agreement with the actual beam fluxes, the program was used to calculate the 'uniformity

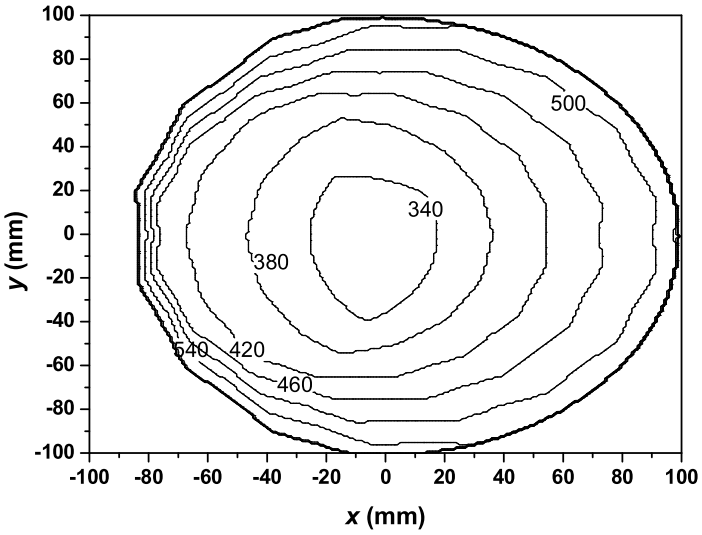

Figure 2.6: Uniformity zones for the effusion cells at different chamber heights. Contours from the center outwards contain the uniformity zones at height $z = 340$ mm, 380 mm (RHEED height), 420 mm, 460 mm (focal point), 500 mm and 540 mm.

zone' of the chamber at different heights. The 'uniformity zone' is defined as the zone in which the beam flux from each cell is greater than 90% of the maximum value. This is illustrated in Figure 2.5b. Within this region, there should be no strong flux variations and hence more uniform growth should be achieved. The uniformity zones at different chamber heights are illustrated in Figure 2.6.

Figure 2.1a shows the focal point of the cells (at a height of 460 mm above the base flange), which should correspond with the height at which a sample can be viewed with RHEED (380 mm above base flange, also illustrated in Figure 2.1a) in order to allow RHEED observation of the surface during growth. These two heights differ by 80 mm which is believed to be a design error from when the chamber was first built in 1982. From Figure 2.6, it is possible to observe the difference between growing at the focal point and growing at the RHEED height. At the focal point, the width of the uniformity zone is 190 mm, while at RHEED height it is only 70 mm. This is a dramatic reduction, although since samples are only 10 mm $\times$ 10 mm, the uniformity zone at RHEED height is sufficiently large to ensure that the fluxes across the sample are uniform. One point to note is that as a result of the asymmetric cell positions, the uniformity zone at RHEED height is not centered at the center of the chamber, but

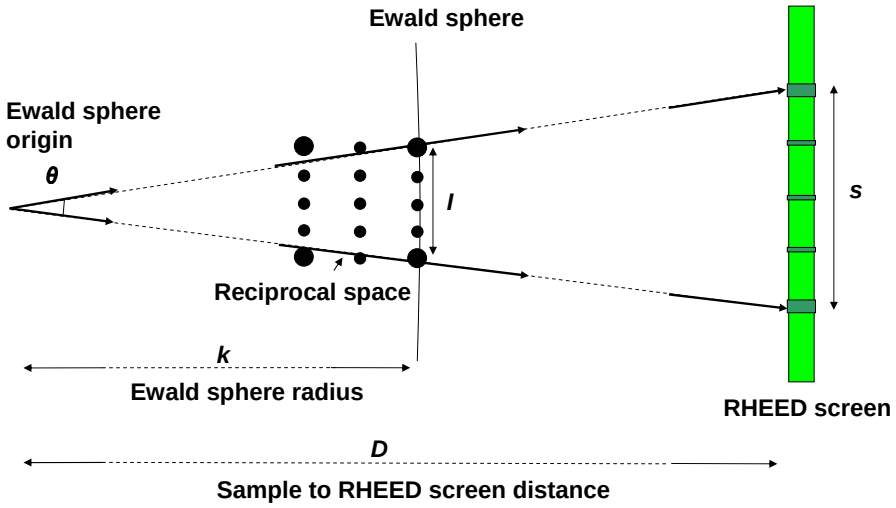

Figure 2.7: RHEED geometry showing the correspondence between the Ewald sphere construction in reciprocal space (left hand side) and the diffracted beam directions and RHEED pattern in real space (right hand side). Variables are the divergence angle (θ), Ewald sphere radius (k), sample to RHEED screen distance (D), reciprocal lattice spacing (I) and integer order streak spacing on the screen (s).

shifted towards the Sb cell.

2.4 Reflection high energy electron diffraction calibrations

As described in Section 1.4.3, the pattern observed on the phosphor screen of a RHEED system indicates the sample's bulk-like and surface periodicities in the form of integer and fractional order streaks respectively. It is therefore possible, given the appropriate calibration, to ascertain the in-plane lattice parameter of the material from the integer order spacings in the RHEED pattern. From the Ewald sphere construction described earlier, the divergence angle (θ) between two diffraction beams passing through adjacent reciprocal lattice sites at the edge of the Ewald sphere is given by

$$\theta \simeq \frac{I}{k} \tag{2.1}$$

Here, I is the reciprocal lattice spacing ($\sim 10^{10}$ m^{-1}), k the wave vector of electrons in the RHEED beam ($\sim 5{\times}10^{11}$ m^{-1}) calculated from the electron energies, and the small angle approximation is used. It is this divergence angle which determines the separation

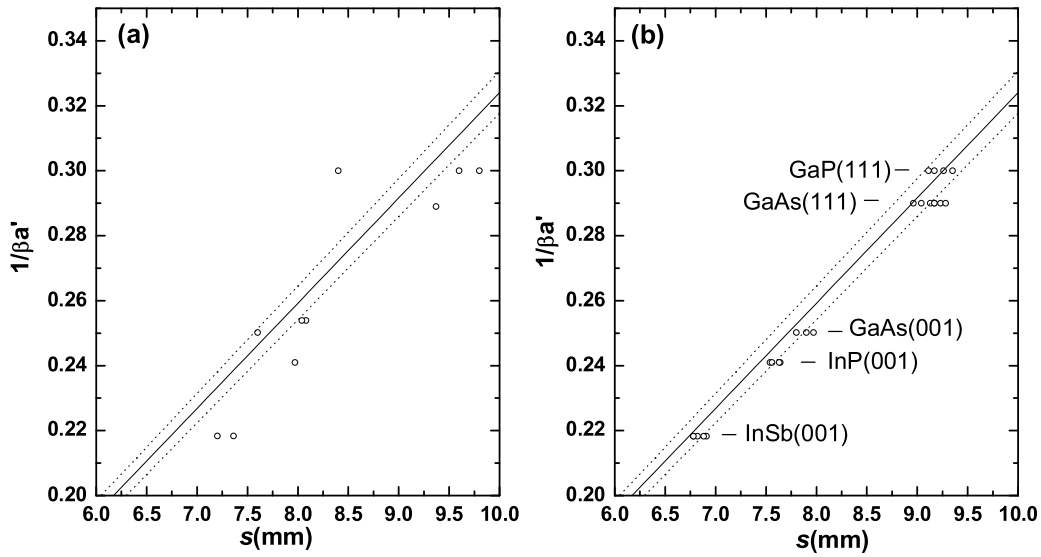

Figure 2.8: RHEED calibration graph (a) before and (b) after improvements to measuring technique. Axes are the experimentally measured integer order spacings (s) and $1/\beta a'$, where $\beta = \sin\theta$, and a' is the expected surface unit vector. The solid line shows the theoretical values ($\alpha = 30.86$) and the dotted lines indicate the error margin expected due to variations in sample positions and electron energies.

of the integer order streaks on the RHEED screen (s) at a distance D from the sample.

$$s = \theta D \tag{2.2}$$

Figure 2.7 shows the correspondence between the Ewald sphere construction in reciprocal space (left hand side), and the electron beam diffraction onto the RHEED screen in real space (right hand side). From this relation,

$$I = \frac{sk}{D} \tag{2.3}$$

The relationship between I and the real space distance being observed (a') depends upon the lattice type. Generally, for a lattice with primitive unit vectors with an angle ϕ between them, the relationship is

$$I = \frac{2\pi}{\sin\phi a'} \tag{2.4}$$

Hence, the lattice parameter determined by RHEED (a'), may be expressed as

$$a'(\mathring{A}) = \frac{\alpha}{\beta s(mm)} \tag{2.5}$$

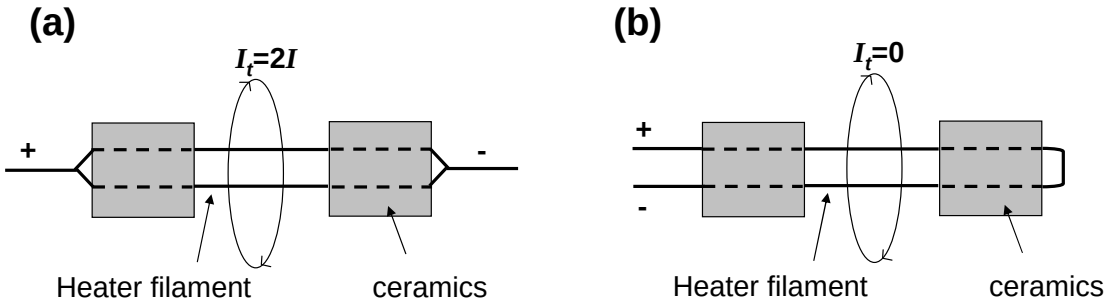

Figure 2.9: Wiring for the filament in the radiative sample heater on the MBE manipulator. (a) Design 1- suffers from radial magnetic field. (b) Design 2- eliminates the radial magnetic field.

In this equation

$$\beta = \sin\phi \tag{2.6}$$

$$\alpha = \frac{2\pi \times 10^{13} D(m)}{k(m^{-1})} \tag{2.7}$$

The value for β is dependent only upon the crystal structure, while α depends upon chamber dimensions and operating conditions, and has a theoretical value for this MBE-STM chamber of 30.86 (D = 280 mm, k = 5.7×10^{11} m^{-1} for an accelerating voltage of 12.5 kV).

Most III-V semiconductor surfaces have lattice parameters between ∼5.4 Å (GaP) and ∼6.5 Å (InSb). This in turn means the expected RHEED spacings are in the range ∼ 6mm-10mm for this RHEED system. In order to distinguish accurately between the different lattice parameters, images of the patterns were obtained using a basic digital camera (HP photosmart 935). A Matlab program written by the author (RHEEDprofile.m, shown in Appendix B) was used to measure a green colour intensity profile horizontally across the image. This allows accurate determination of the spacing between integer order streaks (in pixels). In order to relate the digital image to real space distances, a calibration distance of known size is measured in addition to the streak spacings. Initially, two defects on the RHEED screen (horizontal separation 23 mm) were used as these could consistently be observed in the low light conditions. However, this was found to give a large error in the lattice parameter calculation (see Figure 2.8a) as a result of their relatively small separation. This was improved by fixing two fluorescent

markers to the edge of the screen with a large (150 mm) separation and using them as the reference distance. This was found to give far superior measurements, illustrated in Figure 2.8b. The solid line in the figure shows the theoretical values (using $\alpha = 30.86$), while the dotted lines show the maximum predicted errors as a result in variations in sample positions and electron gun energies. Using the improved measurement method, the experimental values for a range of materials fall within the predicted errors, and so lattice parameters are estimated to have errors of the order of 5%.

As a consequence of the original manipulator heater filament design (Figure 2.9a), a radial magnetic field surrounding the sample interfered with the RHEED beam, resulting in beam deflection and oscillations when the sample temperature was reaching the set-point value. In order to eliminate this effect, a simple alteration to the filament wiring was implemented (Figure 2.9b). While some small fields no doubt remain, this new arrangement ensures that the magnetic fields do not affect the RHEED measurements significantly.

During layer by layer MBE growth of certain materials, periodic changes in the surface condition (terrace size and step density) between fully and fractionally completed mono-layers results in a periodic change in the RHEED intensity. This is commonly used as a growth rate calibration tool. For materials such as InAs [76], these RHEED oscillations are strong, and they have also been observed on MnAs(0001) layers grown on GaAs(111)B [77]. At present, measurements of RHEED oscillations have not been attempted on this system, and it is not known if measurable oscillations occur for MnSb.

2.5 Epitaxial growth calibrations

In order to check the In and Sb effusion cells and sample heater calibrations, a material which is both well known and compatible with the system was required for calibration experiments. The obvious choice for this was InSb. Three low index planes of InSb namely (001), (111)A and (111)B, are well cited in the literature, and with the possible exception of the (001) c(8×2), the surface reconstructions are well established. A common experiment on an epitaxial growth system is to map the different reconstructions obtained under different conditions. Typically 2D "phase maps" of substrate temperature (T) against BEP ratios ($J_{\mathrm{V/III}}$) are produced in such studies

[78, 79, 80]. Numerous phase maps for the InSb surfaces exist, and make it a good calibration tool for this system.

InSb(001), (111)A and (111)B phase maps were obtained during InSb homoepitaxy. InSb was grown on InSb wafers (Wafer technology Ltd., UK) attached to sample plates as described in Section 2.2. The surface reconstructions were determined by RHEED during growth. At the time of these experiments (2003-2004), the sample was conductively heated operating in a constant current mode rather than temperature stabilised feedback mode which was later introduced. The substrate temperature is estimated to have an systematic error of as much as 50°C as a result of the thermocouple position compared to that of the sample, and a further random error of $\pm$ 10°C due to varying thermal contacts between manipulator and sample plates, and heater variations. Figure 2.10 shows the experimental phase maps obtained from the three substrates, in addition to reference phase maps presented by Noreika *et al.* [78]. The agreement for all three phase diagrams is good. The InSb(001) surface demonstrates the most reconstructions, with the In rich c(8×2) [44] at BEP ratios of $J_{Sb/In}$ <1. The main Sb rich reconstruction is the c(4×4) [40], although it should be noted that this has been labelled $(\sqrt{2} \times \sqrt{2})45°$ in the reference figure. In the text of the paper by Noreika *et al.* [78], this reconstruction is identified as a $(2\sqrt{2} \times 2\sqrt{2})45°$, which is equivalent to a c(4×4) as illustrated in Figure 1.2. At higher temperatures, an asymmetric (1×3), denoted a(1×3) is observed, while at low temperatures the RHEED pattern is (1×1). In these experiments, it was not possible to observe a sharp transition between the c(4×4) and the a(1×3) as observed by other groups [78]. Instead a c(4×4)/a(1×3) transition region was observed (indicated by horizontal arrows in Figure 2.10). In this region, both reconstructions were observed in a mixed domain structure. The transition also demonstrated some degree of hysteresis with increasing and decreasing temperature. This may indicate slight instabilities or variations in the sample temperature.

The InSb(111)A phase diagram shows two regions, the In rich (2×2) [41] at low BEP ratio ($J_{Sb/In}$ <2) and high temperature (T_{sub} >350°C), and the $(2\sqrt{3} \times 2\sqrt{3})$R30° at high BEP ratio and low temperature [43]. This reconstruction is sometimes labelled (2×6) with reference to the periodicities observed in the two high symmetry directions. Again this agrees with Noreika *et al.*, although the temperature of the phase transition deviates by approximately 25-50°C. Finally the InSb(111)B surface shows three regions.

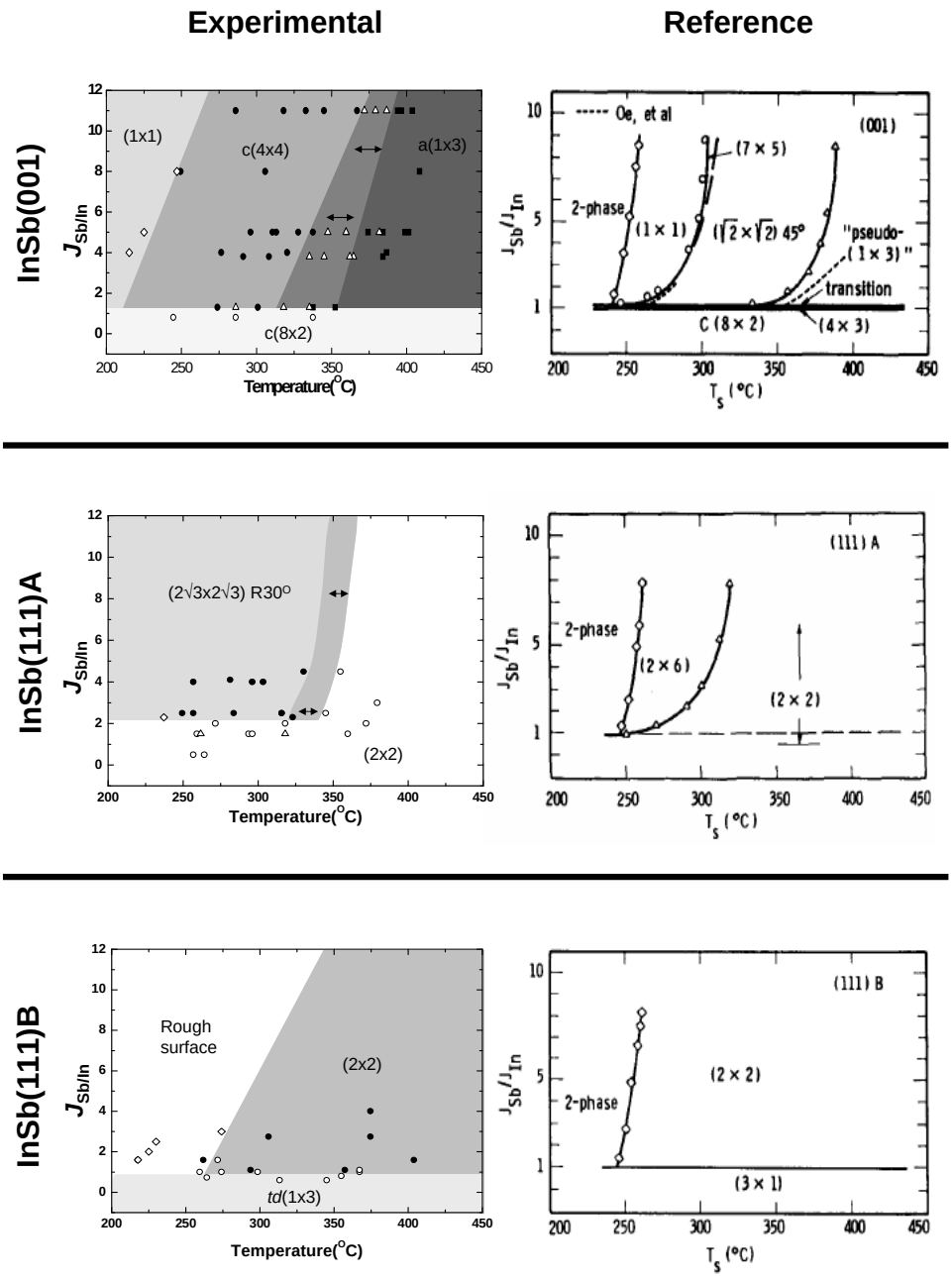

Figure 2.10: InSb phase diagrams indicating RHEED patterns obtained during growth by MBE for the (001), (111)A and (111)B surfaces. Shaded areas indicate the different phases, although boundaries are not exact. Transition regions are labelled with arrows. Symbols represent: (open circle) In rich reconstruction, (filled circle) main Sb rich reconstruction, (diamond) low temperature Sb rich reconstruction, (filled square) high temperature Sb rich reconstruction, (triangle) transition region. Reference phase diagrams are reproduced from work by Noreika *et al.* [78]. Note that the notation used by Noreika *et al.* is that J is a BEP rather than a BEP ratio.

The In rich regime has a $td(1\times3)$ reconstruction while a (3×3) can be obtained after IBA cleaning [81]. In the Sb rich regime, a (2×2) [41] reconstruction is seen at high temperatures and at low temperature a 'rough surface' is observed where the RHEED pattern deteriorated considerably.

For the three InSb surfaces, all the main phases have been observed in the present work with the correct T vs $J_{\mathrm{Sb/In}}$ characteristics. There are some issues which arise from the difference in temperature and sharpness of a number of the transitions in the experimental phase maps. While systematic temperature differences are expected for UHV temperature calibrations, the large transition region between the c(4×4) and a(1×3) phases on InSb(001) is a cause for concern. Since these experiments were carried out, a number of improvements have been made to the sample heater filament and controller. The heater now operates radiatively for more uniform heating, the thermocouples have been positioned closer to the sample, and the heating is now temperature controlled by a feedback loop using one thermocouple. These changes have improved the temperature stability considerably, although any effect on the width of the InSb(001) c(4×4)/a(1×3) transition region has not been studied at this time.

2.6 Scanning tunnelling microscope calibration

The electronics and computer interface for the Omicron STM-1 used in this thesis have been designed and built by Nanograph Systems Limited (Nottingham, UK). Since the control system has been designed specifically for the Omicron STM-1, and is an entirely new product, the STM images have been calibrated carefully. The latest version of the software (Nanograph Studio version 1.6.2252.31545), was installed in March 2005. With appropriate tip and sample preparation, the STM system has reliably provided images showing atomic steps and terraces. To date, the STM has been used primarily to study growth morphology, and so few atomic resolution images have been obtained. Figure 2.11a shows a 1000 Å × 1000 Å STM image of the InSb(001) c(8×2) surface. As expected for this anisotropic surface, preferential step edges are aligned along two perpendicular directions, $<110>$ and $<1\bar{1}0>$. This image also shows some indications of atomic scale features, with lines running along the $[1\bar{1}0]$ direction. These lines are not caused by noise, which is checked by changing the scan speed and observing no change to

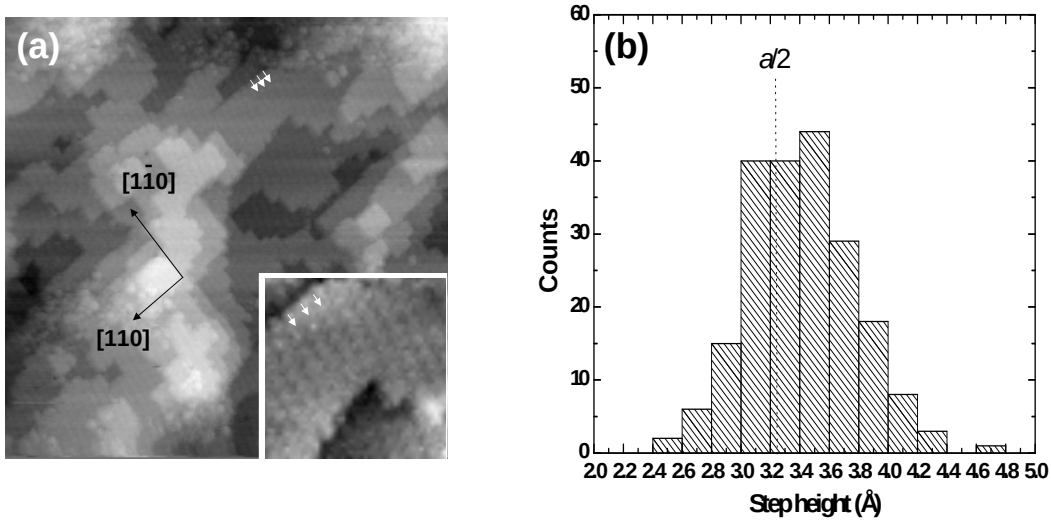

Figure 2.11: (a) 1000 Å $\times$ 1000 Å STM image of the InSb(001) c(8$\times$2) surface. Preferential step directions are aligned along the [110] and [1$\bar{1}$0] directions. Atomic resolution is visible as a series of parallel lines along the [1$\bar{1}$0] direction, and the periodicity in the [110] direction is indicated by small white arrows. The inset shows a zoomed image of these atomic features. Panel b shows a histogram of the InSb(001) surface step height determined from STM images. The ideal step height $a/2 = 3.23$ Å is indicated, while the mean of the experimental distribution is 3.4 Å.

the line direction or spacing. The spacing of the lines (indicated by small white arrows) is determined to be $\sim$ 19 Å, in good agreement with a 4$\times$ periodicity of the InSb surface (18.3 Å). These STM observations are consistent with those of Schweitzer *et al.* [82] and McConville *et al.* [83]. Over the entire image, the 90° angle between step edges is maintained with only small deviations due to thermal drift. The in-plane x and y piezo motion is therefore well calibrated. In order to measure the calibration of the z motion, the heights of a large number of InSb(001) steps have been measured. The results are shown in Figure 2.11b. The mean of the experimental distribution (3.4 Å) is slightly higher than the ideal step height ($a/2 = 3.2$ Å), although the distribution is rather broad, with a standard deviation of 0.4 Å. This broad distribution is believed to be a result of the rather simple method of measuring step heights on the Nanograph Studio software, namely measuring the displacement between two points. This results in errors due to noise, imperfect feedback settings overshooting the step edge or blurring of the step edge due to relatively blunt tips. These errors will be reduced by future improvements to the analysis capabilities of the Nanograph software. Such improvements could include user

defined plane subtraction, and the ability to measure the distance between two parallel lines fitted to the terraces. Currently, in order to obtain meaningful step heights from STM images, the average of a number of step heights must be obtained to take into account the large variation in measured values.

2.7 Additional Systems

The main shortcoming of the MBE-STM chamber used for this project is the lack of chemical analysis, since it has not been possible to make the XPS system operational. In order to complement the in situ analysis carried out in the principle system, two additional systems were used for XPS measurements. The first is an XPS system in Warwick equipped 450 W X-ray gun (VG, UK) operating at 15 kV and using the Mg Kα line. The electron energy analyser is a concentric hemispherical analyser (CHA) with hemisphere radius 100 mm, and electron multiplier operating typically at 2.2 kV. This system is rather temperamental, and occasionally gives rise to spikes in the data, and high noise at binding energies above 700 eV. Resolution of this system is quoted as 0.6 eV for 25 eV pass energy. The second system used for XPS is the Scienta ESCA300 at the National Centre for Electron Spectroscopy and Surface Analysis (NCESS) at Daresbury Laboratory, UK. This is a high resolution instrument with a high power (8 kW) monochromatic Al Kα (1486.7 eV) X-ray source with rotating anode. The analyser is also a CHA with hemisphere radius 300 mm. Overall resolution of the system is 0.3 eV. The system has a separate preparation chamber with ion gun and sample heater. Elemental peak ratios have been obtained using both chambers for the same sample, and the results found to be comparable within experimental accuracy of 5%. Data obtained on the two systems used for peak area analysis have not been distinguished in this thesis. All fitted peaks were obtained at the NCESS facility.

SEM and magnetic measurements were all carried out in the Department of Physics, University of Warwick. The SEM was performed on a ZEISS SUPRA55VP SEM system operating with an accelerating voltage of 10 kV. Magnetic measurements were carried out using a vibrating sample magnetometer (VSM- Oxford Instruments, UK) with 12 T superconducting solenoid and the MPMS-5S superconducting quantum interference device (SQUID- Quantum Designs, UK) with a 2-400 K temperature range.

All samples analysed by SEM, XPS, VSM and SQUID magnetometers were subject to air contamination following removal from UHV. For the magnetic and SEM experiments, this was of little consequence, although for XPS it is an important issue. More details regarding this matter are discussed in the relevant sections of this thesis.

Chapter 3

Heteroepitaxial growth of MnSb on GaAs

3.1 Introduction

This chapter is the first heteroepitaxy study on the newly commissioned, custom built MBE-STM system described in Chapter 2. The first materials system described in this thesis, namely MnSb grown on a GaAs substrate (MnSb/GaAs), has been chosen due to the significant body of work already published on it (summarised in Table 1.4). This provides the opportunity to test the heteroepitaxial growth of MnSb and compare with existing results. In addition further calibration data of the growth chamber were obtained.

The frequent use of GaAs as a substrate for MnSb (and MnAs) growth is no doubt a result of the relatively high availability of GaAs compared to other substrates, in addition to the vast literature on GaAs preparation, cleaning, growth and properties. However, GaAs and MnSb have a rather large lattice mismatch (-3.2%) between GaAs $<110>$ and MnSb $<2\bar{1}\bar{1}0>$, and a structural mismatch for GaAs(001) substrates. Despite this mismatch, epitaxial layers of MnSb have been grown by MBE on both GaAs(111)B and (001) substrates. GaAs(111)B is a sensible choice for the first study, as the hexagonal (111) surface has been reported to promote well oriented MnSb(0001) growth. Although the MnSb/GaAs system has been studied in some depth, there is a substantial gap in the literature concerning the surface aspects of the over-layer, such as detailed surface reconstruction mapping. There is therefore value in further study of this combination of materials.

In the first part of this chapter, the general issues of growth of MnSb/GaAs(111)B are considered, including substrate cleaning, epitaxial orientation, and some optimisation

of growth conditions based on surface diffraction and growth rates. Following this, a set of standard growth conditions is determined, and these conditions are used throughout the remainder of Chapters 3 and 4. The over-layers are then characterised in more detail, including the growth mode, magnetic properties and valence band measurements. In the final section, preliminary results of MnSb/GaAs(001) growth are presented.

3.2 MnSb/GaAs(111)B

3.2.1 Surface preparation of GaAs(111)B

Before MnSb can be grown on GaAs(111)B, the substrate must be cleaned of native oxides and carbon present on the surface as a result of contamination of the wafers in air. This is achieved by ion bombarding and annealing (IBA). As a result of the high melting point (1240°C) of GaAs, this material can be annealed above the desorption temperature of the native oxides, and as a consequence is relatively easy to clean. In this thesis, all GaAs substrates (Si doped, Wafer technology Ltd., UK) 10 mm×10 mm were cleaned by degassing at 400°C for 1 hr, ion bombarding for 10 minutes, and finally annealing at 470°C for 20 minutes. The RHEED pattern observed after this cleaning process was td(1×3), characterised by a faint 3× periodicity with the beam along the <110> directions and a 1× in the $<\bar{2}11>$ directions. These RHEED patterns are shown in Figure 3.1. The expected RHEED pattern for GaAs(111)B is the (2×2), corresponding to the As trimer surface structure. Triple domain (3×1) has been observed previously on GaAs(111)B by Cafolla *et al.* [84]. This reconstruction was reported to be formed by annealing GaAs(111)B to 400-475°C in the presence of Sb, and was attributed to Sb chains on the surface following desorption of As trimers. It is possible that this assignment is applicable for the GaAs(111)B surface prepared in the current work, since is has been prepared in an Sb based MBE chamber, and some Sb background is expected. A second mention of 3× reconstructions on GaAs(111)B was a (3×3) observed in various studies of the GaAs(111)B surface [85, 86]. The RHEED pattern shown in Figure 3.1 is not consistent with a (3×3) reconstruction as a result of the 1× periodicity observed in the $<\bar{2}11>$.

In order to test for the presence of an Sb induced surface reconstruction, a GaAs(111)B sample cleaned by IBA in the Warwick UHV system was analysed by XPS

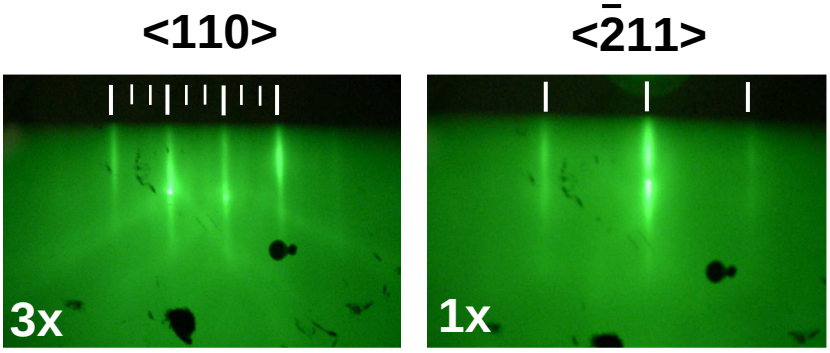

Figure 3.1: RHEED images of cleaned GaAs(111)B, with a $td(1\times3)$ reconstruction. The electron beam is aligned along the <110> and <$\bar{2}$11>.

at the NCESS facility (Daresbury laboratory, UK) in order to detect the Sb. XPS spectra for cleaned and uncleaned samples are shown in Figure 3.2a. The Ga and As 3d peaks are clear in both spectra, in addition to valence band features between 0 and 5 eV, and plasmon peaks from the Ga and As 3d peaks at 37 eV and 57 eV. A change in both Ga and As 3d peak shape as result of the cleaning process is apparent, with high binding energy 'shoulders' attributed to As and Ga oxides reducing for the cleaned samples. The oxide peaks do not disappear, although this is to be expected since the sample will re-oxidise during transfer between the Warwick MBE chamber and the NCESS chamber. Despite the oxidation, any Sb on the surface prior to contamination should be visible in the XPS spectra as a result of the high surface specificity of the technique. No indications of an Sb 4d peak at 32 eV was detected. For an Sb based (1×3) surface reconstruction there must be at least 1/3 ML of Sb on the surface, which would be easily observed by XPS if present, and so the surface obtained here is not believed to be that discussed by Cafolla *et al.*. At this stage of the growth studies, the identity of the surface reconstruction after cleaning is of secondary importance compared to the physical condition of the surface. For high quality epitaxial growth, an atomically smooth surface with no contamination is required. In order to asses the surface condition, a cleaned GaAs(111)B substrate was imaged in situ using STM. A 3000 Å × 3000 Å STM scan is shown in Figure 3.2b. The STM image shows a surface with large (500-1000 Å) terraces. The average step height was measured to be 3.0 Å, in good agreement with the theoretical value for GaAs(111) mono-layer steps of 3.2 Å. In future interface studies, it will no doubt become important to understand the surface reconstruction

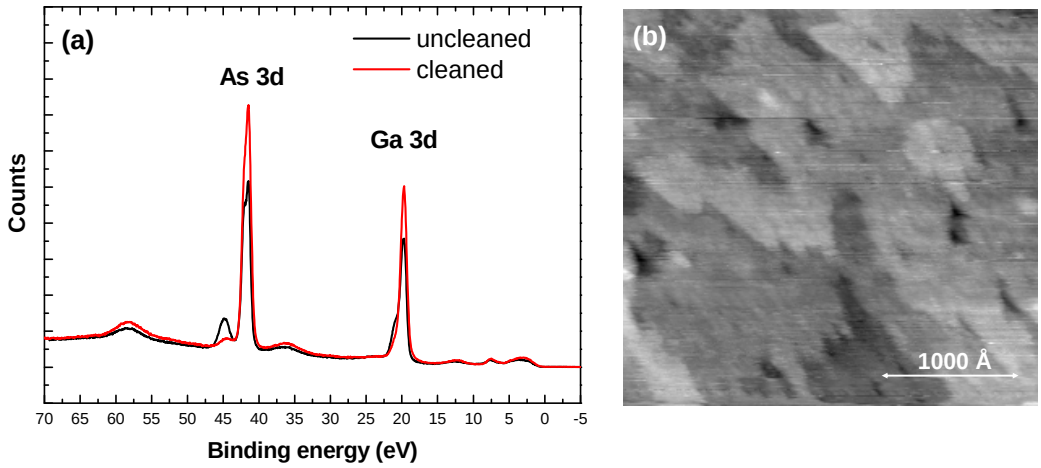

Figure 3.2: (a) XPS spectra of GaAs(111)B before (black line) and after (red line) cleaning by IBA. (b) 3000 Å $\times$ 3000 Å STM image of IBA cleaned GaAs(111)B. Tunnelling conditions used were V = -3 V and I = 0.2 nA.

obtained by the IBA process. For this work it is sufficient to note that the surface gives strong diffraction features, and is observed to be smooth by STM. It is therefore deemed to be suitable as a growth surface for these initial growth studies.

3.2.2 Growth of MnSb/GaAs(111)B

Although growth of MnSb/GaAs(111)B has been reported by a number of groups, growth conditions vary considerably (Section 1.6.2). Possible parameters for the growth include growth temperature, growth rate, flux ratio, substrate, substrate orientation, preparation and termination, post growth treatment and additional processes such as pre-layers, buffer layers and multi-stage growth. An exhaustive study of all these parameters would be enormously time consuming, and so in this work the primary three parameters are examined: the growth temperature (T), growth rate (GR) and BEP ratio ($J_{\mathrm{Sb/Mn}}$). From the literature, Sb rich growth is universally used, and typically temperatures in the range 200-500°C (Table 1.4). It is important to note that optimal temperatures in particular are susceptible to the calibration of different systems. In this section, GaAs(111)B substrates are used with the termination and preparation discussed previously. More complex processes such as pre-layers, buffer layers and multi-

stage growth are not considered in this work.

Experimental details

MnSb was grown on GaAs(111)B substrates under a range of substrate temperatures (T) and directly measured BEP ratios ($J_{\mathrm{Sb/Mn}}$). GaAs(111)B wafers were cleaned using the IBA process described in Section 3.2.1. The cleaned samples (characterised by a td(1×3) RHEED pattern) were cooled to the growth temperature, and left to equilibrate for 10 minutes. During this cooling, the RHEED continued to show a td(1×3). Growth was then initiated by opening both the Mn and Sb shutters simultaneously. Temperature and BEP ratios were changed systematically, and the RHEED patterns observed during growth were recorded. Samples were grown for between 30 and 60 minutes.

Growth surfaces and orientations

Under all conditions studied, the RHEED patterns during and after growth retained strong integer order streaks. Figure 3.3 shows RHEED patterns and profiles obtained from the GaAs(111)B substrate, and the MnSb over-layer with the electron beam aligned along two directions, denoted 0° and 30°. Integer and fractional order streaks are indicated by long and short lines respectively in the RHEED images. Integer order streaks are indicated in the profiles by arrows. The over-layer forms a surface structure with similar symmetry to the substrate, although from the profiles it is apparent that the integer order spacing in both the 0° and 30° directions decreases. This corresponds to an increase in the real space surface mesh size. Assuming a hexagonal structure, the lattice parameter obtained from the over-layer is 4.1 ± 0.2 Å. Both the lattice parameter and the hexagonal symmetry are consistent with a MnSb(0001) surface. Figure 3.4 illustrates the relative orientation of both real and reciprocal space for both the substrate and over-layer. The 0° and 30° directions are preserved in all panels. The shaded regions in the reciprocal space pictures indicate the recording plane of the RHEED screen when the electron beam is in the direction indicated by the attached arrow. Hence, for the GaAs(111)B substrate, aligning the electron beam along [$\bar{1}$10] (0°), a 3× periodicity is observed. All the features in the RHEED images in Figure 3.3 are accounted for by Figure 3.4. Epitaxial orientations for MnSb/GaAs(111)B are

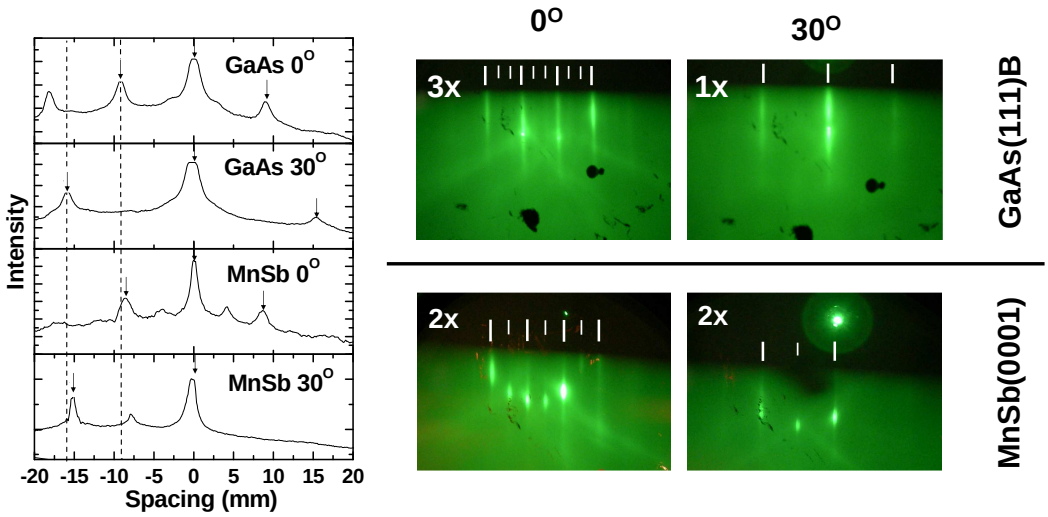

Figure 3.3: RHEED profiles and images for GaAs(111)B $td(1\times3)$ substrate and MnSb(0001) (2×2) over-layer. RHEED images are shown with the electron beam along two directions, 0° and 30° shown in Figure 3.4. Integer order peaks in the RHEED profiles are indicated by arrows. Integer (fractional) order streaks in the RHEED images are indicated by long (short) lines.

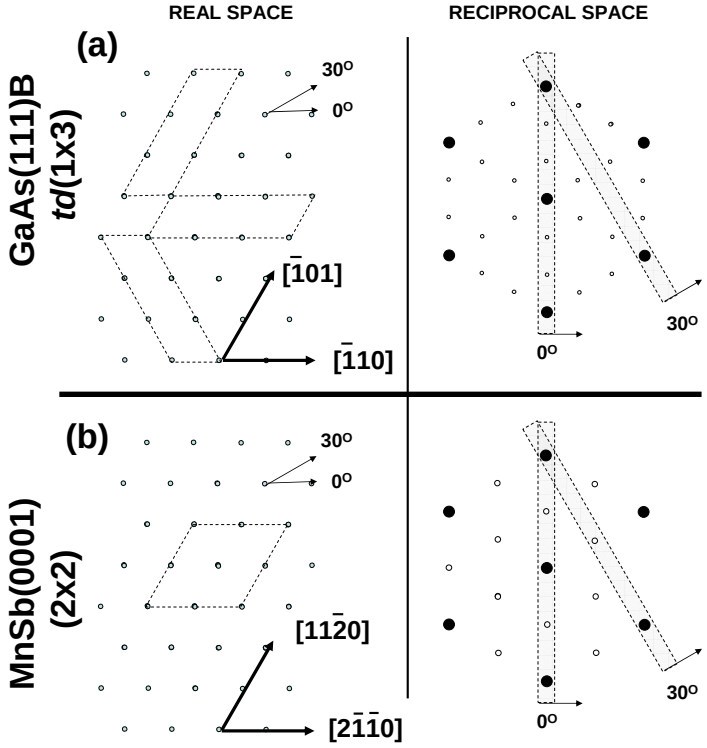

Figure 3.4: Epitaxial orientation of MnSb(0001) grown on GaAs(111)B. Panels indicate the relative orientations of real space (left) and reciprocal space (right). The shaded regions in the reciprocal space panels indicate the recording plane of the RHEED when the electron beam is in the direction indicated by the attached arrow. The solid (empty) circles indicate integer (fractional) order diffraction features. Directions are consistent across all the panels.

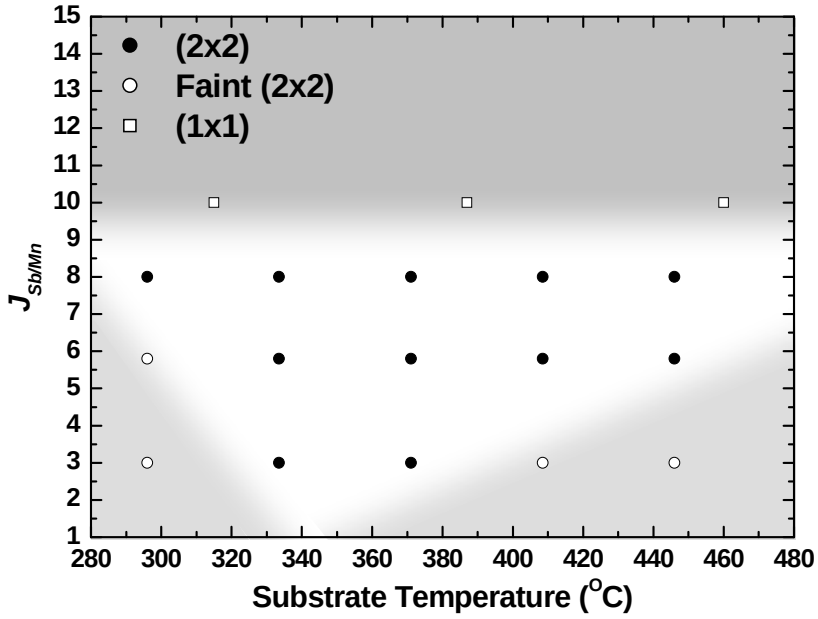

Figure 3.5: Surface symmetry observed by RHEED during growth of MnSb(0001) on GaAs(111)B under a variety of conditions. The colored background is a guide to the eye.

therefore MnSb[0001]||GaAs[111], MnSb[$2\bar{1}\bar{1}0$]||GaAs[$\bar{1}10$].

Figure 3.5 shows the surface reconstructions observed during growth of MnSb/GaAs(111)B. Two different RHEED patterns were observed. The main reconstruction over a large range of T-$J_{\mathrm{Sb/Mn}}$ phase space was a strong (2×2), with 2× both in the $<2\bar{1}\bar{1}0>$ (0°) and $<10\bar{1}0>$ (30°) MnSb(0001) surface directions. This RHEED pattern is shown in Figure 3.3. At low flux ratios and high/low temperatures, the (2×2) RHEED patterns became faint, and the streaks blurred, indicating a deterioration in the surface quality. At high flux ratios, a second RHEED pattern, (1×1) appears. This pattern has the same integer order spacing and symmetry as the (2×2), and so is also consistent with MnSb(0001) growth. Given the Sb rich conditions required to obtain this surface, it is likely that this is not a true reconstruction, but simply a highly disordered surface resulting in a suppression of the fractional order streaks.

The phase map in Figure 3.5 shows that in the range 300°C$<T<$450°C and $5<J_{\mathrm{Sb/Mn}}<10$, the surface symmetry is reasonably insensitive to these two parameters, giving a (2×2) RHEED pattern. The strongest RHEED features were observed at higher flux ratios ($J_{\mathrm{Sb/Mn}} \sim 8$) and temperatures around 400°C.

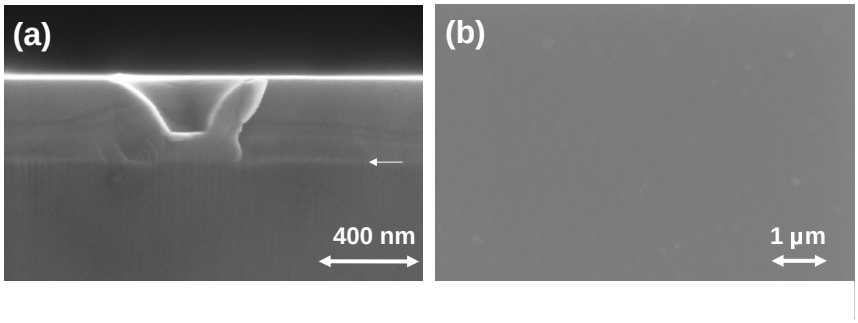

Figure 3.6: (a) Cross sectional SEM image of MnSb/GaAs(111)B. An arrow indicates the interface. (b) Plan view SEM image of MnSb over-layer.

3.2.3 Ex situ analysis of MnSb/GaAs(111)B

Scanning electron microscopy

After removing MnSb/GaAs(111)B samples from the growth chamber, they were studied by plan view and cross sectional SEM. In all cases, plan view SEM images showed a surface which was featureless on a sub micron scale. An example is shown in Figure 3.6b. Panel a shows the cleaved edge SEM image of a typical growth layer. The over-layer for all MnSb/GaAs(111)B samples demonstrated a flat interface parallel to the over-layer surface. The over-layer thickness was constant to within experimental error ($\pm$ 10 nm) across the entire cleaved edge, indicating uniform growth across the sample.

From the ratio of the growth thickness (determined from the cross sectional SEM) and the growth time, it is possible to determine the growth rate (GR) for samples grown under different conditions. The growth rate for III-V materials under typical growth conditions (group V overpressure) is group III limited. By analogy, the growth rate of MnSb under Sb rich conditions may reasonably be expected to be Mn dependent. By observing the growth rate under various conditions, more details on the optimal growth conditions are obtained.

Figure 3.7 shows the growth rate for MnSb/GaAs(111)B samples grown under a range of flux ratios ($1<J_{\mathrm{Sb/Mn}}<10$), Mn beam pressures (1×10^{-7} mbar$<P_{\mathrm{Mn}}<5\times10^{-7}$ mbar) and temperatures (300°C$<T<$470°C). Since a number of variables are changing simultaneously, the data were plotted as follows. In both panels, the vertical axis indicates GR/P_{Mn}. This is done in anticipation that the growth rate will be dependent

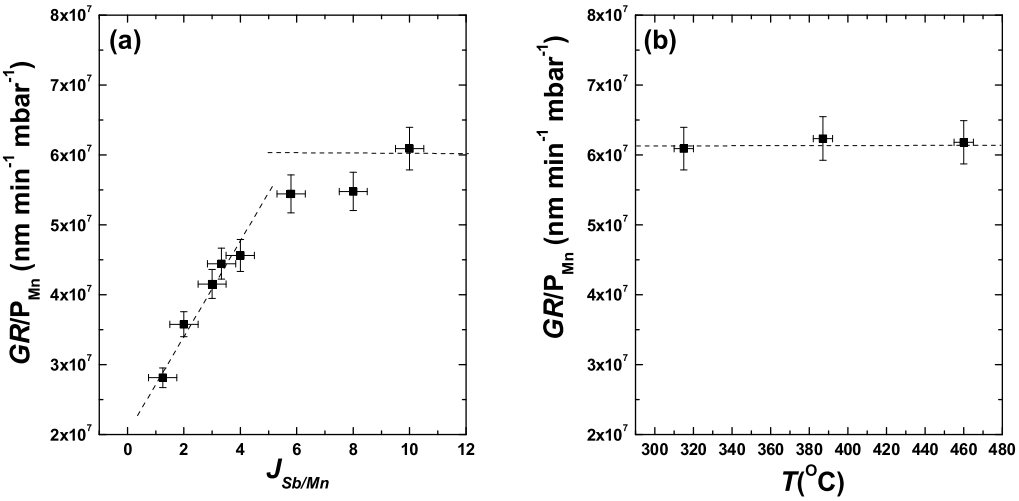

Figure 3.7: Dependence of GR/P_{Mn} on (a) $J_{\mathrm{Sb/Mn}}$ with T = 400°C and (b) T with $J_{\mathrm{Sb/Mn}}$ = 8.

upon the Mn flux, and that under optimal conditions GR/P_{Mn} should be a constant as described by Appendix A.

$$\frac{GR}{P_{\mathrm{Mn}}} = 10.9 \times 10^7 \frac{V_{\mathrm{MnSb}}}{\sqrt{T_{\mathrm{Mn}} M_{\mathrm{Mn}}}} [\mathrm{nm\ min^{-1} mbar^{-1}}] \tag{3.1}$$

Using the values M_{Mn} = 55 amu, T_{Mn} = 1133 K (Mn cell operating temperature), V_{MnSb} = 42.7 Å^3 and the appropriate ion gauge sensitivity factor, a value of GR/P_{Mn} = 2.7×10^7 nm min^{-1} mbar^{-1} is predicted.

Figure 3.7a shows the dependence of GR/P_{Mn} upon the BEP ratio $J_{\mathrm{Sb/Mn}}$ with a constant substrate temperature of 400°C. The plots indicate two distinct regimes. At low BEP ratios ($J_{\mathrm{Sb/Mn}}$<6), the growth rate increases linearly with flux ratio. The gradient in this region is ∼6×10^6 nm min^{-1} mbar^{-1}, and indicates that below $J_{\mathrm{Sb/Mn}}$ = 6 the growth is Sb limited. In the Sb poor regime, excess Mn will appear in the growth layer in some form, although at this point no assumptions are made regarding its location. At higher flux ratios ($J_{\mathrm{Sb/Mn}}$>6), the data points appear to reach a plateau, where the gradient approaches zero, and the growth becomes Mn limited as expected. In this regime, there is sufficient Sb for all the Mn arriving at the surface to react and form MnSb. From Figure 2.3 earlier in this thesis, the sublimation of metallic Sb from the surface at 400°C is considerably more rapid than that of Mn, and

so excess Sb on the surface can easily desorb into the vacuum, allowing the growth of stoichiometric material. In the Mn limited regime, $GR/P_{\mathrm{Mn}} \simeq 6\times10^{7}$ nm min^{-1} mbar^{-1}. While this is the same order of magnitude as the theoretical value of 2.7×10^{7} nm min^{-1} mbar^{-1}, there is a significant difference. This difference could arise from a number of sources, including assumptions for the growth rate (Equation 3.1), and ion gauge pressure calibrations which have been observed to vary by at least a factor of $\times2$ between different controllers. While ion gauge calibrations would not affect BEP ratios, individual BEPs would change and hence so would the calculated growth rate.

The transition from Sb poor to Sb rich growth at $J_{\mathrm{Sb/Mn}} \sim 6$ indicates the pressure ratio at which the arrival rates for Mn and Sb are approximately equal. $J_{\mathrm{Sb/Mn}}$ is expressed by nitrogen equivalent pressures P_{Sb} and P_{Mn}, and by incorporating the appropriate ion gauge sensitivity factors described in Section 2.3, the value of $J_{\mathrm{Sb/Mn}} \sim 6$ corresponds to a true pressure ratio of approximately 1:1 as expected.

Figure 3.7b shows the growth rates determined for samples grown across the range 300-470°C. These experiments were all carried out in the high flux ratio regime at $J_{\mathrm{Sb/Mn}} \sim 8$, with Mn BEP set at 1×10^{-7} mbar. The growth rate across this region is constant within experimental error, and indicates that the deposition and formation of MnSb is not strongly affected by the substrate temperature at these flux ratios. Closer to the transition region between Mn and Sb limited growth, the temperature dependence is likely to be stronger as a result of T dependent Sb desorption rates and effective changes in $J_{\mathrm{Sb/Mn}}$.

X-ray photoelectron spectroscopy

Epitaxial growth of MnSb/GaAs(111)B at flux ratios $J_{\mathrm{Sb/Mn}} < 6$ shows a growth rate dependence upon the Sb beam pressure (Figure 3.7a). Under these conditions, excess Mn is expected in the growth layer. Excess Mn may occur in a number of environments, including incorporation into the growth layer either as interstitial Mn, non-stoichiometric material ($\mathrm{Mn}_x\mathrm{Sb}$, $x > 1$) or as Mn cluster incorporation. Another possibility is that the Mn accumulates at the surface. In order to examine the stoichiometry near the growth region in the two different growth regimes, samples grown under Sb limited ($J_{\mathrm{Sb/Mn}} = 4$) and Mn limited ($J_{\mathrm{Sb/Mn}} = 8$) growth conditions were examined using XPS. XPS spectra showing the Sb 4d, Ga 3d and Mn 3p photoelectron peaks are

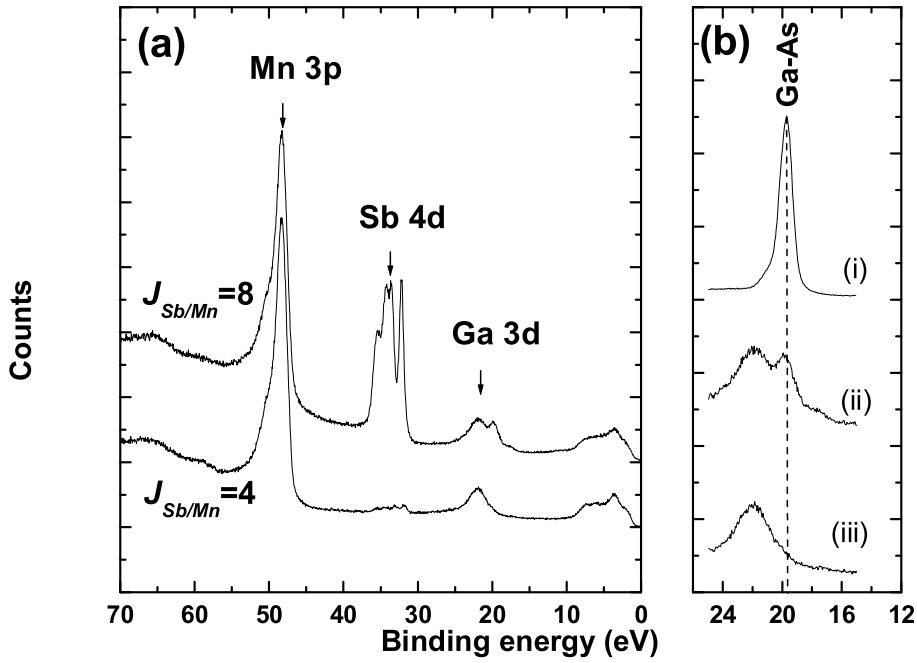

Figure 3.8: (a) XPS spectra for MnSb/GaAs(111)B samples grown at $J_{\mathrm{Sb/Mn}} = 8$ and $J_{\mathrm{Sb/Mn}} = 4$ and (b) Ga 3d peak for (i) GaAs (ii) MnSb/GaAs(111)B, $J_{\mathrm{Sb/Mn}} = 8$ and (iii) MnSb/GaAs(111)B, $J_{\mathrm{Sb/Mn}} = 4$.

shown in Figure 3.8a. The high flux ratio sample shows large Mn and Sb peaks, while the low flux ratio sample shows a surface predominately of Mn, with a very small Sb peak. The spectrum for $J_{\mathrm{Sb/Mn}} = 8$ is closer to that expected for stoichiometric MnSb, while the $J_{\mathrm{Sb/Mn}} = 4$ indicates a highly Mn enriched surface region. Since the probing depth of XPS is of the order of 30-40 Å, these measurements do not indicate the stoichiometry of the entire over-layer, but that of the surface region. The presence of this thick Mn layer on the surface is surprising, since the RHEED spacings during growth of the low flux ratio samples were consistent with MnSb. A Mn layer sufficiently thick to dominate the XPS signal should certainly hinder RHEED observation. One possibility is that the surface Mn is in the form of droplets on the surface during growth, still allowing RHEED on the MnSb surface, but large enough that transmission diffraction is not observed. These droplets may then form a thick capping layer after cooling and oxidation, although this has yet to be tested with a quenching experiment. This Mn cap only occurs for samples in the Sb limited growth regime, and hence the Mn limited growth

regime ($J_{\mathrm{Sb/Mn}}$>6) is identified as more suitable for growth of MnSb/GaAs(111)B.

Both samples are in excess of 200 nm thick, and as such the presence of the Ga 3d peak is unexpected. Figure 3.8b shows the Ga 3d peak for:(i) GaAs, (ii) MnSb, $J_{\mathrm{Sb/Mn}} = 8$ and (iii) MnSb, $J_{\mathrm{Sb/Mn}} = 4$. The Ga peaks for the MnSb samples are predominantly high binding energy oxides, although the sample grown at $J_{\mathrm{Sb/Mn}} = 8$ also shows a peak at similar energy to that of the Ga-As peak in GaAs. In the absence of As, this is attributed to Ga-Sb bonding in the Sb rich growth regime. Surface segregated Ga has been previously reported for MnSb/GaAs growth in the literature [64].

Standard growth conditions

Considering the results from the previous sections, the following growth parameters have been used for all remaining growth of MnSb on GaAs in this thesis.

- $T_{\mathrm{Mn}} = 860$°C
- $P_{\mathrm{Mn}} = 1\times10^{-7}$ mbar
- $T_{\mathrm{Sb}} = 373$°C
- $P_{\mathrm{Sb}} = 8\times10^{-7}$ mbar
- $J_{\mathrm{Sb/Mn}} = 8$
- $T = 400$°C

These conditions ensure growth of the MnSb(001) surface with a (2×2) RHEED pattern in the Mn limited growth regime. Growth rates under these conditions are 6 ± 0.5 nm min^{-1}. In order to fully optimise these growth conditions, detailed studies on the magnetic and crystallographic properties are required.

3.3 Characterisation of MnSb/GaAs(111)B

MnSb(0001) has been successfully grown on GaAs(111)B substrates, and a set of standard conditions chosen which are used for all following growth on GaAs. In this section, the MnSb over-layers produced under these growth conditions are studied in more detail.

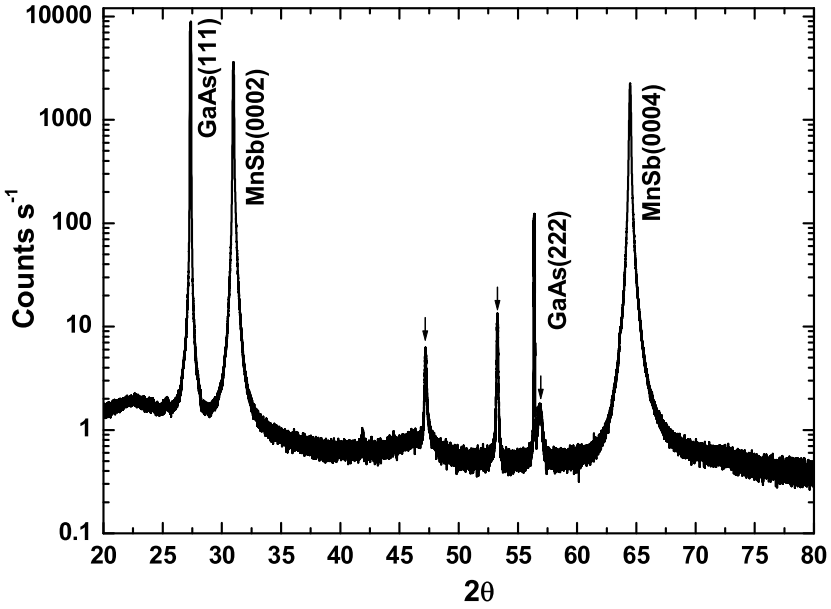

Figure 3.9: XRD spectrum for MnSb/GaAs(111)B grown under standard conditions. Unidentified peaks are indicated by arrows.

3.3.1 X-ray diffraction of MnSb/GaAs(111)B

In order to confirm the growth orientation of MnSb/GaAs(111)B, a sample grown under standard conditions was studied by X-ray diffraction (XRD). A PANalytical X-pert Pro MRD was used to obtain a 2θ-ω scan of a 200 Å thick MnSb/GaAs(111)B sample. The spectrum obtained is shown in Figure 3.9, the main peaks for which are labelled. Peak assignments may be checked using the Bragg condition for diffraction shown below, in which n is an integer, λ the X-ray wavelength (1.54 Å for Cu Kα used here), d the plane spacing ($\sqrt{3}a/3$ for GaAs(111), $c/2$ for MnSb(0001)) and θ the diffraction angle [87].

$$n\lambda = 2d\sin\theta \tag{3.2}$$

Experimental peak positions and those predicted for MnSb and GaAs planes are shown in Table 3.1. The agreement between the experimental and predicted peak positions are very good, and confirm the growth orientation as MnSb(0001)/GaAs(111)B. In addition to the expected peaks, additional peaks are observed at 47.19°, 53.27° and 56.86°. These peaks are small compared to the substrate and over-layer diffraction

Peak	Position	d	n	Predicted position
GaAs(111)	27.35°	3.26 Å	1	27.34°
GaAs(222)	56.38°	3.26 Å	2	56.43°
MnSb(0002)	30.90°	5.789 Å	2	30.88°
MnSb(0004)	64.41°	5.789 Å	4	64.34°
?	47.19°			
?	53.27°			
?	56.86°			

Table 3.1: Peak data for the XRD scan of MnSb/GaAs(111)B. All expected peaks for MnSb(0001) and GaAs(111) oriented crystals are observed, in addition to three unassigned peaks

peaks and may be a result of intermixing phases at the interface such as MnGa, MnAs or GaSb. Alternatively, they could be an effect of relaxation or reconstruction at the surface. At present the identity of these peaks is unknown. The FWHM of both the GaAs(111) and MnSb(0002) peaks are $\sim 0.12^\circ$ as a result of experimental broadening from the detector used. As such, these values do not represent the crystalline quality of the sample.

3.3.2 Magnetic measurements of MnSb/GaAs(111)B

Bulk MnSb with the NiAs structure is ferromagnetic with a magnetic moment of 3.5 μ_{B}/Mn atom [50]. In order to characterise this aspect of the MnSb films, a number of magnetic measurements were carried out. Both a superconducting quantum interference device (SQUID) and vibrating sample magnetometer (VSM) were used to measure the magnetisation (M) of a MnSb/GaAs(111)B sample at various temperatures (2 K$<T<$400 K) and magnetic fields (-1000 kOe$<H<$1000 kOe). Both devices operate by moving the sample in a series of superconducting coils while in a magnetic field. The inducted current measured in the coils is proportional to the magnetisation of the sample due to the magnetic field and these data are plotted as a function of H or T to obtain $M-H$ and $M-T$ graphs respectively. The two devices differ in the method of detection, with the SQUID moving the sample slowly through three coils, while the VSM vibrates the sample through a pair of opposite coils. The VSM collects data faster, and is better equipped to measure M-H hysteresis curves. The SQUID is more sensitive and the device at Warwick University has the facility for $M-T$ measurements in the range 2-400 K.

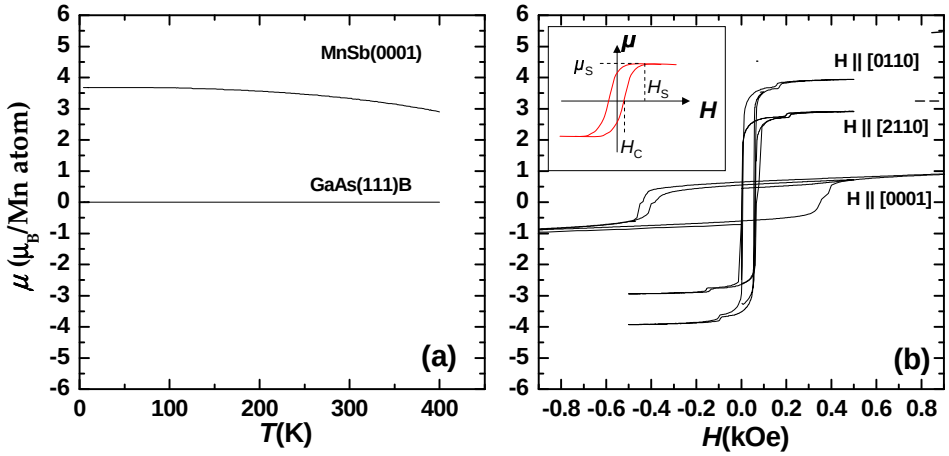

Figure 3.10: (a) M-T measurements carried out using the SQUID under a magnetic field of 200 Oe for MnSb/GaAs(111)B and the GaAs(111)B substrate.(b) M-H measurements using the VSM at 10 K for MnSb/GaAs(111)B with the magnetic field aligned in the over-layer plane along the [01$\bar{1}$0] and [2$\bar{1}\bar{1}$0] and out of plane along the [0001]. The inset shows the saturation field (H_{S}) saturation magnetisation (μ_{S}) and coercive field (H_{C}).

The temperature dependence of the magnetisation of a MnSb/GaAs(111)B sample grown under standard conditions was measured using the SQUID between 2-400 K under a magnetic field of 200 Oe (0.02 T). The effective magnetic moment per Mn atom (μ) was calculated using the equation

$$\mu = \frac{M}{\mu_{\mathrm{B}} N_{\mathrm{Mn}}} \tag{3.3}$$

Here, N_{Mn}, the number of Mn atoms in the sample was calculated from the over-layer volume (obtained from cross sectional SEM thickness measurements and macroscopic area measurements) and assuming the ideal NiAs structure for MnSb. The Bohr magneton μ_{B} has a value of 9.274 $\times$ 10^{-24} J T^{-1}. The temperature dependence of μ is plotted in Figure 3.10a. The MnSb/GaAs(111)B sample shows a strong ferromagnetic signal at 2 K which then decreases slowly with temperature. This behaviour is that of increasing thermal disorder of a ferromagnetic system, and the shape of the graph indicates a Curie temperature $T_{\mathrm{C}} > 400$ K [88]. The magnetic moment measured at 2 K is 3.6 μ_{B}/Mn atom, in good agreement with the literature value of 3.5 μ_{B}/Mn atom for MnSb [50]. The $M-T$ characteristics of a GaAs(111)B substrate are also shown

in Figure 3.10a. The substrate shows a very weak diamagnetic (negative) signal. The ferromagnetic signal from the MnSb/GaAs(111)B sample is therefore from the MnSb over-layer.

$M - H$ hysteresis loops were measured for the MnSb(0001) samples using the VSM with the magnetic field aligned along three perpendicular crystallographic directions, two in the plane of the sample: $[2\bar{1}\bar{1}0]$ and $[01\bar{1}0]$, and one out of plane, [0001]. The hysteresis loops for these measurements are shown in Figure 3.10b. In order to avoid superconducting signals from the metallic eutectic on the bottom of the substrate (a remnant from attaching the wafer to sample plates in the growth chamber), measurements were all carried out at 10 K, above the superconducting threshold temperatures of all elements. The hysteresis loops were all compensated for the paramagnetic sample holders and the diamagnetic substrate in order to get the signal from the MnSb over-layer alone. The following measurements are taken from the hysteresis loops: the saturation field (H_{S}), the field at which the magnetisation saturates at a value of (μ_{S}), and the coercive field (H_{C}), the field at which the magnetisation changes sign. The values taken from the hysteresis loops in Figure 3.10b are shown in Table 3.2.

Field	H_{S}	μ_{S}	H_{C}
$[2\bar{1}\bar{1}0]$	0.2 kOe	2.9 μ_{B}	60 Oe
$[01\bar{1}0]$	0.2 kOe	3.9 μ_{B}	60 Oe
[0001]	18 kOe	2 μ_{B}	300 Oe

Table 3.2: Saturation field (H_{S}), saturation magnetisation (μ_{S}) and coercive field (H_{C}) for MnSb/GaAs(111)B hysteresis loops shown in Figure 3.10b.

The easy axis of the magnetisation is clearly in the plane of the sample, with the sample reaching saturation with in-plane fields of only 0.2 kOe. When the magnetic field was out of plane, 18 kOe was required, although this saturation is not visible in Figure 3.10b. Coercive fields in the range 40-100 Oe have been reported by Liu *et al.* for in-plane hysteresis of MnSb/GaAs(111)B [70], agreeing well with the value of 60 Oe observed for the in-plane measurements on these MnSb samples. Liu *et. al.* also observed that high fields are required for saturation with an out of plane magnetic field, quoting values $>$10 kOe, consistent with the 18 kOe measured in the current work. For all field directions, hysteresis loops are observed, although the saturation magnetisation of each direction varies considerably. Since the saturation magnetisation is dependent

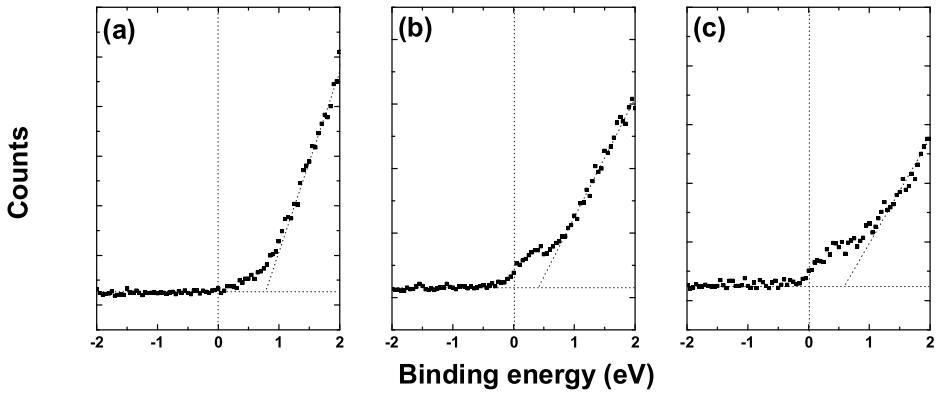

Figure 3.11: XPS valence band spectra for (a) GaAs (semiconducting), (b) Mn (metallic) and (c) MnSb (metallic).

upon the number of magnetic atoms in the sample, this should be independent of the orientation. The VSM is calibrated with a point Ni sample, and as such variations in measured magnetisations are expected for highly anisotropic samples such as these thin films, in particular between in plane and out of plane field directions. The variation in μ_{S} between the perpendicular in plane field directions may also be affected by the point calibration, although the large size of the effect is surprising. A second possibility is that the sample may not be fully saturating in all directions at magnetic fields <2 T. In either case, this strange behaviour merits further study.

The MnSb films grown on GaAs(111)B by the standard MBE conditions are ferromagnetic, with a Curie temperature in excess of 400 K and magnetic moment of 3.6 μ_{B}/Mn atom in good agreement with the literature. Further work is required to resolve the outstanding issues regarding the rather puzzling directional dependence of the saturation magnetisation of the films.

3.3.3 Valence band of MnSb/GaAs(111)B

MnSb is reported to be a metallic compound, and as such a further test of MnSb/GaAs(111)B samples is to ensure that they are metallic. This was studied by observing the valence band maximum (VBM) of a number of samples using XPS obtained at the NCESS facility (Daresbury Laboratory, UK). Figure 3.11 shows XPS spectra of the VBM region for three materials. Using the linear method outlined by Chambers *et*

al. [89] the VBM position of a semiconductor may be determined by the intersection of two straight lines. The first is fitted to the linear drop-off of the VBM, and the second fitted to the background counts. These two lines are shown in Figure 3.11. Panel a shows the VBM for GaAs(001). The VBM is determined to be 0.8 eV below the Fermi level (0 eV), matching well with the predicted values between the charge neutrality level (0.55 eV) and the experimental values up to 0.9 eV obtained for samples cleaned at different temperatures [90]. There is a tail on the VBM between 0.8 eV and 0 eV, due to experimental broadening. This sample shows the features expected of a semiconductor. Panel b shows the same region for a thick (>200 nm) layer of Mn. The spectrum for Mn shows a small density of states up to the Fermi level, consistent with a metallic material. Again, a small tail between -0.5 eV to 0 eV is due to experimental broadening. It is clearly possible to distinguish between metallic and semiconducting materials. Figure 3.11c shows the valence band region for a thin ($\sim$ 45 Å) MnSb film grown under the standard growth conditions. The MnSb film shows a non-zero density of states right up to the Fermi level, proving that the MnSb thin film is metallic. Thick layers ($\sim$200 nm) of MnSb also show this metallic density of states, although as a result of the suspected build up of Mn at the surface and the high surface specificity of XPS, the metallic features in the thick layers may be due to either the MnSb or Mn at the surface. The thin layer data is sufficient to demonstrate that the MnSb grown is metallic.

3.3.4 Growth mode of MnSb/GaAs(111)B

Heteroepitaxial growth can proceed by a variety of growth modes, described in Section 1.4.2. Understanding the initial growth mode for MnSb on GaAs substrates will be crucial for future studies growing high quality interfaces, in particular for devices requiring thin MnSb layers. The growth mode will depend upon the growth conditions, although discussion here is limited to the growth mode under the standard conditions described earlier.

RHEED

MnSb/GaAs(111)B samples grown under the standard conditions demonstrate a (2×2) RHEED pattern with integer order spacing characteristic of MnSb. Figure 3.12a shows the RHEED spacings over the growth run, measured from camera images. Before

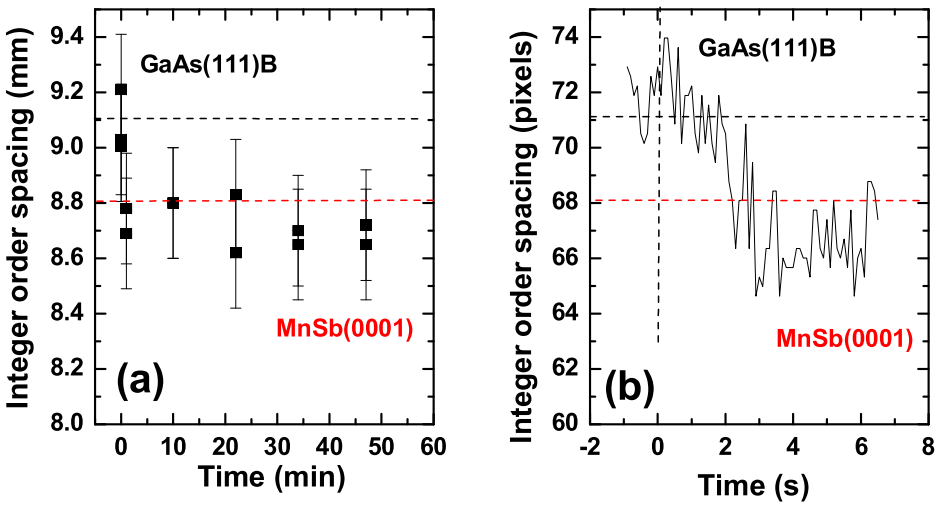

Figure 3.12: RHEED integer order streak spacing measured from (a) camera images throughout a 1 hour growth run and (b) video capture of the RHEED screen during the initial growth.

growth, the integer order RHEED spacings are 9.1 $\pm$ 0.2 mm, corresponding to the GaAs(111)B substrate ($a' = 3.99$ Å). Within one minute of growth, the RHEED spacing reduces by ~6%, agreeing well with the growth of the larger MnSb(0001) lattice ($a' =$ 4.129 Å). Following this initial change, the RHEED pattern shows no obvious changes throughout the remaining growth. In order to examine the RHEED transition in more detail, higher time resolution is required. To achieve this, a digital camera operating on video mode was used to record the RHEED screen. The maximum resolution of the video was only 640×480 pixels (c.f. 2608×1952 in the mode used for all other RHEED measurements). Furthermore due to the short exposure necessary for video mode, it was only possible to detect the integer order streaks, but not fractional orders. Images from the video were extracted at 0.1 s intervals and the integer order streak spacing was measured as a function of time using the Matlab code RHEEDprofile.m (Appendix B). Peak positions were identified manually within the program, and as such were allowed non-integer pixel positions. The results of these measurements are shown in Figure 3.12b. The high noise in Figure 3.12b is a combination of the low resolution of the video, the small change in RHEED spacing and the low exposure time. Despite the relatively crude measurement, Figure 3.12b shows that the RHEED spacing reduces by ~6 % within the first 3 s, indicating the formation of fully relaxed MnSb in this time

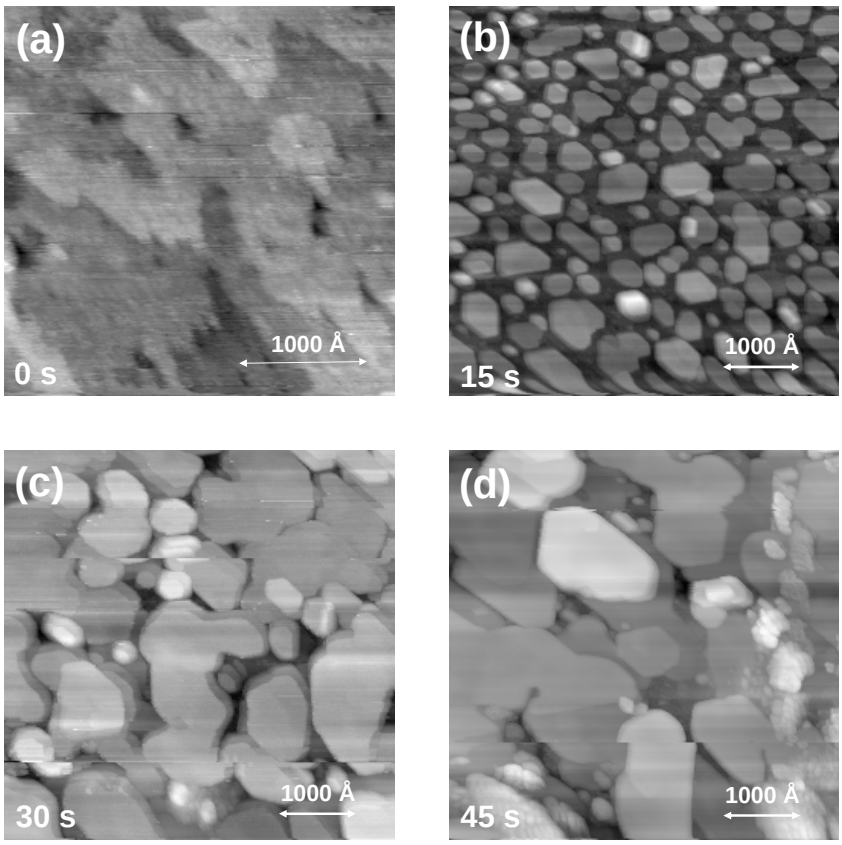

Figure 3.13: STM images for thin MnSb/GaAs(111)B layers. Nominal layer thicknesses are (a) 0 Å, (b) 15 Å, (c) 30 Å, (d) 45 Å.

frame. The growth rate of MnSb under the standard conditions is 6 $\pm$ 0.5 nm min^{-1}, and so in 3 s, only a few Å of material have been grown. Akinaga *et al.* observed RHEED relaxation of MnSb/GaAs(111)B over a growth thickness of 20-30 Å [91], and so the relaxation observed in the current work is surprisingly rapid .

Scanning tunnelling microscopy

STM was used to image the surface after interrupting growth at various points during the first minute. The experiments were carried out as follows. The substrate was cleaned in situ as described in Section 3.2.1, and imaged using the STM. The sample was moved back to the growth chamber, heated to 400 °C and exposed to Mn and Sb fluxes for $t_{\mathrm{Mn+Sb}} = 10$ s. Since the growth conditions are rather Sb rich, the sample was exposed to Mn for $t_{\mathrm{Mn}} \sim 5$ s after each interruption to obtain a strong (2×2) surface reconstruction before imaging in the STM. This procedure was used to obtain a

Panel	$t_{\mathrm{Mn+Sb}}$ (s)	t_{Mn} (s)	$c_{\%}$	$h_{\max}$ (Å)	h_{av} (Å)	L (Å)	$L_{\mathrm{predicted}}$ (Å)
(a)	0	0	0	3 ± 1	3 ± 1	0	0
(b)	10 ± 1	5 ± 1	70 ± 5	48 ± 5	20 ± 5	14 ± 4	15 ± 2
(c)	20 ± 2	10 ± 1	95 ± 2	86 ± 5	45 ± 10	42 ± 10	30 ± 4
(d)	30 ± 3	15 ± 1	97 ± 2	114 ± 5	60 ± 10	58 ± 11	45 ± 6

Table 3.3: Measurements from Figure 3.13. $t_{\mathrm{Mn+Sb}}$ is the co-deposition time and t_{Mn} the time annealed under Mn to stabilise the (2×2) reconstruction. $c_{\%}$ refers to the over-layer coverage, $h_{\max}$ and h_{av} the maximum and average island heights. L is the equivalent layer thickness and $L_{\mathrm{predicted}}$ the value calculated from the total growth time t and the growth rate.

consistent surface for STM imaging. Total growth time is defined as $t = t_{\mathrm{Mn+Sb}} + t_{\mathrm{Mn}}$. This total growth time allows that during the Mn annealing time, new growth material may be forming from the Mn flux and excess Sb on the surface. Although at 400 °C the desorption of Sb from the surface will be rapid, the large Sb over-pressure during growth and small time interval between growth and Mn annealing makes it probable that some Sb will still be on the surface. The growth process was repeated, and surfaces studied by STM after t = 15, 30 and 45 s of growth. The STM images obtained are shown in Figure 3.13.

Figure 3.13b shows the surface after only 15 s of growth. The surface exhibits large, flat topped 3D islands of ∼500 nm in diameter, and an average of 20 Å in height covering approximately 70% of the surface. The islands show clear preferential edge directions at 60° rotations, indicating hexagonal symmetry. From the STM images it was possible to determine the percentage island coverage ($c_{\%}$), maximum and average island height ($h_{\max}$,h_{av}). These are shown in Table 3.3. The equivalent layer thickness L is defined as the over-layer thickness which would be formed if all the material in the 3D islands had formed by layer by layer growth (i.e. $c_{\%}$=100). This is calculated from the island coverage and the average island height h_{av} as

$$L = \frac{c_{\%} \times h_{\mathrm{av}}}{100} \tag{3.4}$$

A predicted equivalent layer thickness $L_{\mathrm{predicted}}$ was obtained from the growth rate and the growth time t. After growth for 15 s, the equivalent layer thickness is 14 ± 5 Å, in very good agreement with the predicted value $L_{\mathrm{predicted}}$ = 15 Å. As more material was grown, the 3D islands increase to a coverage of ∼95% after 30 s (Figure 3.13c), and 97% after 45 s (Figure 3.13d). As expected during growth the average height of the islands increases, but even after 45 s, the islands still do not fully cover the substrate.

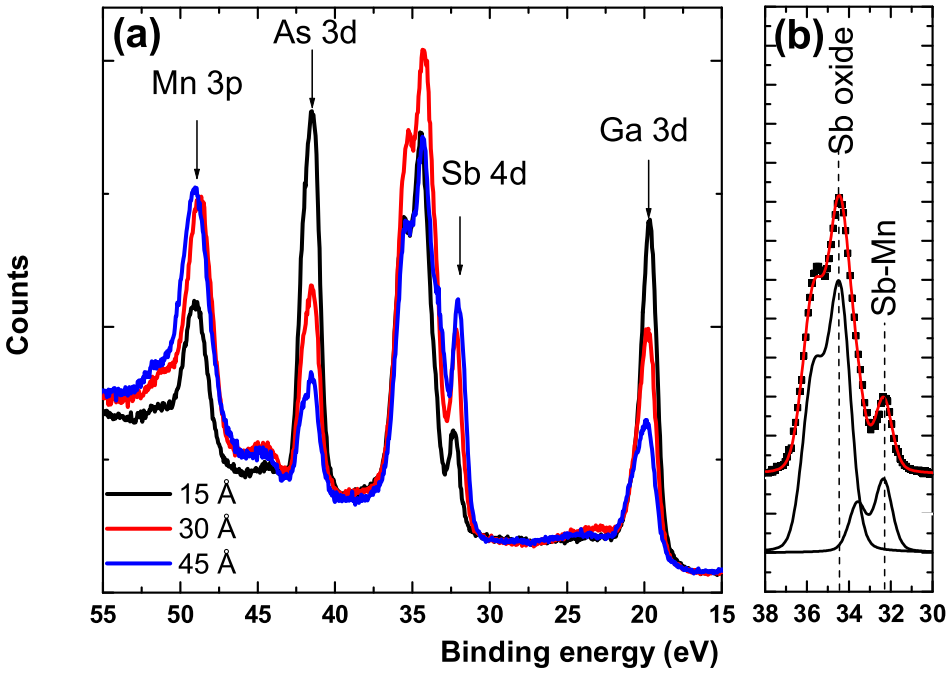

Figure 3.14: (a) XPS spectra for nominal 15 Å, 30 Å and 45 Å MnSb films grown on GaAs(111)B under standard conditions. (b) Sb 4d peak and approximate peak fitting.

The equivalent layer thickness for panels c and d are consistently greater than those predicted from the growth rate, which many be due to the difficulty in determining h_{av} at high coverage.

X-ray photoelectron spectroscopy

In order to ensure that the islands observed in STM are MnSb, XPS was carried out on a series of thin films at the NCESS facility (Daresbury, UK). Samples of nominal thickness 15 Å, 30 Å and 45 Å were grown, and then removed from the growth system, resulting in unavoidable contamination of the surface by atmospheric gases. Earlier, in Figure 3.2a, XPS spectra of the GaAs(111)B substrate were presented. Figure 3.14a shows the same region for the three thin films. Four peaks are clearly visible in all three spectra, corresponding to the Ga and As 3d, Sb 4d and Mn 3p core levels. The most complex peak is the Sb 4d. This peak has been fitted in Figure 3.14b by two peaks, each consisting of a doublet, with spin orbit splitting of 1.25 eV [92]. The low binding energy peak corresponds to Sb-Mn bonding at 32.3 eV, fitted using a peak with FWHM 0.9

eV and L:G 29 % as described in Section 1.4.4. The second peak has been broadened to FWHM 1.2 eV to represent a number of oxide and surface peaks which are hard to fit individually. The relevant peak in the Sb 4d for study of the growth layer is the low binding energy Sb-Mn, rather than the oxide layer.

The presence of a thick contamination layer combined with a thin growth layer makes useful quantitative analysis extremely difficult. Qualitatively, information can be obtained from the trends of the peak heights. As the layer thickness increases from 15 Å (black line) to 45 Å (blue line), the four peaks follow two types of behaviour. The As 3d and Ga 3d peak heights decrease at a similar rate with increasing over-layer thickness, while the Mn 3p and Sb 4d peaks increase. This is clear evidence that the Mn and Sb are over growing the GaAs substrate, rather than forming an intermixing layer. Since the Mn and Sb, and the Ga and As peaks follow almost identical trends, there is some degree of confidence that the pairs of atoms have similar depth profiles, indicating that two phases exist, MnSb and GaAs. This result gives confidence in the identity of the islands observed by STM in Figure 3.13 as MnSb.

Growth mode

The STM images show that under the standard conditions, the growth of MnSb /GaAs(0001) begins by the nucleation and then coalescence of MnSb 3D islands with flat tops. The RHEED patterns observed within the first few seconds correspond to RHEED from the relaxed tops of the 3D islands. Growth then proceeds by the almost complete coalescence of the 3D islands within the first minute, with no further observed changes to the RHEED spacing. STM of thicker layers indicate that once the islands have coalesced, the growth mode is layer by layer, forming large flat terraces. These surfaces are considered in more detail in Chapter 4. Similar nucleation and coalescence of MnSb 3D islands on GaAs have been observed by Tatsuoka *et al.* [71] using TEM. Growth by the nucleation and coalescence of 3D islands poses a considerable obstacle to formation of high quality interfaces since it is probable that buried gaps and crevices will form in the interface region before the islands coalesce higher up. It is likely that the size and distribution of these islands will be dependent upon temperature and growth rate as a result of the changing mobility and average migration length of the adatoms prior to incorporation. It is possible that further study can lead to growth conditions

which may reduce or even prevent 3D island nucleation at the interface, and improve the interface quality, although this is not considered further in this thesis.

3.4 MnSb/GaAs(001)

MnSb films which are metallic and ferromagnetic have been successfully grown by MBE on GaAs(111)B substrates with the growth orientation MnSb[0001]||GaAs[111], MnSb[$2\bar{1}\bar{1}0$]||GaAs[$\bar{1}10$]. The advantage of the GaAs(111)B substrate is the symmetry match with the hexagonal MnSb(0001) plane. In contrast, GaAs(001) has little similarity, with a cubic surface mesh, and lattice mismatch $\geq$3.2% in all directions. It is therefore interesting to observe how MnSb grows on this surface. This section presents preliminary results on this system.

GaAs(001) samples were prepared by IBA in the same manner as the GaAs(111)B in the previous section. The RHEED pattern observed after cleaning corresponds to the Ga rich (4×6) reconstruction [93, 94]. MnSb films were grown on the cleaned GaAs(001) substrate using the standard conditions described in Section 3.2.3. RHEED patterns after 1 hr of growth showed strong integer and fractional order streaks. Figure 3.15 shows RHEED patterns and profiles for the GaAs substrate (4×6), and the MnSb over-layer. The integer order spacing observed with the electron beam along 0° was 15.6 mm, and 4.6 mm along 90°. These spacings, along with observations at other azimuths confirm the growth plane as MnSb($1\bar{1}01$), consistent with other growth studies on MnSb [60, 95]. Ideal RHEED screen spacings calculated by the method described in section 2.4 are 15.1 mm and 4.56 mm. Figure 3.16 shows the orientations of the GaAs substrate and the MnSb over-layer. The epitaxial orientation of the MnSb($1\bar{1}01$)/GaAs(001) is MnSb[$1\bar{1}02$]||GaAs[110] and MnSb[$11\bar{2}0$]||GaAs[$1\bar{1}0$]. There are indications that a second growth orientation may exist, rotated by 17° such that MnSb[0101]||GaAs[110]. At this time, this is unconfirmed, but should be of great interest for future work. The reconstruction observed on the MnSb($1\bar{1}01$) surface is discussed in the Chapter 4, in addition to the surface structure.

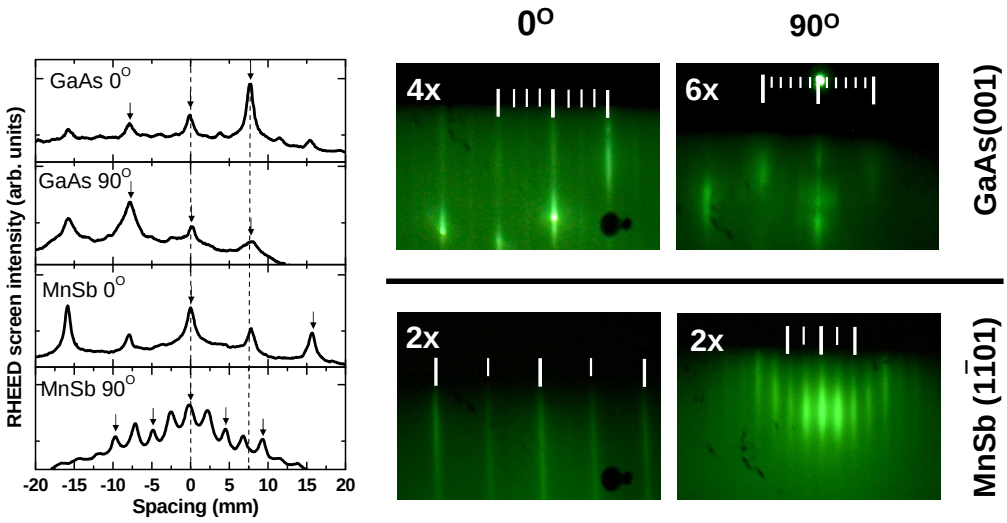

Figure 3.15: RHEED profiles and images for the GaAs(001) (4×6) substrate and MnSb(1$\bar{1}$01) (1×2) over-layer. RHEED images are shown with the electron beam along two directions, 0° and 90° shown in Figure 3.16. Integer order peaks in the RHEED profiles are indicated by arrows. Integer (fractional) order streaks in the RHEED images are indicated by long (short) lines.

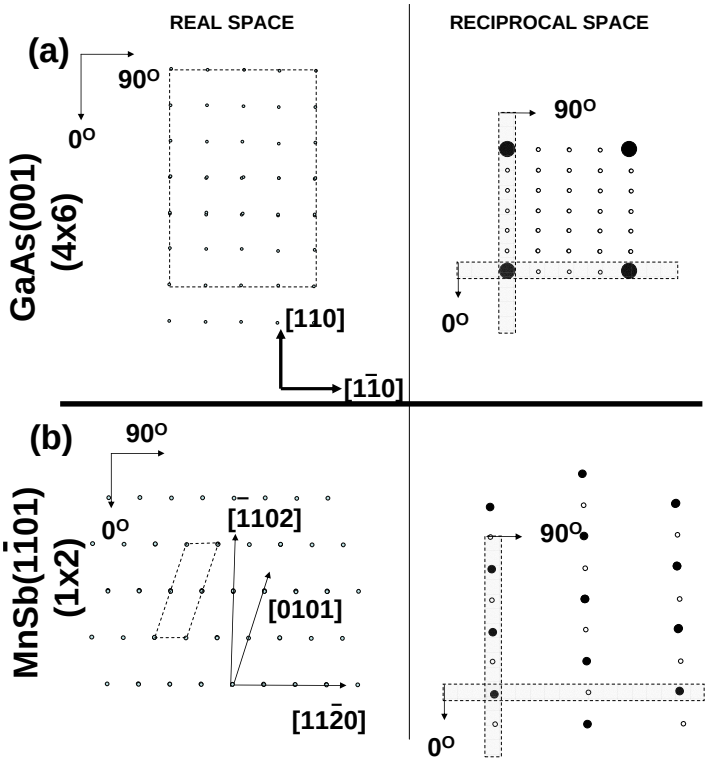

Figure 3.16: Epitaxial orientations of MnSb(1$\bar{1}$01) grown on GaAs(001). Panels indicate the relative real space (left) and reciprocal space (right) orientations of (a) the GaAs(001) and (b) MnSb(1$\bar{1}$01). The shaded regions in the reciprocal space panels indicate the recording plane of the RHEED when the electron beam is in the direction indicated by the attached arrow. The solid (empty) circles indicate integer (fractional) order diffraction features. Directions are consistent across all the panels.

3.5 Summary

In this chapter MnSb with the expected magnetic characteristics has been epitaxially grown on GaAs substrates. The T-$J_{\mathrm{Sb/Mn}}$ phase space for MnSb/GaAs(111)B was investigated by observation of RHEED patterns during growth. The RHEED in most cases showed strong integer order streaks, and in a wide range of phase space, a strong (2×2) pattern was observed. The growth rate of samples under different conditions was calculated, and the trends used to identify two different growth regimes. At flux ratios below $J_{\mathrm{Sb/Mn}} = 6$, the growth rate was dependent principally on the Sb BEP, and hence is termed the Sb limited growth regime. Samples grown in this region are found by XPS to be Mn rich at the surface after removal from the UHV chamber, supporting the observation that there is insufficient Sb to combine with all the Mn, leading to an accumulation of Mn at the surface. For higher flux ratios ($J_{\mathrm{Sb/Mn}}>6$), the growth rate becomes dependent only upon the Mn flux, and hence growth is Mn limited. Samples in this regime show near stoichiometric Mn:Sb ratios at the surface. Growth in the Sb rich regime is therefore preferable. On the basis of this work, standard growth conditions were chosen. Layers grown under these standard conditions are observed to be ferromagnetic and metallic, with growth orientations MnSb[0001]||GaAs[111], MnSb[$2\bar{1}\bar{1}0$]||GaAs[$\bar{1}10$] on GaAs(111)B and MnSb[$1\bar{1}02$]||GaAs[110] and MnSb[$11\bar{2}0$]||GaAs[$1\bar{1}0$] on GaAs(001). Both surfaces display surface reconstructions which are discussed in more detail in the following chapter.

Chapter 4

Surface structures of MnSb

4.1 Introduction

For the purpose of the fabrication of spintronic devices, epitaxial combinations of ferromagnetic and semiconducting materials are of great interest. In particular, the quality of the interface between the materials is likely to strongly influence the efficiency of spin injection into the semiconductor, with low quality interfaces more likely to reduce spin polarisation [96, 97]. For some proposed spintronic device structures, buried 2D layers of the ferromagnetic materials will be required, requiring two heteroepitaxial interfaces to be understood and optimised. The most commonly studied interface is the normal interface between a ferromagnet over-layer and semiconductor substrate. This is initially the easier surface to study, as semiconductor substrates are readily available and well characterised. A brief study of the growth mode under the standard growth conditions for the MnSb/GaAs(111)B interface was presented in the previous chapter, and identifies the 3D island nucleation growth mode as a potential problem for formation of high quality interfaces. The inverse interface, with a semiconductor over-layer grown on a ferromagnet is more challenging to study since the MnSb surfaces are less well understood. The structures and reconstructions of the MnSb surfaces are likely to be highly important with regard to the interfacial quality and growth modes of inverse interfaces, just as semiconductor surfaces and reconstructions are important for normal interface formation [57]. Despite this relevance, relatively little published work exists focussing on the surface science aspects of MnSb (or MnAs).

This chapter presents a study of the basic crystallography of two MnSb surfaces. The first section of this chapter discusses the MnSb(0001) surface obtained via growth on GaAs(111)B. The expected surface structure is discussed in some detail, and compared to the images obtained from STM. Surface reconstructions of the MnSb(0001) surface

are then investigated as a function of temperature and individual elemental fluxes. The second section considers the rather more complex MnSb($1\bar{1}01$) surface. Again, STM images are shown and a number of surface reconstructions discussed. In the final section of this chapter, the surface atomic structures are discussed, and suitable models for the MnSb(0001) (2×2) and td(1×4) reconstructions considered.

4.2 MnSb(0001)

4.2.1 MnSb(0001) surface morphology

In order to understand how MnSb is likely to bond to an over-layer, it is invaluable to consider the various possible MnSb surface terminations, and identify those which are most stable. Figure 4.1 shows the structure of a MnSb(0001) oriented crystal , projected onto the (1100) plane. Assuming that the surface is bulk terminated, and ignoring surface reconstruction for now, it is apparent that there are four possible terminations for the c plane (0001) surface. These are shown on the right of Figure 4.1, along with the plan view of the surface unit mesh for each. Dangling bonds for a bulk terminated crystal are indicated by short lines and the unreconstructed (1×1) surface mesh shown by dotted lines. The surface may be terminated by either Mn or Sb, each with two different orientations rotated by 60°. From simple bond counting arguments, there is no preferred surface, with each surface having three dangling bonds per unit cell. Using Figure 4.1 a MnSb mono-layer is defined as the distance between two consecutive Mn (or Sb) layers (e.g. Mn1 to Mn2). A MnSb bi-layer is therefore the distance between the same Mn (or Sb) layer (e.g. Mn1 to Mn1). For the MnSb(0001) surface, mono-layers all have a distance $c/2$ = 2.89 Å, and bi-layers c = 5.789 Å irrespective of the terminations.

4.2.2 Scanning tunnelling microscopy imaging of MnSb(0001) surfaces

In the previous chapter, epitaxial growth of thick (>200 nm) fully relaxed MnSb(0001) layers on GaAs(111)B was achieved. High quality RHEED images were consistently obtained from the surfaces, indicating atomically flat sections of the surface, while SEM showed a featureless surface at the highest magnifications indicating a smooth morphology at the 10-1000 nm scales. In order to investigate the surface morphology in

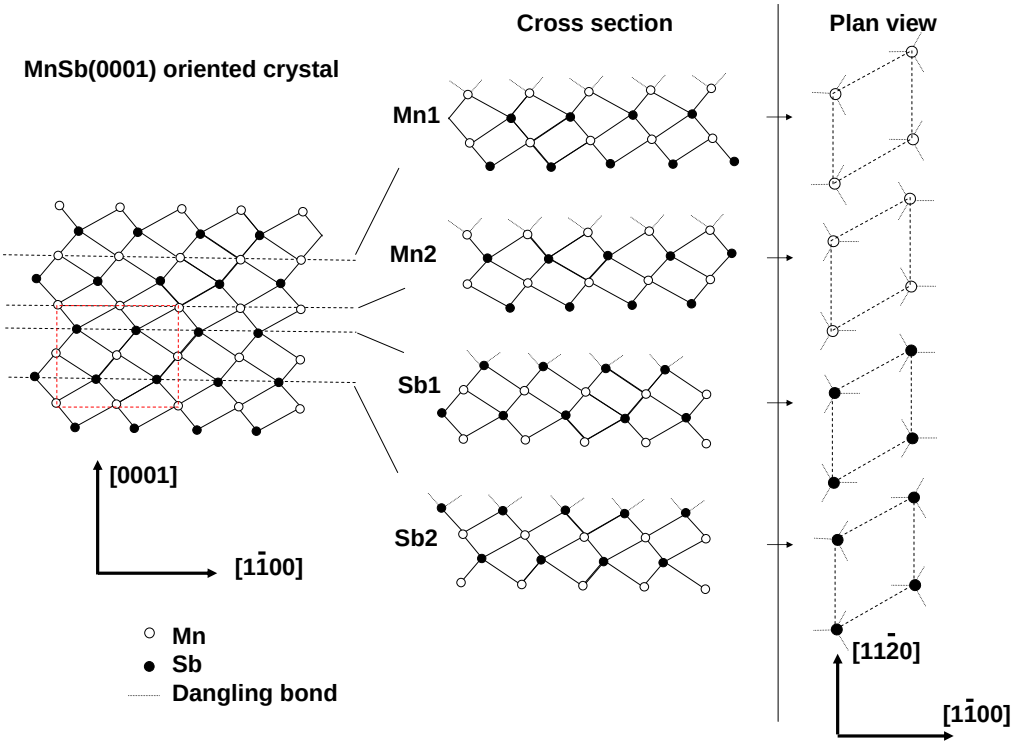

Figure 4.1: MnSb(0001) oriented crystal projected onto the (1100) plane. The unit cell is shown in red. Four bulk terminated surfaces are illustrated on the right, with plan view schematics of the surface structures.

more detail, MnSb(0001) samples were grown under the standard conditions described in Section 3.2.3 and imaged with STM.

The STM images in Figure 4.2 show typical surfaces for samples after either quenching (panel a, removed from the growth chamber less than 1 minute after the end of growth) or annealing (panel b, annealed for $\sim$ 16 hours at 400°C). Both the quenched and annealed surfaces show large terraces (typically $>$ 1000 Å) and step edges with distinct preferential directions. These directions are rotated by 60° from one another, indicating hexagonal symmetry. Step heights from the annealed MnSb(0001) surface obtained by STM are plotted in Figure 4.3, with dashed lines indicating the step heights expected for mono-layers and bi-layers of MnSb. Figure 4.3 does not show any *atomic* mono-layer steps ($c/4 = 1.44$ Å), proving that the surface is terminated by a single element. The presence of both MnSb mono-layer and bi-layer steps however indicates that both types of elemental termination (Mn1+Mn2 or Sb1+Sb2) are present. The rapid quenched surface typically exhibited smaller terraces separated by mono-layer

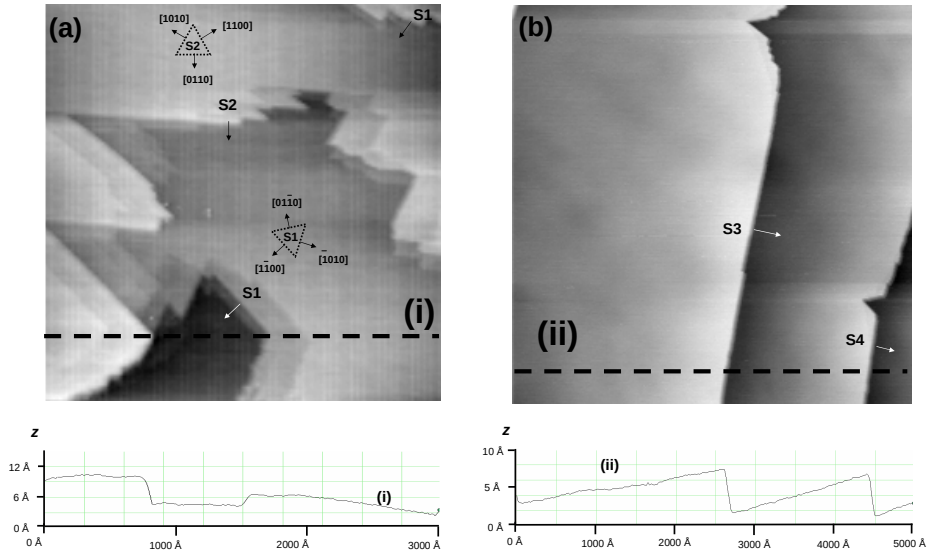

Figure 4.2: MnSb(0001) surfaces imaged using STM. Panel a shows a 3000 Å $\times$ 3000 Å region of the surface obtained after quenching the sample in $<$ 1 minute. Panel b shows a 5000 Å $\times$ 5000 Å region of the surface obtained after annealing the sample for 16 hours. Tunnelling conditions used were $V = +3$ V and $I = 0.2$ nA. The arrows show step-down directions of a number of steps. The two inequivalent sets of step directions are also indicated in panel a. Note the image drifts slightly and so the angles between steps are not exactly 60°. Some double tip effects are also visible.

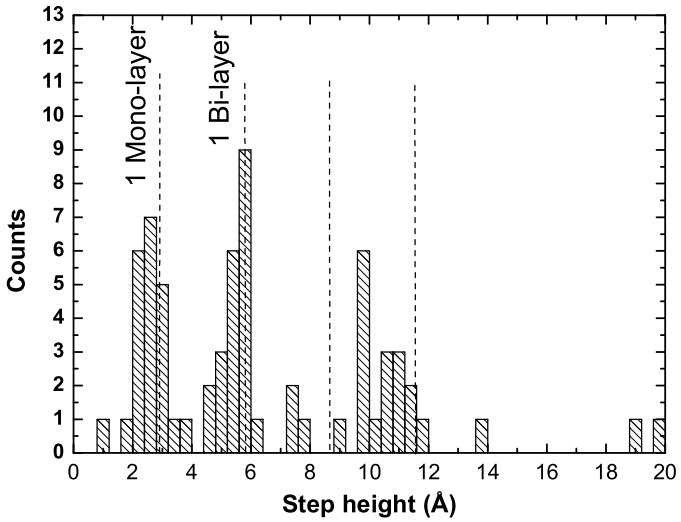

Figure 4.3: Histogram of step heights for MnSb(0001) surfaces obtained from STM images after annealing for 16 hours. Dashed lines indicate integer numbers of MnSb mono and bi-layer step heights.

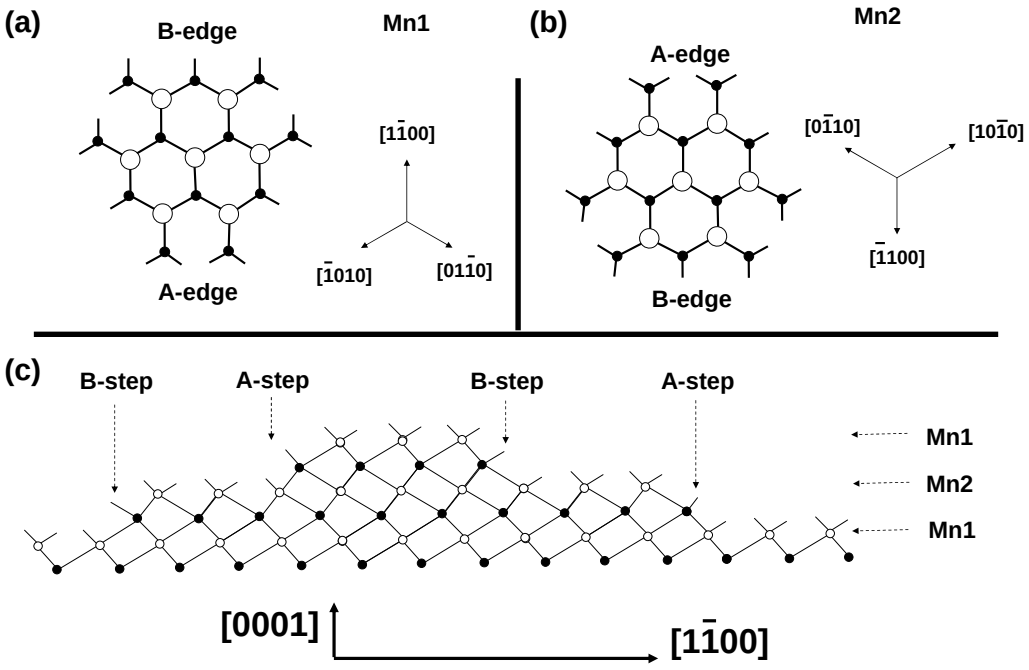

Figure 4.4: Illustration of the MnAs(0001) step model of Kästner *et al.* [63]. (a) Mn1 surface steps (b) Mn2 surface steps (c) (1100) projection of bulk terminated MnSb(0001) A and B steps. Filled (empty) circles indicate Sb(Mn) atoms. Circle size in panels a and b indicate the relative height of the atoms.

steps, while the long annealed samples had larger terraces and a greater number of bi-layer steps.

As previously noted, the step edges on the MnSb(0001) surface have clear preferential directions. Step edges are defined as the direction normal to a step, pointing in the step-down direction. The morphology of step edges on MnAs(0001) has been discussed in detail by K$\ddot{a}$stner *et. al.* [63], whose model is illustrated in Figure 4.4. Panel c shows the projection of a MnSb(0001) oriented crystal with a number of steps in the [1$\bar{1}$00] and [$\bar{1}$100] directions. It is assumed that only atoms with three back bonds are stable at the step, and a Mn termination has been assumed, although the argument is equally valid for an Sb terminated surface. Panels a and b show plan views of the relative bond orientation of Mn1 and Mn2 surface step edges. In addition to the terminating Mn atoms, the second atomic layer of Sb and their top facing bonds are shown. From these panels two types of step edge can be defined. For Mn1, in the [$\bar{1}$100] step direction (in addition to the [10$\bar{1}$0] and [0$\bar{1}$10]) Sb atoms at the step edge

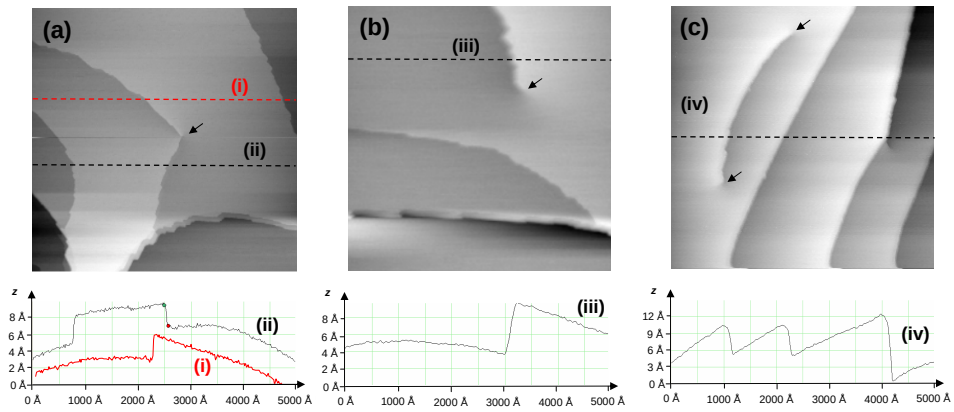

Figure 4.5: 5000 Å × 5000 Å STM images of MnSb(0001) surfaces with dislocations shown by arrows. These correspond to (a) a double MnSb mono-layer dislocation with a positive screw direction, (b) a single MnSb bi-layer dislocation with a positive screw direction and (c) two interfering bi-layer dislocations with opposite screw directions. Tunnelling conditions used were V = -1.4 V and I = 2 nA.

have two dangling bonds, while in the $[1\bar{1}00]$ they have only one. These are labelled A and B edges respectively, and from minimisation of dangling bonds B-edges are likely to be more stable. Thus on the Mn1 surface, B-type step edges in the $[\bar{1}010]$, $[1\bar{1}00]$ and $[01\bar{1}0]$ directions are expected. On the Mn2 layer, bond directions are rotated by 60°C, and as such the B-edges are in the $[10\bar{1}0]$, $[\bar{1}100]$ and $[0\bar{1}10]$ directions. K*ä*stner *et. al.* have observed these alternating step edge directions on MnAs(0001) using STM [63].

This model also matches the steps observed in Figure 4.2 for the MnSb(0001) surfaces obtained in the current work. The effect is most notable in the rapid quenched surfaces (Figure 4.2a), with the steps S1 and S2 shown demonstrating the clearly different sets of step directions. The same pattern is observed for the mono-layer steps on the annealed surface. Figure 4.2b shows two bi-layer steps on the annealed surface. The bi-layer steps demonstrate triangular kinks which are formed from both step sets. This is to be expected since any bi-layer step is formed from the combination of an A and B step and so a mixture of all six step directions is more likely.

Figure 4.5 shows a range of screw dislocations observed on the MnSb(0001) surface. Panel a shows a dislocation with two MnSb mono-layer step edges rotating in a positive screw direction, while panel b shows the same screw component, but with a single bi-layer step. Panel c shows two dislocations with opposite screw directions

which interfere destructively. A wide area of the surface was surveyed, and dislocations with positive and negative screw components were observed. All dislocations displayed a Burgers vector of $\pm c$[0001], either with a single MnSb bi-layer step or two MnSb mono-layer steps. This is consistent with the ABACA stacking order of the bulk MnSb crystal, since if the B and C layers were equivalent, dislocations with Burgers vectors of $c/2$ would have been observed. These measurements do not provide information of the stacking order at the surface, since the Burgers vector of the dislocation observed at the surface is determined by the crystallography of the bulk. The dislocation density estimated from the STM survey is of the order of 10^8 cm^{-2}, in close agreement with the observations of Kästner *et. al.* regarding MnAs(0001) grown on GaAs(111)B [63].

From these STM results, a number of inferences can be made regarding the MnSb(0001) surface. Assuming the bulk termination model shown in Figure 4.1, the presence of MnSb(0001) mono-layer steps indicates that terraces of Mn1 and Mn2 (or Sb1 and Sb2) are present with approximately equal probability. The different step directions of subsequent terraces indicate that the two terrace types are indeed structurally different. A surface is then expected to consist of alternating domains separated by mono-layer steps. The reconstruction periodicities are expected to be the same for the different terraces, although the actual reconstruction structures are expected to be rotated by 60°. Atomic resolution STM on either side of a step may allow direct observation of these different orientated structures.

4.2.3 Surface reconstructions of MnSb(0001)

In Chapter 3, sharp (2×2) RHEED patterns have been observed on MnSb(0001) surfaces during growth, in addition to a (1×1) pattern believed to be associated with deterioration of the surface quality due to adsorption of excess Sb. The (2×2) pattern is the most stable reconstruction, and all other phases appear to revert to the (2×2) after vacuum annealing. In order to observe additional reconstructions on MnSb(0001), the surface was exposed to Mn and Sb fluxes individually while annealing the sample at temperature T. The BEPs for the Mn and Sb cells were set to P_{Mn}= 1×10^{-7} mbar and P_{Sb}= 8×10^{-7} mbar. Surface reconstructions were observed to change as a function of T and exposure time to Mn and Sb fluxes.

The (1×1) reconstruction was found to change to a (2×2) by a brief exposure to

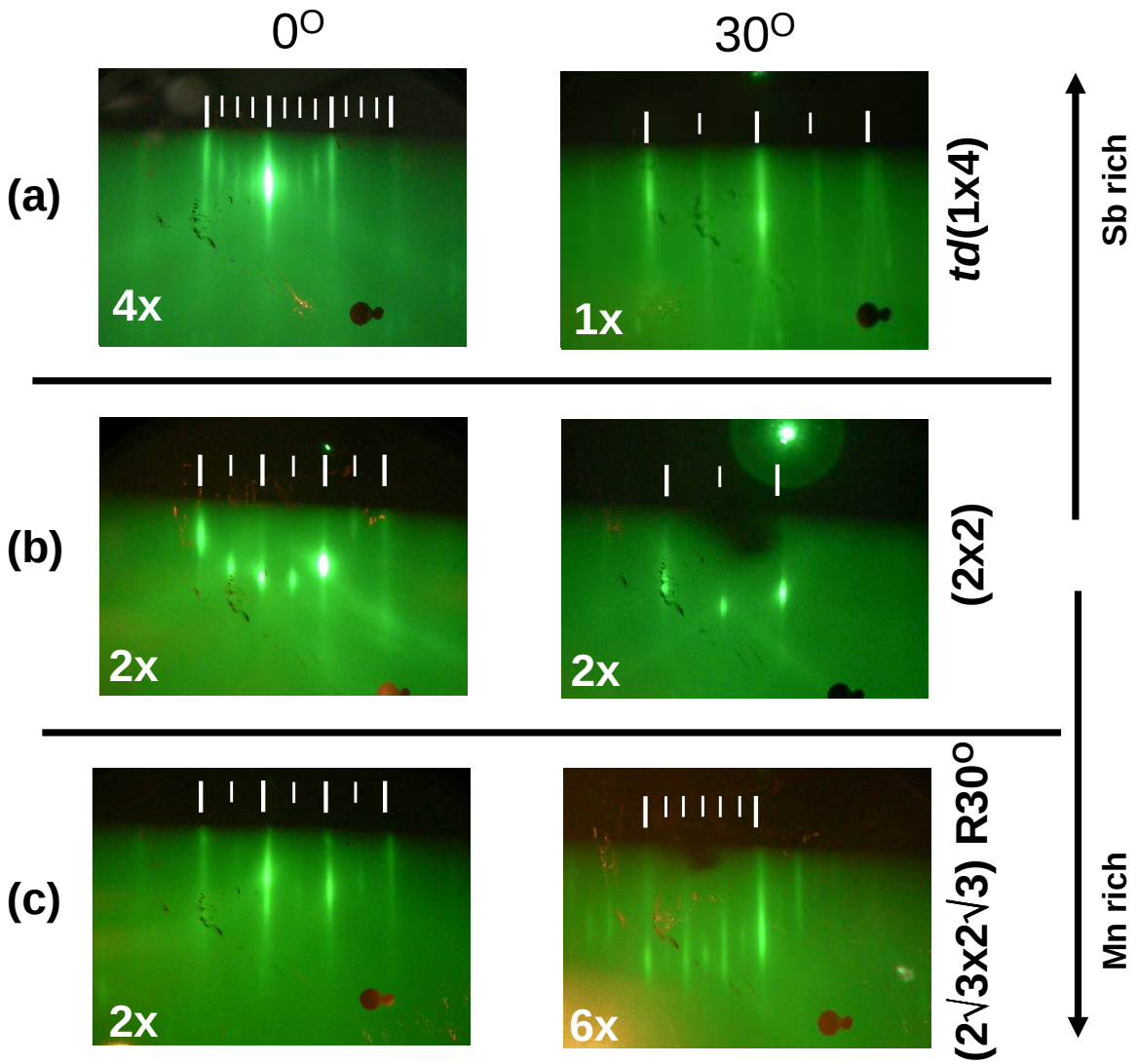

Figure 4.6: RHEED patterns observed on MnSb(0001) surfaces along two high symmetry directions. (a) Sb rich triple domain (1×4), (b) stable (2×2) and (c) Mn rich $(2\sqrt{3}\times 2\sqrt{3})$R30°. Strong $\frac{2}{6}$ and $\frac{4}{6}$ order streaks at 30° in panel c indicate a coexisting $(\sqrt{3}\times\sqrt{3})$R30° phase. Integer (fractional) order streaks in the RHEED images are indicated by long (short) lines.

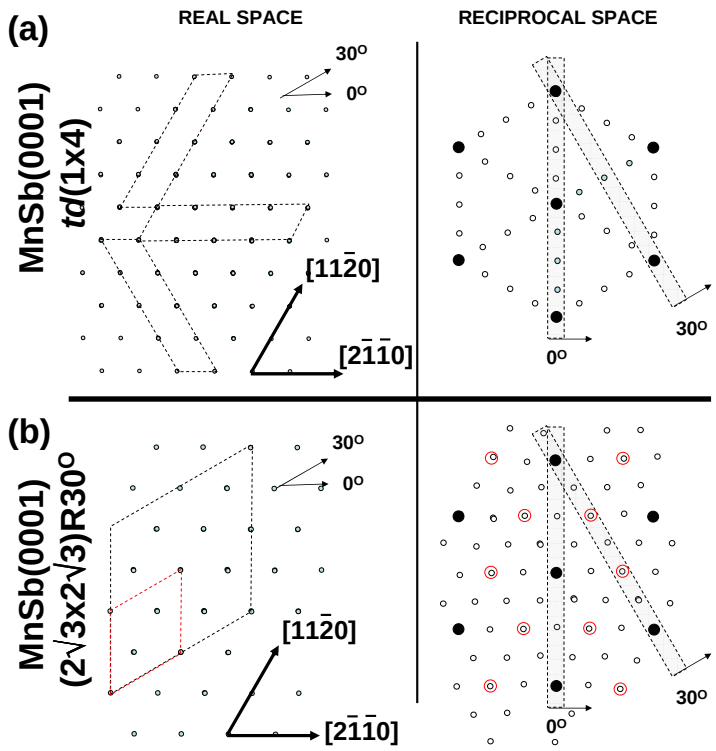

Figure 4.7: Real and reciprocal space periodicities for MnSb(0001) (a) $td(1\times4)$ and (b) $(2\sqrt{3}\times2\sqrt{3})$R30° surface reconstructions. The shaded regions in the reciprocal space panels indicate the recording plane of the RHEED when the electron beam is in the direction indicated by the attached arrow. The solid (empty) circles indicate integer (fractional) order diffraction features. Directions are consistent across all the panels. In panel b, the red lines and circles indicate the $(\sqrt{3}\times\sqrt{3})$R30° reconstruction.

the Mn flux and could be reformed by exposure to the Sb flux. The (1×1) reconstruction is identified as an Sb rich surface, entirely consistent with excess Sb induced disorder. The (1×1) phase is unstable in the temperature range studied in the absence of an Sb flux, and changes back to (2×2) after annealing. The $(1\times1)\rightarrow(2\times2)$ transition was observed at all temperatures studied, and has been used as a reference point for all other phase transitions.

As more Sb was deposited on the (1×1) surface, a third reconstruction was observed at temperatures below 370°C. This reconstruction demonstrates a $4\times$ periodicity in the 0° direction, while a $2\times$ is observed at 30°. The streaks in the 30° direction are all rather long, and show apparent facet-like features. These RHEED images are shown in Figure 4.6a. The periodicities are consistent with a $td(1\times4)$ reconstruction as illus-

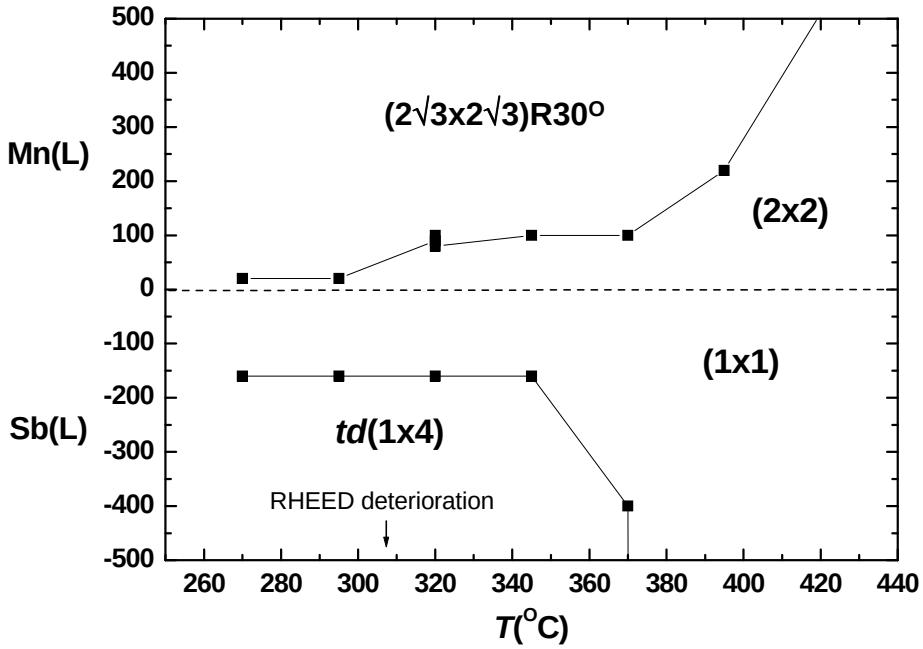

Figure 4.8: Deposition of Mn (positive values) and Sb (negative values) required to bring about various surface reconstruction transitions starting from the (1×1)→(2×2) transition.

trated in Figure 4.7a. The facet-like features are identified as the fractional 4× streaks between the first and second Laue zone. The td(1×4) is a highly Sb rich reconstruction, which is consistent with the instability of this phase at higher temperatures where the desorption of Sb is rapid. Even at the lower temperatures, the td(1×4) reconstruction is not stable in the absence of an Sb flux, and eventually deteriorates to the (1×1) and then the (2×2). As Sb is continually deposited on the td(1×4) reconstruction at lower temperatures, the pattern deteriorates, and the RHEED features become more diffuse, consistent with a build up of excess Sb on the surface.

Starting from the stable (2×2) reconstruction, Mn was deposited at various temperatures. After a short exposure, the appearance of a fourth reconstruction was observed. This reconstruction is characterised by 2× in the 0° and 6× in the 30° direction, and corresponds to a $(2\sqrt{3} \times 2\sqrt{3})$R30° reconstruction as shown in Figure 4.7b. The RHEED patterns for this reconstruction in the two high symmetry directions are shown in Figure 4.6c. The 1/6, 3/6 and 5/6 streaks are fairly weak, while the 2/6 and 4/6 are considerably stronger. This may imply coexisting regions of $(\sqrt{3}\times\sqrt{3})$R30°. Recent results have indicated that a $(\sqrt{3} \times \sqrt{3})$R30° reconstruction is obtained by IBA of a MnSb(0001) surface, although this has still to be confirmed by further experiments. As with all the other reconstructions on MnSb(0001), the $(2\sqrt{3} \times 2\sqrt{3})$R30° could be

converted back to the (2×2) reconstruction, although this time by exposure to an Sb flux. The quantity of Mn required to achieve the (2×2)→$(2\sqrt{3} \times 2\sqrt{3})$R30° transition shows some temperature dependence, with more Mn required at higher temperatures to bring about the transition. This is rather unexpected, since the increase in temperature is not expected to affect the desorption rate of Mn significantly, and if anything, the increased temperature should make the surface less Sb rich, and intuitively easier to form the Mn rich reconstruction. The quantities of Mn and Sb required to bring about various reconstruction transitions are plotted in Figure 4.8. In this figure, the vertical axis shows the quantity of Mn (positive values) and Sb (negative values) deposited in Langmuirs (1 L = deposition at 10^{-6} mbar for 1 s) required to achieve a phase transition at each temperature, starting from the (1×1) to (2×2) transition.

4.3 MnSb(1$\bar{1}$01)

4.3.1 MnSb(1$\bar{1}$01) surface morphology

MnSb(1$\bar{1}$01) surfaces were obtained by growth on GaAs(001) substrates under standard conditions. Figure 4.9 shows a bulk terminated (1$\bar{1}$01) oriented crystal projected onto the (1100) plane. As with the MnSb(0001) crystal, there are four possible terminations for the crystal, which have been illustrated on the right side of the figure. All terminations have an oblique unit mesh. Unlike the (0001) surface, the terminations are all distinctly different and all four surfaces are highly corrugated, forming a range of complicated dangling bond arrangements. From bond counting arguments, structures Mn2 and Sb2 are considered less likely, with seven dangling bonds per unit mesh, while Mn1 and Sb1 have only five. In addition to the large number of dangling bonds, the Sb2 surface has an Sb atom which is only weakly bound by two back bonds to the bulk and four dangling bonds. These are unlikely to be stable, and removing them results in the Mn1 surface.

The definitions of mono-layers and bi-layers for the MnSb(1$\bar{1}$01) surface are rather more complex than for the (0001) surface since the different planes are not evenly spaced. Bi-layers for Mn and Sb terminated surfaces are equal, with an ideal separation of 3.01 Å. Two different mono-layer separations must be defined for each termination since the ordering of the Mn and Sb atoms in MnSb is different (Section 1.6.1). Since

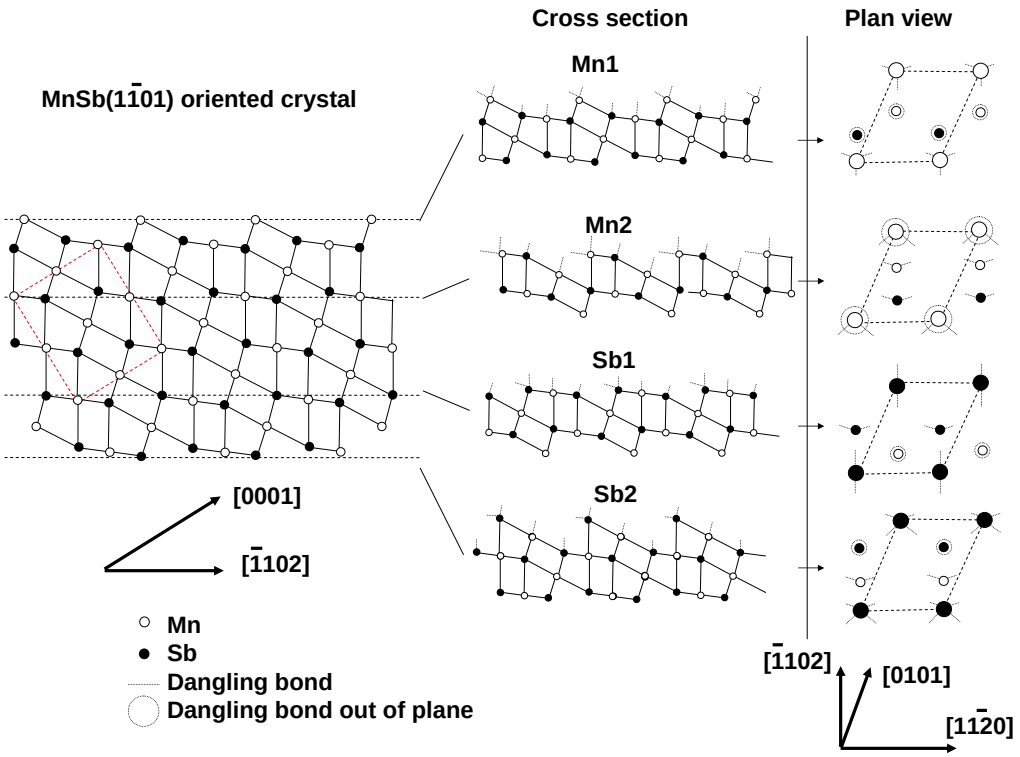

Figure 4.9: MnSb(1$\bar{1}$01) oriented crystal projected onto the (1100) plane. The unit cell is shown in red. Four bulk terminated surfaces are illustrated on the right, with plan view schematics of the surface structures.

the Mn atoms (in the A hexagonal close packed layers) are evenly distributed in the structure, the step height downwards from Mn1 to Mn2 layers d_{12}^{Mn} and that down from Mn2 to Mn1 d_{21}^{Mn} are the same at 1.5 Å. For Sb in the alternating B and C hexagonal close packed layers, the separations are different, with values of d_{12}^{Sb}=0.48 Å and d_{21}^{Sb}=2.53 Å. If the MnSb(1$\bar{1}$01) bulk surface is terminated by alternating Sb1, Sb2 terraces, it should be possible to observe an alternating mono-layer step height in STM.

4.3.2 Scanning tunnelling microscopy imaging of MnSb(1$\bar{1}$01) surfaces

STM images of the MnSb(1$\bar{1}$01) surface are shown in Figure 4.10. These images are both 3000 Å × 3000 Å in size, and were imaged with sample bias +3 V and 0.2 nA tunnelling current. Unlike the (0001) surface, no clear set of preferential step directions are apparent across the sample, although some long straight steps are observed in Figure 4.10. Step heights obtained from the STM images are shown in Figure 4.11. As with the steps observed on the (0001) surface, step heights are consistently smaller than the

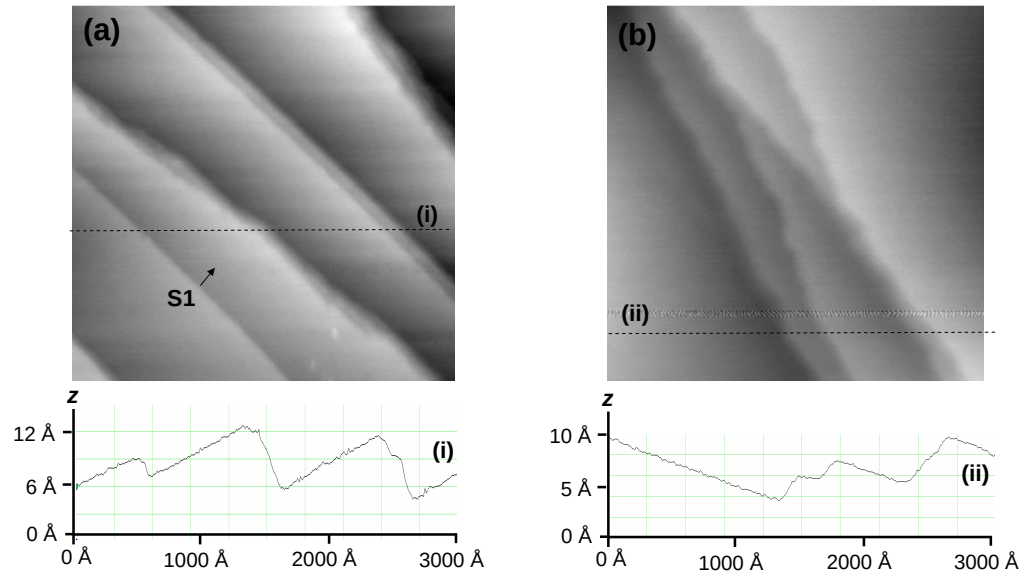

Figure 4.10: MnSb(1$\bar{1}$01) surfaces imaged using STM. Both 3000 Å $\times$ 3000 Å images were obtained after a 16 hour anneal. Tunnelling conditions used were $V = +3$ V and $I = 0.2$ nA. The slope on the cross sections are caused by the global plane fitted by the STM software, and currently cannot be compensated for. This slope makes step height measurements problematic as described in Section 2.11.

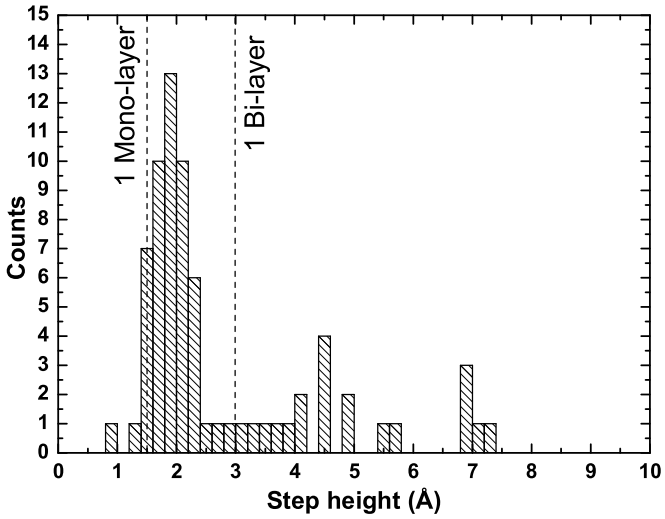

Figure 4.11: Histogram of step heights for MnSb(1$\bar{1}$01) surfaces from STM images obtained after a 16 hour anneal. MnSb mono and bi-layer step heights shown are for Mn terminated surfaces (d_{12}^{Mn}=d_{21}^{Mn}=1.5 Å).

bi-layer height, indicating multiple surface terminations or a deviation from ideal bulk termination. Figure 4.10b shows a series of steps, each with a similar step height of 1.9 Å. This image is inconsistent with the alternating d_{12}^{Sb} and d_{21}^{Sb} expected for an Sb ideal bulk terminated surface. The steps are also slightly too large for the Mn terminated surface with d_{12}^{Mn}=1.5 Å.

4.3.3 Surface reconstructions of MnSb(1$\bar{1}$01) surfaces

In Section 3.4, MnSb(1$\bar{1}$01) RHEED patterns were observed and used to identify the growth orientation. Discussion of the surface reconstruction was postponed until this point in the thesis due to the unusual nature of the surface. As described previously, the oblique surface is formed from tessellating parallelograms and so is rather different from the cubic (001) and hexagonal (111) or (0001) surfaces discussed elsewhere. Since this surface has not been reported in detail in the literature, a labelling convention for the surface reconstructions is required. A number of choices are illustrated in Figure 4.12, which shows the real space reconstruction directions for an (n×m) reconstruction. Convention a seems the most natural, since it labels two very different crystallographic directions, unlike c which labels two symmetrically identical directions. Convention b has a small angle between the vectors, and so the reconstruction using this convention will badly reflect the actual size of the surface structures. Convention a will be used from this point onwards, with the n× representing a reconstruction periodicity along the [11$\bar{2}$0] direction and m× along the [0101].

As a result of the unusual symmetry of the (1$\bar{1}$01) surface, determination of the reconstructions using RHEED was rather more difficult than for the more typical (001) and (111) III-V surfaces. As such, three different RHEED images are presented for each reconstruction, in order to confirm the surface periodicity proposed. The first reconstruction (shown in Figure 4.13a) was observed during growth, and was characterised by a 2× RHEED pattern along the 0° azimuth. A 2× was also observed at the perpendicular 90° azimuth, while no fractional order streaks were observed at 45°. This pattern is shown in Figure 4.13, and is identified as a (1×2) reconstruction. The real and reciprocal lattice periodicities for this reconstruction are shown in Figure 4.14a.

A second surface reconstruction appeared quickly after growth was halted. The (1×2) pattern faded, leaving rather a weak RHEED pattern. The 0° azimuth showed no

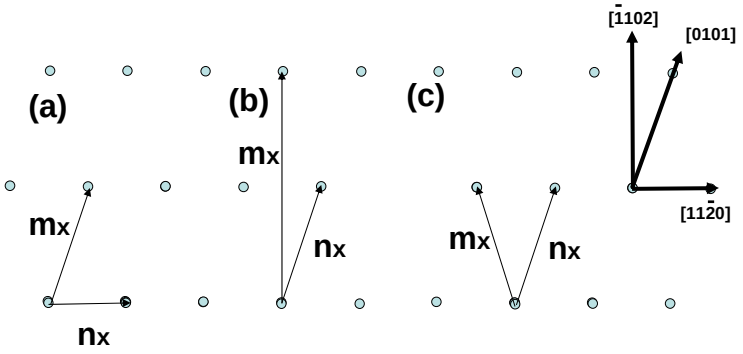

Figure 4.12: Real space periodicity directions for an (n×m) reconstruction on the MnSb(1$\bar{1}$01) surface

fractional order streaks, while the 90° image showed a number of closely spaced fractional order streaks consistent with 7× periodicity. These images are shown in Figure 4.13b, although the 7× is rather hard to make out on the printed copy. In the 45° azimuth, an apparent asymmetric 3× appeared with the streaks staggered slightly, which has been labelled s(3×) in the RHEED image. The s(3×) was the most distinct feature of this reconstruction. Real and reciprocal space periodicities have been determined for this reconstruction, and are shown in Figure 4.14b. The structure shown agrees with all the RHEED observations, including the staggered 3× at 45°. This reconstruction cannot be labelled using the usual Wood notation with the chosen labelling convention. Instead, it must be written using the matrix notation described in Section 1.3.2 and is defined by the matrix G

$$G = \begin{pmatrix} 3 & 1 \\ -1 & 2 \end{pmatrix}$$

The dimensions of this reconstruction are similar to those of a (4×2), although rotated and distorted slightly. For ease of reference, this reconstruction is referred to as a distorted (4×2) or dis(4×2). The dis(4×2) reconstruction is the most thermally stable reconstruction on MnSb(1$\bar{1}$01), but can be converted into the (1×2) by deposition of Sb and during growth (presumably under Sb rich conditions). No further reconstructions have been observed on the (1$\bar{1}$01) surface to date. Since there is only one reconstruction transition, a phase map similar to that of Figure 4.8 is not possible for the (1$\bar{1}$01) surface.

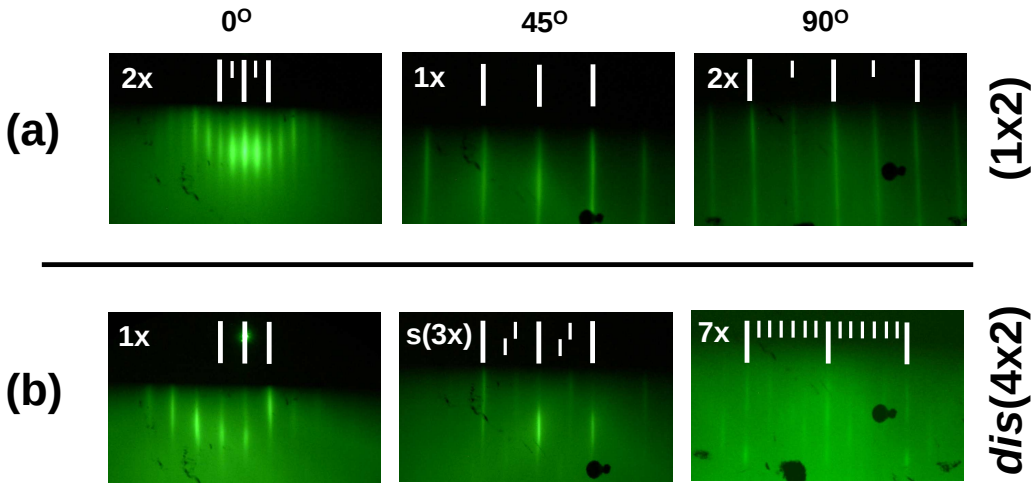

Figure 4.13: RHEED images for MnSb(1$\bar{1}$01) (a) (1×2) and (b) dis(4×2) surface reconstructions. RHEED images are shown with the electron beam along three directions, 0°, 45° and 90°. Integer (fractional) order streaks in the RHEED images are indicated by long (short) lines.

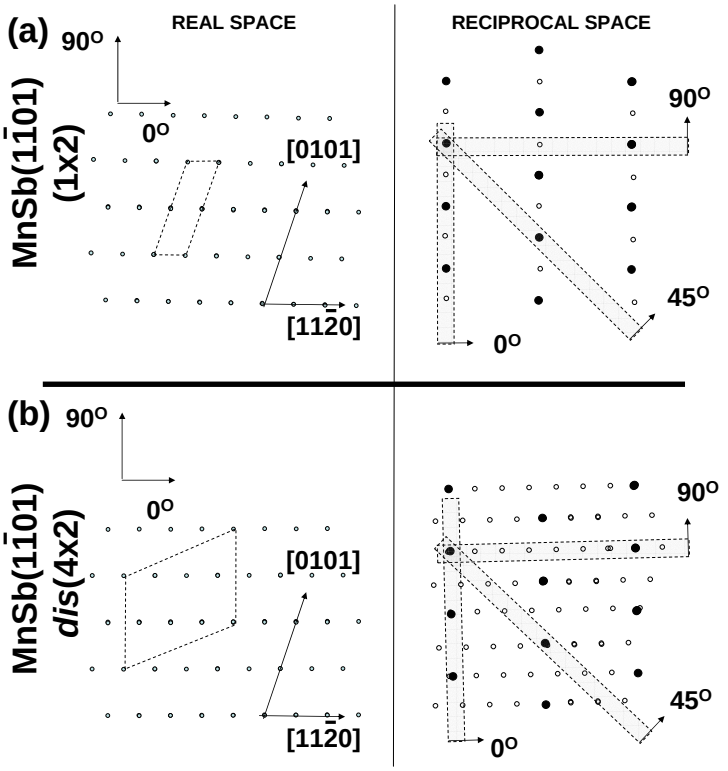

Figure 4.14: Real and reciprocal space periodicities for MnSb(1$\bar{1}$01) (a) (1×2) and (b) dis(4×2) surface reconstructions. The shaded regions in the reciprocal space panels indicate the recording plane of the RHEED when the electron beam is in the direction indicated by the attached arrow. The solid (empty) circles indicate integer (fractional) order diffraction features. Directions are consistent across all the panels.

Surface	Reconstruction	Composition	Observed before?	Relevant models	Figure 4.17
MnSb(0001)	$(\sqrt{3}\times\sqrt{3})$R30°	Mn rich	No	InN(0001)	
	$(2\sqrt{3}\times 2\sqrt{3})$R30°	↓	No	InSb(111) [43] AlN(0001) [98]	
	(2×2)	stable	Yes [64]	MnAs (0001) As adatom [65] MnAs(0001) large trimer [74] III-V (111) trimer [99] III-V (111) vacancy [41] GaN(0001) [100]	a,b e,f c,d e,f
	(1×1)	↑	Yes [66]	Disordered surface	
	td(1×4)	Sb rich	No	MnAs- td(1×3)[65] In/Si(111) [101]	g-l m-n
MnSb($1\bar{1}01$)	dis(4×2)	stable	No		
	(1×2)	Sb rich	No		

Table 4.1: Summary of MnSb surface reconstructions and similar reconstructions on similar materials.

4.4 Literature survey of relevant reconstructions

In this section, reconstructions from the literature which are similar to those observed on MnSb surfaces are discussed. The results of this literature search are shown in Table 4.1.

MnAs and MnSb(0001) (2×2)

As the most stable reconstruction on the MnSb(0001) (and MnAs(0001)) surface, in addition to being the typical reconstruction during growth, the (2×2) reconstruction is the most important reconstruction to understand. The (2×2) reconstruction has been observed on MnAs and MnSb by a number of groups [65, 74, 64, 63] and two groups have studied the reconstruction on MnAs using STM, and indicated possible structures. Both groups observe triangular features in the atomic scale STM images. Ouerghi *et. al.* have proposed two structures; an As adatom model in 2003 [65] and a large As trimer in 2006 [74]. The (2×2) models proposed by Ouerghi *et al.* are proposed in conjunction with a model for the td(1×3) also observed on the MnAs(0001) surface. The relative heights of the two MnAs(0001) reconstructions in a multiple domain STM image were observed, in addition to the coverage of As required to convert the (2×2) to the td(1×3). This model seems highly plausible, although no comment on the actual bonding type (sp^3, octahedral or triangular prism) was made. The second group, Ploog *et. al.* also observed triangular features in the atomic scale STM images and an As trimer model (similar to the As trimer observed on GaAs(111)B [99]) was proposed [63]. The three structures for MnAs(0001) (2×2) proposed in the literature are illustrated in Figure 4.15.

In addition to the (2×2) trimer observed on III-V (111)B surfaces, a second (2×2) reconstruction is also observed on the group III rich III-V (111)A surfaces. This is attributed to a vacancy model [41] which has similarities to the most recent model of Ouerghi *et al.*. A number of wurtzite materials (GaN, AlN) also display a (2×2) reconstruction on the hexagonal (0001) surfaces. For these surfaces an adatom model was proposed [100], which is similar to the 2003 model of Ouerghi *et al.* for MnAs(0001).

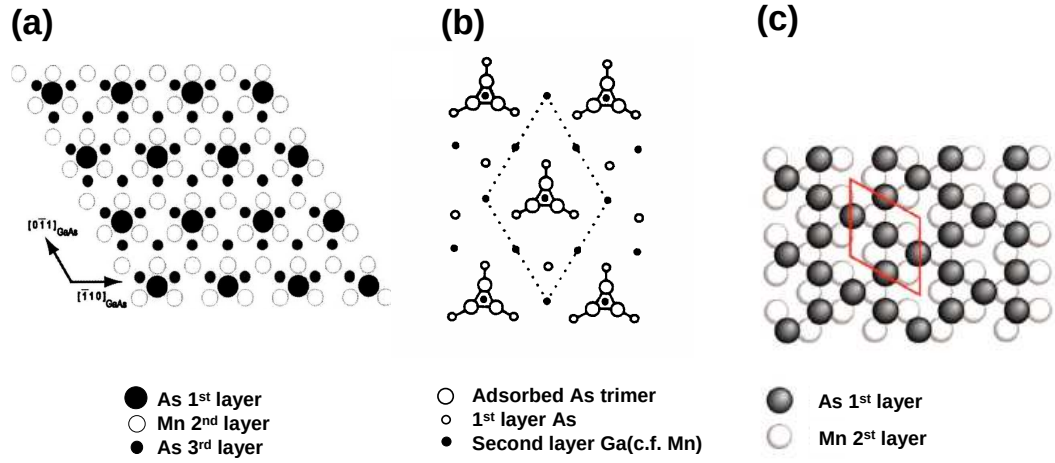

Figure 4.15: Atomic arrangements for (2×2) reconstructions of MnAs(0001), proposed by (a) Ouerghi *et al.* (2003) [65], (b) Ploog *et al.* (based on the GaAs(111)B (2×2) proposed by Biegelsen *et al.* [99]) and (c) Ouerghi *et al.* (2006) [74].

MnSb(0001) td(1×4)

The MnSb(0001) td(1×4) reconstruction has not been previously reported. This reconstruction is the most Sb rich, and occurs only at low temperatures (<370°) indicating rather weakly bound Sb on the surface. However, on MnAs(0001), a similar reconstruction, a td(1×3), has been observed by Ouerghi *et. al.* [65, 74]. From STM images of the td(1×3) 'sticks' in the three symmetrically identical directions were observed, and from the relative height of neighboring (2×2) and (1×3) domains, the sticks were proposed to be $\frac{1}{3}$ ML As on a full As layer. This structure is illustrated in Figure 4.16a. Importantly, this assignment is based on the assumption that the model presented in the paper for the coexisting (2×2) is accurate. The td(1×3) model can easily be modified to provide a 4× periodicity instead of the 3× by changing the separation or width of the sticks, and hence it is a good candidate for the td(1×4) on MnSb. A second possible mechanism for this reconstruction can be proposed from the structure observed when In is deposited on Si(111) [101]. This td(1×4) has a full In over-layer, but relaxation in the over-layer provides a 4× periodicity in one direction. This is shown in Figure 4.16b.

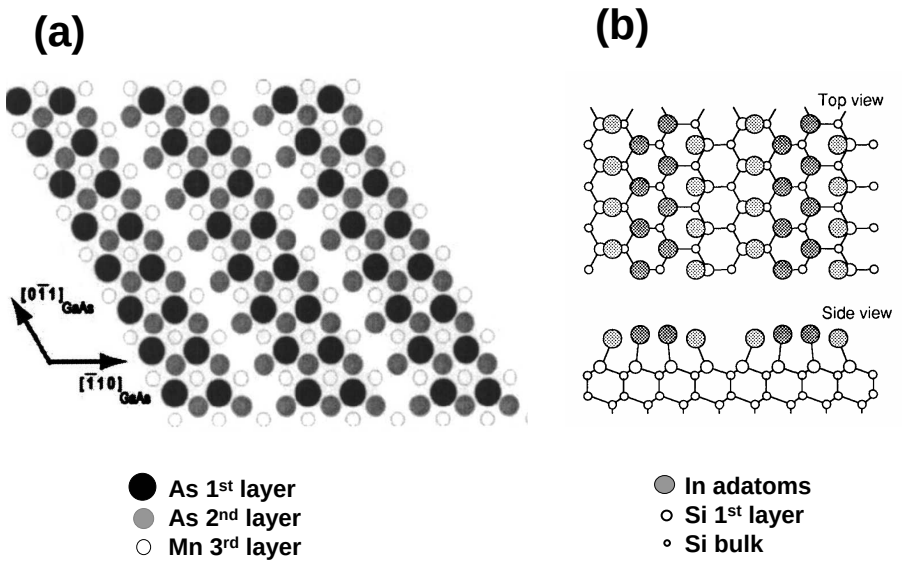

Figure 4.16: Atomic arrangements for reconstructions similar to the $td(1\times4)$ observed on MnSb(0001). (a) MnAs(0001) $td(1\times3)$ proposed by Ouerghi *et al.* [65] and (b) $td(4\times1)$ In on Si(111) proposed by Abukawa *et al.* [101].

MnSb(0001) ($2\sqrt{3}\times2\sqrt{3}$)R30°

The $(2\sqrt{3}\times2\sqrt{3})$R30° reconstruction has not been reported to date, and no similar structures have been observed on MnAs. This is a relatively large reconstruction, and as such the model may be rather complex. As an example, the $(2\sqrt{3}\times2\sqrt{3})$R30° reconstruction on InSb(111)A proposed by Nishizawa *et al.* has four reconstructed layers with inter-layer dimers [43]. While the $(2\sqrt{3}\times2\sqrt{3})$R30° is the most Sb rich reconstruction on InSb, it is the most Mn rich on MnSb. It is therefore highly unlikely that they share a common structure. A more comparable surface reconstruction may be the $(2\sqrt{3}\times2\sqrt{3})$R30° observed on AlN(0001) under Al rich conditions. This is attributed to $\frac{4}{3}$ ML Al contracted and rotated with respect to the bulk [98].

MnSb(1$\bar{1}$01) reconstructions

As stated earlier, the MnSb(1$\bar{1}$01) surface is highly complicated, and entirely unlike any other commonly studied surface, and as such no relevant literature has been found. Kästner *et al.* proposed a model for the MnAs(1$\bar{1}$00) (1×2) reconstruction [59], although it should be noted that due to the very different geometry and symmetry

of the $(1\bar{1}00)$ and $(1\bar{1}01)$ surfaces, this has few similarities to the (1×2) observed on MnSb$(1\bar{1}01)$ in the current work.

4.5 Discussion of structures for MnSb surfaces

In this section, some criteria for assessing proposed surface reconstructions on MnSb(0001) surfaces are considered. Similar considerations are likely to be relevant for the MnSb$(1\bar{1}01)$ surfaces. Due to the similarities between MnAs(0001) and MnSb(0001), the literature for the two are referred to interchangeably.

4.5.1 Surface termination

From the ideal bulk terminated structure model in Figure 4.1 there is no preferable termination for the MnSb(0001) surface from minimisation of dangling bonds. From DFT calculations by Jenkins [102], the Sb terminated MnSb(0001) surface has been calculated to be thermodynamically more stable. Similarly, a group V terminated surface was implied by Ploog *et al.* when proposing a trimer structure for the (2×2) MnAs(0001) reconstruction [63]. Intuitively, a Sb terminated surface seems likely, since the samples are grown under Sb rich conditions during which the (2×2) surface reconstruction is observed. In contrast, Rader *et al.* identified a feature in experimental valence band spectra which was only obtained in calculations for a Mn terminated or Mn rich surface reconstruction [103]. Ouerghi *et al.* have proposed two models for the (2×2) reconstruction. In 2003, they proposed a As adatom on a full layer of Mn [65], while a more recent paper proposed an As trimer on a full Mn layer on the basis of improved STM images [74]. The argument in these papers for As adatom(s) on a Mn layer was based on STM imaging of two coexisting phases, (2×2) and td(1×3), and measurement of the quantity of As required to move from one to the other. In the authors opinion this work by Ouerghi is the most convincing evidence regarding the nature of the surface and the reconstructions, although this is based on the assumption that the td(1×3) reconstruction has only a 2 ML As surface termination, and breaks down if the As coverage is significantly greater than this. Highly group V rich III-V surfaces are feasible, such as the (2×5) GaSb(001) surface proposed by Thibado *et al.* [104], which was terminated by 3 ML of Sb.

Since there is no obvious choice for the surface termination, assumptions about the terminating element are avoided by proposing models for a generic material AB with the NiAs structure, in which A and B may be Mn or Sb and switched as required. For the MnSb(0001) surface this is a reasonable assumption as the local bonding configurations at the surface are effectively identical. Since the atomic environments in MnSb($1\bar{1}01$) surfaces are inequivalent, more detailed knowledge of the surface termination will be required in order to propose realistic models.

4.5.2 Bonding configurations at surfaces

The termination of the surface and the formation of surface reconstructions are expected to be predominantly determined by the direction and nature of the dangling bonds occurring as a result of the formation of the surface. MnSb is a metallic compound rather than a semiconductor, and so may be expected to behave like other metallic surfaces. Unlike III-Vs, metals do not have highly directional bonding, and as a result, the clean surface reconstructions tend to be few in number and rather simple (e.g (1×1)). This is certainly not consistent with the numerous reconstructions observed on MnSb(0001). The reconstructions on MnSb are more reminiscent of III-V reconstructions described in Section 1.5.2. For a bulk terminated MnSb (0001) surface, there are three dangling bonds per atom each with three backbonds. Nesbitt *et al.* have suggested that for NiAs surfaces, atoms with three severed bonds such as those found on (0001) surfaces may adopt III-V-like sp^3 hybridization with four bonds in an approximately tetrahedral bonding configuration [105]. Several models for MnAs surface reconstructions have been proposed which all incorporate distinctly sp^3-like reconstructions [63, 65, 74, 59], although no explicit comments on the bonding were made in these studies. Models with sp^3-like bonding seem plausible for the MnSb(0001) surface reconstructions. It should be noted that rehybridisation to sp^3 bonding at the surface may be expected to affect the argument for preferential step directions described in Section 4.2.2. However, since the dangling bond arrangements at A and B step edges will still be different, the preferential step model is still expected to be applicable.

4.5.3 Modified electron counting

In Section 4.6 models for the (2×2) and td(1×4) are presented and assessed using two criteria. The first is dangling bond counting, using the assumption that the surface will minimise dangling bond density where possible. This is likely irrespective of the exact nature of the bonding since the presence of dangling bonds due to the surface requires energy. III-V semiconductor surface reconstructions can be assessed using the electron counting rule described in Section 1.5.3. If the atoms at the surfaces of MnSb do indeed rehybridise into sp^3-like bonding arrangements as proposed by Nesbitt *et al.* [105], there may be some aspects of the electron counting rule which are transferable to MnSb. Hence the second criterion is to apply a modified electron counting rule to the assumed sp^3 hybridized surfaces of MnSb, although clearly the results must be viewed with caution.

In this modified electron counting (MEC) model, the exact electron excess/deficit values used for group III and group V elements in different environments have been expressed by a variable δ. MEC is then carried out in the same way as normal electron counting. It should be noted that an error in this calculation will arise as a result of the transition between NiAs and sp^3 bonding at some point below the top layer. Assuming that each sp^3 bond requires two electrons, the excess/deficit of dangling and dimer bonds may be expressed in terms of the variable δ. Each full sp^3 bond is comprised of δe^- from the cation and (2-δ)e^- from the anion. For III-V electron counting, δ has a value of 3/4. For MnSb, the value is unknown, but is likely to be closer to δ=2/4 as a result of the expected Mn valency of 2. Values for the dimer and dangling bond excess/deficit are shown in Table 4.2.

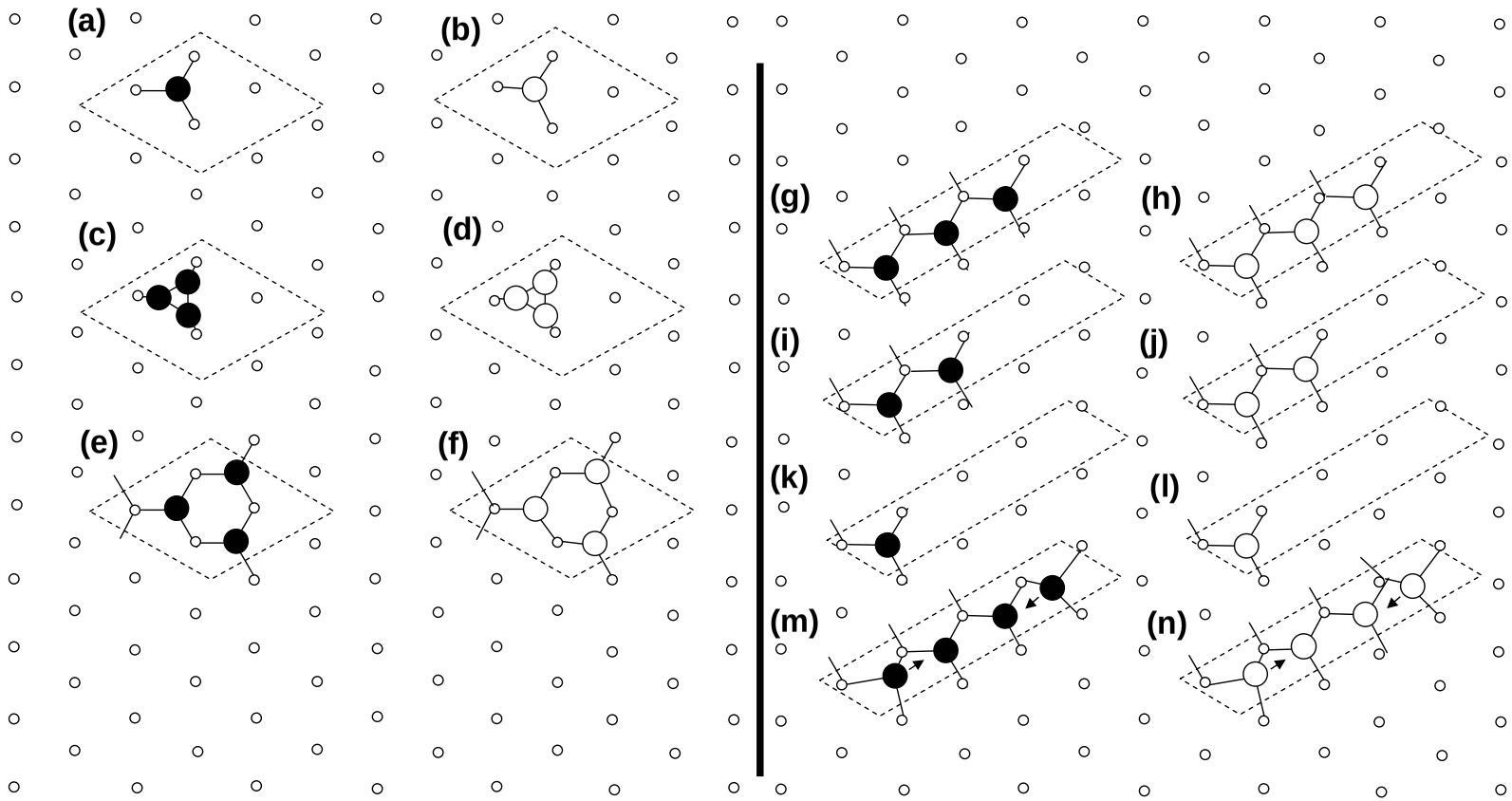

Figure 4.17: Proposed models for the (2×2) (a-f) and td(1×4) (g-n) reconstructions of the MnSb(0001) surface. Empty (filled) circles represent A(B) atoms. Atom sizes indicate the relative heights in the reconstruction.

4.6 Models for MnSb(0001) surface reconstructions

On the basis of a number of models for (2×2) and td(1×4) reconstructions in the literature, Figure 4.17 shows a number of proposed models for these reconstructions on MnSb. The generic material AB is shown, in which A and B may be Mn or Sb as required. For each model, homo (A on A) and hetero (B on A) structures are shown. Model a and b are based on the original adatom model proposed by Ouerghi *et al.* in 2003, c and d the trimer model of Ploog *et al.*, and e and f the vacancy model proposed on III-V (111)A surfaces and the recent Ouerghi model [74]. It should be noted that the term "trimer" can cover structures c-f, although for simplicity, here the large trimers in models e and f are referred to as the vacancy model.

Table 4.2 shows a number of properties of the reconstructions, including bond counting assuming that the surface atoms are allowed sp^3 hybridization as described by Nesbitt *et al.*. The numbers in parentheses show the number of dangling bonds if the surface was bulk terminated (all atoms having 6 bonds). Table 4.2 also shows the results of the modified electron counting applied to a surface where A=Mn and B=Sb. The electron counting values for A=Sb, B=Mn are simply the opposite sign of those shown. It is clear from the table that the sp^3 hybridisation dramatically reduces the number of dangling bonds in each model. The most interesting models are the hetero-adatom and hetero-vacancy models. In these structures there are an equal number of A and B dangling bonds, and so the MEC sums to zero irrespective of the value of δ. The trimer and homo-adatom models obey electron counting for III-Vs, but not generally for all values of δ.

A number of structures have also been proposed for the single domain (1×4) reconstruction, which are shown in Figure 4.17g-n. Models g-l are variations on the model proposed by Ouerghi *et. al*, with between 1-3 missing rows in the top layer per 4× unit. It is likely that for the higher coverage structures some dimerisation may occur on the surface, although this has not been included in the structures in Figure 4.17. Models m-n show a full over-layer with relaxation indicated by the arrows, based on the In-Si(111) model of Abukawa [101]. Bond counting for the models in Figure 4.17 are shown in Table 4.2. For the td(1×4) models, only the hetero double row model always obeys MEC, while for all other hetero row structures MEC is $\neq 0$ for all values of δ.

This would appear to make them less plausible, although without inclusion of surface dimerisation, it is rather hard to say.

On the basis of the modified electron counting, the hetero-adatom and hetero-vacancy models for the (2×2) reconstruction, and the hetero double row for the $td(1\times4)$ seem the most promising reconstructions as a result of their independence on δ. That the hetero-adatom and hetero-vacancy models have both been proposed by Ouerghi *et al.*, which to date seems the most convincing evidence for the surface structures, provides rather more confidence in this MEC. In order to more accurately determine the surface structures, more quantitative experimental techniques (such as STM, XPS, XRD) must be combined, supported by DFT calculations. The work presented in this chapter should provide a starting point for more detailed work.

Model	Description	A Dangling	B Dangling	A Dimer	B Dimer	Electron counting total	δ=3/4	Termination
Electron counting Excess/deficit		$+\delta$	-δ	-(2-2δ)	+(2-2δ)			
(2×2)								
(a)	Hetero-adatom	1(9)	1(3)	-	-	0	0	1/4 ML B
(b)	Homo-adatom	2(12)	-	3	-	8δ-6	0	5/4 ML A
(c)	Hetero-trimer	1(9)	3(9)	-	3	6-8δ	0	3/4 ML B
(d)	Homo-trimer	4(18)	-	6	-	16δ-12	0	7/4 ML A
(e)	Hetero-vacancy	3(3)	3(9)	-	-	0	0	3/4 ML B
(f)	Homo-vacancy	6(12)	-	9	-	22δ-18	-1.5	7/4 ML A
td(1×4)								
(g)	Hetero missing row	1(3)	3(9)	-	-	-2δ	-1.5	3/4 ML B
(h)	Homo missing row	4(12)	-	9	-	24δ-18	0	7/4 ML A
(i)	Hetero double row	2(6)	2(6)	-	-	0	0	2/4 ML B
(j)	Homo double row	4(12)	-	6	-	16δ-12	0	6/4 ML A
(k)	Hetero-adatom row	3(9)	1(3)	-	-	2δ	1.5	1/4 ML B
(l)	Homo-adatom row	4(12)	-	3	-	10δ-6	1.5	5/4 ML A
(m)	Hetero full layer relaxed	-	4(12)	-	-	-4δ	-3	1 ML B
(n)	Homo full layer relaxed	4(12)	-	12	-	28δ-24	-3	1 ML A

Table 4.2: Bond counting for the MnSb(0001) (2×2) and td(1×4) models in Figure 4.17 assuming the sp^3 hybridisation at the surface proposed by Nesbitt *et al.*. Numbers in parentheses indicate bond counting assuming ideal bulk termination (i.e. six bonds per atom). The results of modified electron counting for the models is shown, where δ is the number of electrons from the A atom in each A-B bond.

4.7 Summary

MnSb surfaces have demonstrated a rich variety of surface reconstructions, mediated by the deposition of individual Mn and Sb fluxes. The MnSb(0001) surface shows a (2×2) reconstruction observed by a number of other groups, which is the main growth phase, in addition to an Sb rich (1×1) which is believed to be a highly disordered surface due to excess Sb. At higher Sb depositions and low temperature, a td(1×4) reconstruction is observed which is likely to have a missing row(s) structure similar to that of the td(1×3) on MnAs(0001). At high Mn fluxes, a $(2\sqrt{3} \times 2\sqrt{3})$R30° is observed, although no structure is proposed. On the MnSb(1$\bar{1}$01) surface two new reconstructions have been observed, (1×2) and the dis(4×2) which is defined by the matrix notation

$$G = \begin{pmatrix} 3 & 1 \\ -1 & 2 \end{pmatrix}$$

The structure of the (1$\bar{1}$01) surface is highly complex, and so no structural models for either of these surfaces are presented.

With the exception of the (2×2) and (1×1), these reconstructions have not been reported elsewhere and so are of considerable interest. The main priority for future work should therefore be to obtain STM images of these surfaces, and use these to make more informed proposed structures. Following this, DFT will be carried out in order to asses these structural models, since the modified electron counting technique used here is unable to provide any firm conclusions.

Chapter 5

Heteroepitaxial growth of MnSb on InP(001)

5.1 Introduction

In Chapters 3 and 4, the heteroepitaxial growth of MnSb layers with both the expected ferromagnetic properties and high quality surfaces was demonstrated. It was also observed that the initial growth of MnSb(0001)/GaAs(111)B proceeded by 3D island nucleation followed by coalescence. This growth mode indicates the formation of defects at the interface which could hinder spin transport or injection [96, 97]. The growth mode on the GaAs(111)B substrate is dependent upon a number of factors including the lattice mismatch between MnSb and GaAs. A layer by layer growth mode is preferable for high quality interface formation, and this is considerably more likely for material combinations with lower lattice mismatch. For lattice matching to MnSb, a substrate is required with surface lattice parameters close to either a = 4.128 Å or c = 5.789 Å. Figure 5.1 shows the lattice parameters, a, and the <110> lattice spacing ($a/\sqrt{2}$) for a number of semiconductors (SC). The <110> lattice spacings are the most relevant since they form the primitive unit vectors for (001) and (111) surfaces. Also shown in Figure 5.1 are lattice mismatch contours between the <110> lattice spacing and the MnSb<$2\bar{1}\bar{1}0$> spacing. This gives the lattice matching in all directions for MnSb(0001)/SC(111) growth and in one direction for MnSb($1\bar{1}01$)/SC(001) and MnSb($1\bar{1}00$)/SC(001). From Figure 5.1, GaAs substrates are clearly non-ideal, with a -3.2% mismatch. With the exception of InP, all binary semiconductors shown have a mismatch greater than 2.5%. Based on Figure 5.1, InP appears the ideal choice for lattice matched growth of MnSb, with only a 0.5% mismatch between the InP<110> (a = 4.149 Å) and MnSb<$2\bar{1}\bar{1}0$> (a = 4.129 Å). Since InP and GaAs have the same

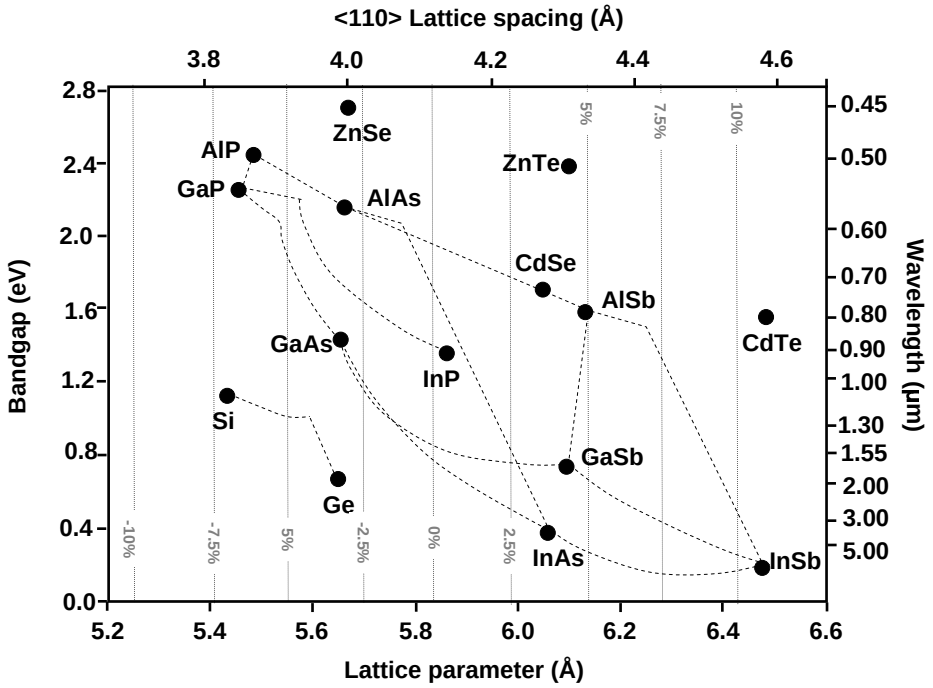

Figure 5.1: Lattice parameter and bandgap data for III-V semiconductors. Dashed lines between materials indicate intermediate data for ternary materials (or binary between Ge and Si). Vertical dotted lines indicate the lattice mismatch between the (110) lattice spacing and MnSb($2\bar{1}\bar{1}0$).

structure, the epitaxial orientations of MnSb grown on InP are expected to be similar to those observed on GaAs in Chapter 3. The InP(111) surface is therefore predicted to promote the MnSb(0001) growth orientation, while InP(001) substrates are likely to result in MnSb($1\bar{1}01$) as observed for MnSb/GaAs(001) or MnSb($1\bar{1}00$) orientation as observed for MnAs/GaAs(001).

In this chapter, the growth of MnSb/InP(001) is investigated. First, surface cleaning of InP(001) substrates is discussed, followed by the RHEED observations of MnSb/InP(001) grown at various temperatures and BEP ratios. During these observations, two growth phases were identified as MnSb and InSb (or $In_{1-x}Mn_xSb$). A number of compositional and thickness anomalies were observed during this study, and these are discussed in detail.

5.2 Surface preparation of InP

The preparation of clean InP surfaces has been the subject of a number of papers and is not as straightforward as cleaning GaAs (discussed in Section 3.2.1). Unlike GaAs, the native oxide of InP desorbs at 480°C [106], well above the incongruent sublimation temperature of 440°C [107]. This means that annealing alone cannot remove the oxides without causing the substrate to become non-stoichiometric. In addition, the large size mismatch between In and P atoms results in preferential sputtering of P during ion bombardment [108], leaving In rich features such as sputter cones on the surface. Typical methods for preparation of high quality InP surfaces involve high temperature annealing with a P_2 molecular beam incident on the surface, in order to maintain sample stoichiometry at high temperatures. The absence of a P effusion cell on the MBE-STM system makes this method impossible, and so preparation of InP surfaces sufficiently clean and well ordered for epitaxial growth is non-trivial. In order to develop a cleaning strategy for InP, three different methods were tested: high temperature annealing (sample A), chemical etching and sulphur passivation (sample B), and finally a modified IBA process (sample C). InP(001) samples (Wafer Technology Ltd., UK) 10 mm $\times$ 10 mm were used, attached to sample plates and loaded into the chamber in the usual fashion.

High temperature annealing (sample A) was based on the method of Bando *et al.* [107]. This method was reported to remove oxides at a temperature well below the oxide desorption temperature due to congruent desorption of the InP substrate at 380°C removing the surface contamination above. This method has been reported to produce a (2$\times$4) RHEED pattern, although the quality of the surface is reported to be highly temperature dependent. To test this cleaning protocol, the InP wafer was heated in 12.5°C increments, and the RHEED patterns observed. Figure 5.2a shows the RHEED pattern for as loaded sample A, with no visible RHEED streaks. As the temperature was increased to 250°C, a (1$\times$1) diffraction pattern was observed, with a high background. This indicates a reduction in the surface contamination, although the high background and lack of fractional order RHEED streaks indicates that the surface contamination is not fully removed. As the temperature was increased further, the background intensity reduced somewhat, but no fractional order streaks were observed at any time. Figure 5.2b shows the pattern obtained at 425°C, when the background was at its lowest. The

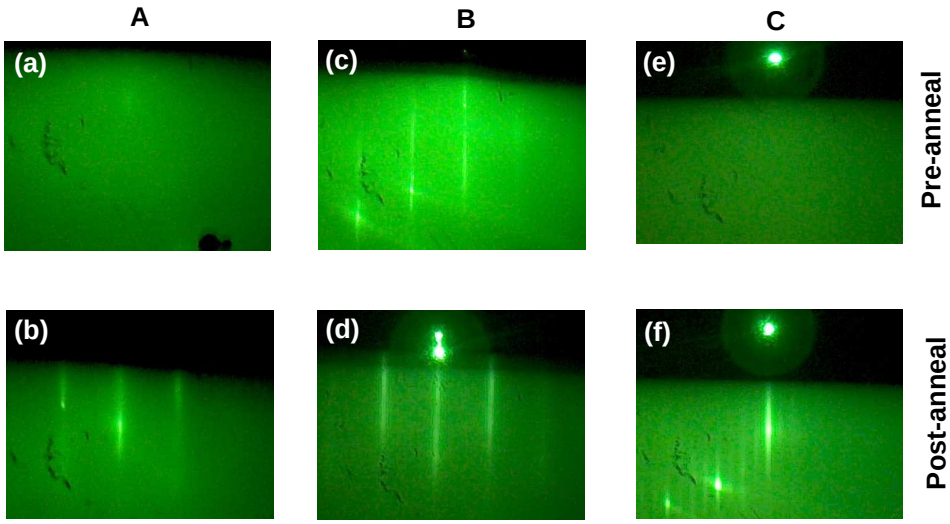

Figure 5.2: RHEED patterns for InP before and after annealing to 425°C for samples A (anneal only, panels a and b), B (sulphur passivated, panels c and d) and C (ion bombarding, panels e and f).

streak separation was consistent with InP <110>, but the absence of fractional order streaks indicates a considerable amount of contamination remaining on the surface. The sample was heated further, but the background intensity began to increase, consistent with deterioration of the surface quality due to incongruent desorption.

Sample B was etched in ammonium polysulphide ($(NH_4)_2S$) at room temperature for 10 minutes, then rinsed with acetone, propanol and de-ionised water before finally being dried with dry nitrogen. This follows the method of Chassé *et al.* [109]. Ammonium polysulphide is used to etch away the surface contamination layer, and passivate the substrate surface with sulphur. The sulphur passivation layer prevents further contamination during the transfer to UHV and can then be removed by annealing in vacuum. Figure 5.2c shows the as loaded sample. A comparison with panel a shows that the etch has indeed reduced the thick contamination layer, as integer order RHEED streaks are immediately apparent, although the background is high and no fractional order streaks are visible. The sample was then annealed at increasing temperatures. Although the RHEED streaks became visibly sharper and the background intensity reduced, only very faint fractional order streaks were observed which did not improve in

quality beyond that shown in panel d. Figure 5.2d shows the pattern at 425°C with very faint fractional order streaks.

Sample C was prepared by a modified IBA (ion bombarding and annealing) process. This was designed to combine high temperature annealing with a short ion bombarding step. This step was short to minimise any induced non-stoichiometry due to preferential sputtering of P. The sample was first degassed at 425°C for 1 hour to remove as many native oxides as possible and then ion bombarded for 2 minutes under standard operating conditions. Under these conditions, the estimated sputter yield (assuming one sputtered atom per arriving ion) is 0.04 mono-layers s^{-1}, and as such only $\sim$ 5 mono-layers of material should be removed. Finally, the sample was annealed to 425°C for a further 20 minutes. After ion bombarding, the RHEED pattern showed no features (Figure 5.2e), but following the final anneal stage a sharp (2×4) RHEED pattern was observed, shown in Figure 5.2f. The pattern shows sharp integer and fractional order streaks, with integer order streak spacing consistent with InP <110>.

All three cleaning methods reduce the contamination layer dramatically, allowing integer order RHEED streaks characteristic of the InP(001) surface to be observed. However, only with the modified IBA cycle were strong fractional order RHEED streaks obtained. This process has been used to prepare all subsequent InP samples. Although the ion bombarding process is expected to preferentially sputter P, the short duration of this step should maintain surface stoichiometry. In Section 5.4.3 the effect of preferential sputtering of the surface is discussed in more detail.

There has been a degree of controversy over the identity of the main InP(001) surface reconstruction, with (2×4) and (4×2) structures proposed. A number of papers follow the trend of (4×2) group III terminated (001) surface reconstructions demonstrated by InSb, GaAs and InAs [110, 111]. Generally, the (2×4) notation is accepted [112, 113, 114], along with the model of Schmidt *et al.* involving a one mixed dimer per unit cell aligned along the $[1\bar{1}0]$ upon a full In layer. This is the model assumed for this work.

5.3 Growth of MnSb/InP(001)

5.3.1 Experimental details

MnSb was grown on InP(001) wafers cleaned by the modified IBA protocol described in Section 5.2. After observing a sharp (2×4) RHEED pattern, the samples were cooled to the appropriate growth temperature T and allowed to equilibrate for 10 minutes. Growth was then initiated by opening the Mn and Sb shutters simultaneously. For all growth on InP(001) substrates, the Mn BEP was kept constant at 5×10^{-8} mbar and the Sb BEP altered systematically to obtain different BEP ratios ($J_{\mathrm{Sb/Mn}}$). The samples were all grown continuously for 90 minutes. RHEED patterns were observed during and after the growth to determine the growth layer quality and reconstructions over a large region of T vs. $J_{\mathrm{Sb/Mn}}$ phase space.

5.3.2 Growth surfaces and orientations

Figure 5.3 shows the RHEED patterns of MnSb/InP(001) samples grown under different temperatures and BEP ratios. Three distinct RHEED patterns were observed in different regions of phase space. These different phases were predominantly temperature dependent. At low temperatures ($<$290°C), RHEED streaks after growth were either diffuse or absent. The lack of distinguishable integer order streaks indicates a surface with little or no periodicity, and is associated with either non-epitaxial growth or a non-crystalline surface. These samples were subsequently annealed to high temperatures, but no RHEED features appeared. This indicates that the poor RHEED was not due to the presence of excess Sb on the surface similar to that observed for MnSb/GaAs(111)B surface at low temperatures (Section 3.2.2) as this could be removed by annealing. Instead, it is attributed to the high roughness of the surface.

As the substrate temperature is increased beyond 290°C, a second phase is observed. This is labelled phase A. Phase A is in fact associated with a range of RHEED patterns with common features, specifically unequal integer order streak spacing in perpendicular surface directions. An example of a phase A RHEED pattern is shown in Figure 5.4. This rather faint pattern displays unequal lattice spacings in the two perpendicular high symmetry directions. With the RHEED beam aligned along the 0° direction, the spacing is approximately matched to that of the InP substrate, while at

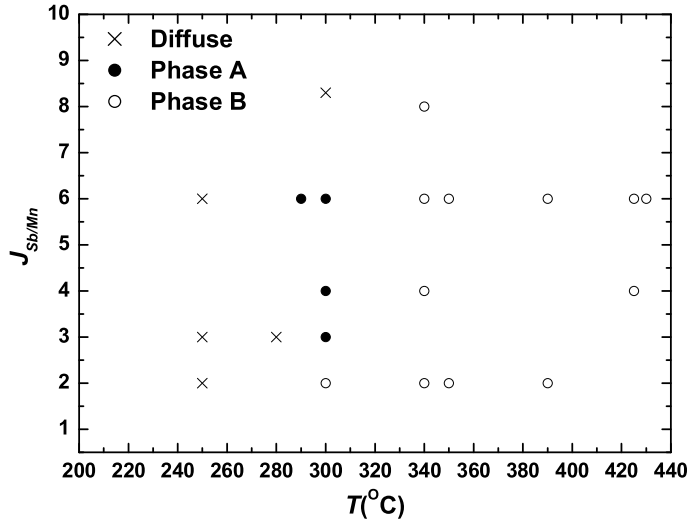

Figure 5.3: RHEED patterns for MnSb grown on InP(001) under varying growth conditions. Three regions are observed: a diffuse region with no strong RHEED features, Phase A with unequal perpendicular primitive unit vectors, and phase B with a strong (4×1) pattern.

90° the over-layer RHEED spacing is smaller than that of InP, corresponding to a larger surface mesh. RHEED intensity profiles for InP, and both phases are also shown in Figure 5.4. The RHEED spacings for phase A in the 0° and 90° directions are determined as 7.2 ± 0.2 mm and 4.5 ± 0.2 mm. All RHEED patterns associated with phase A exhibit this smaller RHEED spacing, although the patterns were often very faint and patterns in both high symmetry directions could not always be seen well. The RHEED patterns for phase A are reminiscent of those for MnSb($1\bar{1}01$)/GaAs(001) shown in Figure 3.15 which had integer order spacings of 15.6 ± 0.2 mm and 4.6 ± 0.2 mm respectively. In the 90° direction, they are very similar, with 2× periodicity and RHEED screen spacings within experimental error of one another. In the 0° direction, the spacings for the MnSb/InP(001) sample are almost half that of that for MnSb($1\bar{1}01$)/GaAs(001), although it is hard to determine unambiguously which are the integer order streaks for the sample grown on InP(001). The similarities indicate that while the surface plane is not necessarily ($1\bar{1}01$), it has a component in the c axis of the MnSb hexagonal structure, giving rise to the small RHEED streak spacing in the 90° direction. One possibility is the ($1\bar{1}00$) surface for which calculated RHEED spacings are 7.4 mm and 5.33 mm. If this was the growth plane, it would be very interesting as while the MnAs($1\bar{1}00$) surface

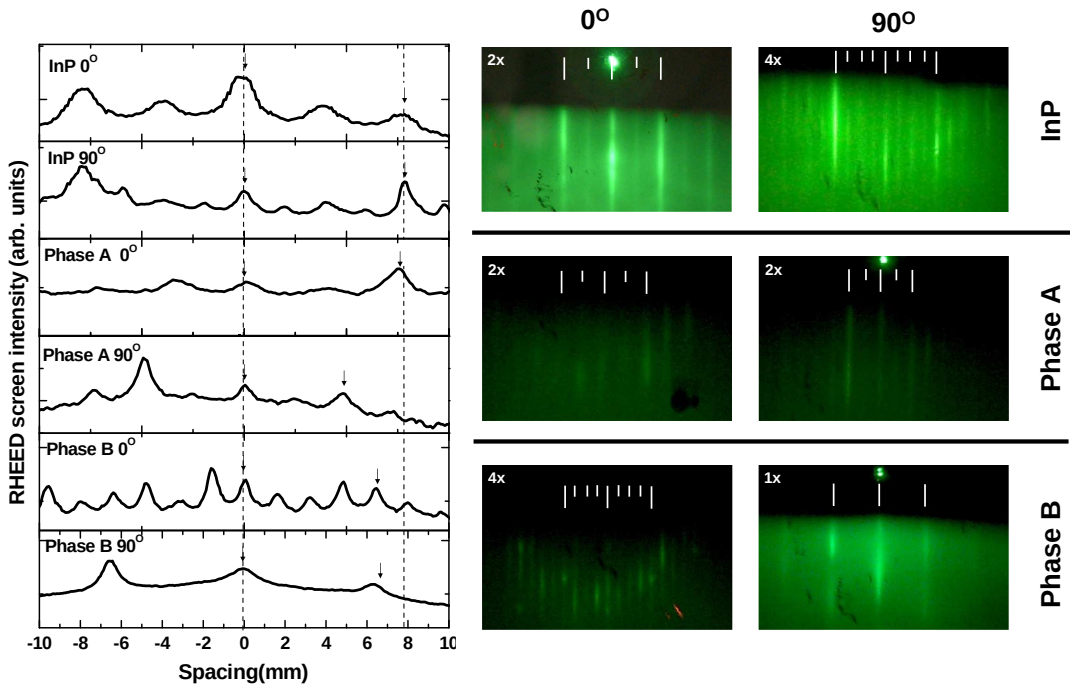

Figure 5.4: RHEED profiles and images for InP(001) (2×4) substrate and the two phases observed after growth. RHEED images are shown with the electron beam along two directions, 0° and 90° indicated in Figure 5.5. Integer order peaks in the RHEED profiles are indicated by arrows. Integer (fractional) order streaks in the RHEED images are indicated by long (short) lines.

has been grown on GaAs(001) (see Table 1.4), this surface has not been observed for MnSb to date. However, the high variation in RHEED pattern quality makes it rather hard to confirm the surface orientation.

At temperatures above 300°C, the third RHEED pattern, phase B is obtained. The RHEED patterns and profiles for this phase are shown in Figure 5.4. Phase B consistently displays a (4×1) reconstruction with a square unit cell and the 4× periodicity observed with the beam along 0° for all samples. This shows that the over-layer is epitaxial upon the InP substrate, and that the reconstruction should be labelled (4×1) by comparison to the InP (2×4). The RHEED streak spacings for phase B are smaller than those for the InP(001) substrate, indicating a larger surface lattice parameter of 4.5 ± 0.2 Å. From Figure 5.1, the only material with comparable lattice parameter and elemental content is InSb, which has a <110> spacing of 4.58 Å. The square surface mesh indicates that the InSb growth plane is the (001), which is supported by the (4×1) RHEED pattern. This reconstruction has similarities to the InSb(001) c(8×2)

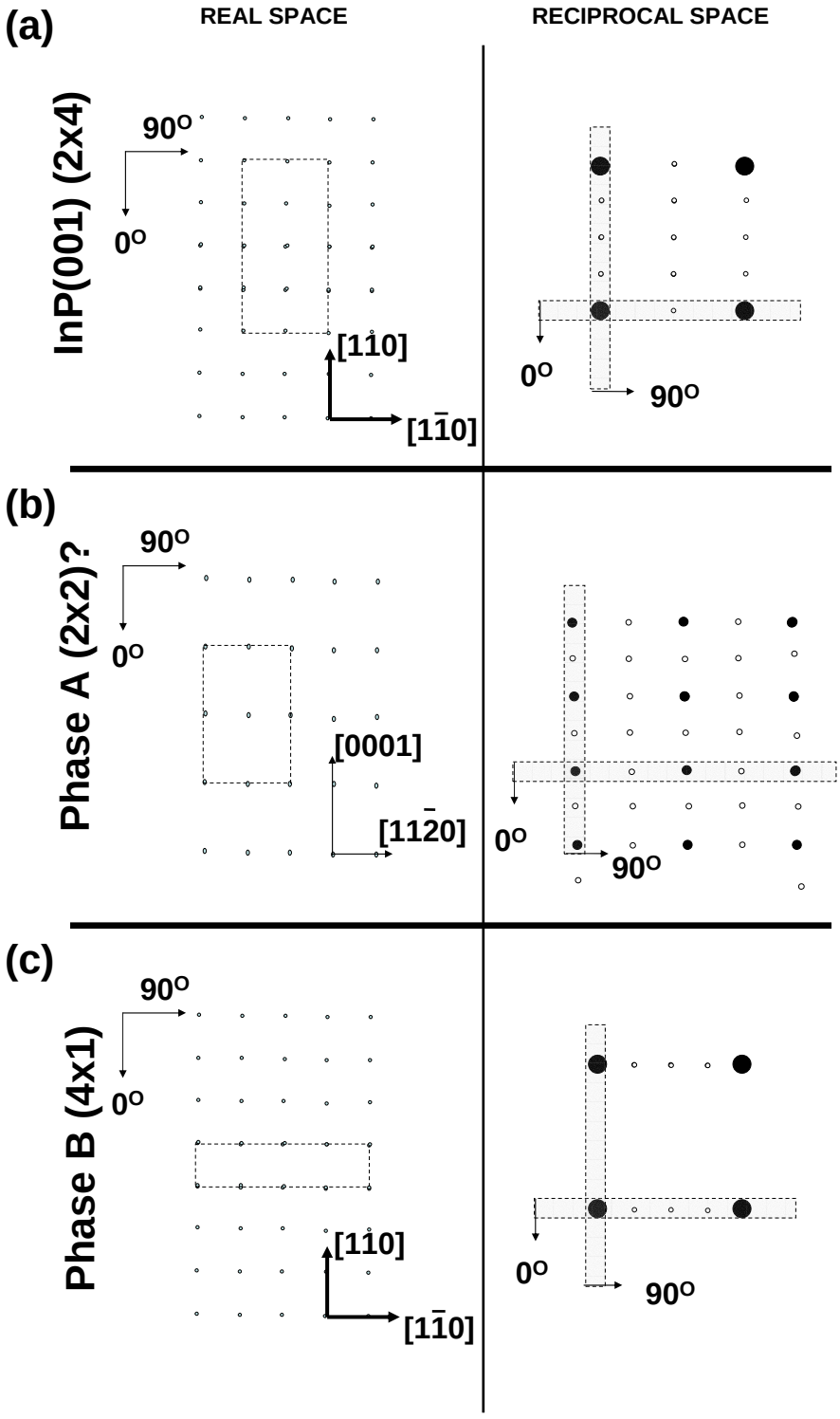

Figure 5.5: Epitaxial orientations of growth phases A and B on InP(001). The structure for phase A in panel b is assumed to be the MnSb(1$\bar{1}$00) orientation, although the streak spacings are not quite correct. Phase B is consistent with InSb(001). The panels indicate the relative orientations of real space (left) and reciprocal space (right). The shaded regions in the reciprocal space panels indicate the recording plane of the RHEED when the electron beam is in the direction indicated by the attached arrow. The solid (empty) circles indicate integer (fractional) order diffraction features. Directions are consistent across all the panels.

surface reconstruction [44], which also shows a 4× periodicity in the RHEED. In order to confirm this assignment, the (4×1) sample was annealed under Sb flux at 300°C. Under these conditions, InSb c(8×2) forms a c(4×4) reconstruction. No change in RHEED pattern was observed for the current phase, although this could due to excess In or Mn on the surface, resulting in further growth rather than the predicted reconstruction change. It is also possible that phase B is $In_{1-x}Mn_xSb$ ($x \ll 1$). As a result of the smaller atomic radius of Mn, this is expected to have a smaller lattice parameter than InSb, although the change is small (of the order of 0.05% [115]) and as such is not expected to be distinguishable by the RHEED measurements used here. The only reported reconstruction of $In_{1-x}Mn_xSb$ is (1×3) [116], although this was obtained at considerably lower temperature and Mn flux than those expected during the growth reported here.

The formation at high temperatures of a phase consistent with InSb(001) from RHEED is surprising, as although In is present in the substrate, none is expected in the growth layer. In order to further determine the processes involved in this multiple phase growth, the samples were removed from vacuum and studied using a range of microscopies.

5.4 Ex situ analysis of MnSb/InP(001) samples

5.4.1 Microscopy of MnSb/InP(001)

Optical microscopy

MnSb/InP(001) samples were first examined by optical microscopy, from which it was possible to separate the samples into two categories. The first set of samples were those grown at low BEP ratios ($J_{\mathrm{Sb/Mn}}$<3). These samples exhibited optically visible droplets on the surface, shown in Figure 5.6a. These varied in size from 100 nm to 100 μm droplets. EDX was used in order to obtain a compositional analysis of the droplets, which were found to be predominantly In. The quantity of material in these droplets could not be reliably estimated from the images as a result of the large size range of the droplets, although it is estimated to be approximately equivalent to tens of nm of layer growth. Figure 5.6b shows a typical optical image of the high BEP ratio ($J_{\mathrm{Sb/Mn}}$>3)

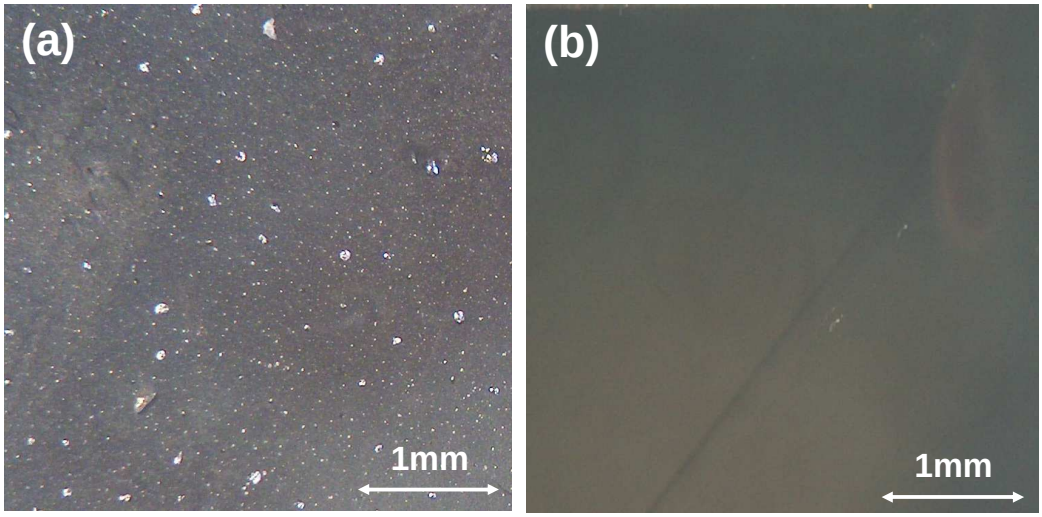

Figure 5.6: Optical pictures for samples grown under (a) low BEP ratio ($J_{\mathrm{Sb/Mn}} = 2$) and (b) high BEP ratio ($J_{\mathrm{Sb/Mn}} = 6$).

samples. These samples appear optically clean, with no indications of metallic droplets. However, the samples did not have the mirror finish characteristic of high quality single crystal films, and a dull grey appearance indicates roughness on smaller scales.

Plan view scanning electron microscopy

To study the morphology of growth layers in more detail, MnSb/InP(001) samples were imaged using plan view SEM. Figure 5.7 shows the surfaces obtained following growth at a variety of temperatures and two different BEP ratios, $J_{\mathrm{Sb/Mn}} = 6$ and $J_{\mathrm{Sb/Mn}} = 2$. Looking firstly at the $J_{\mathrm{Sb/Mn}} = 6$ samples, above 300°C multiple phase growth can be observed. Image c, corresponding to growth at 390°C displays two clearly different phases at distinct grey levels. The darker phase becomes more prevalent at lower growth temperatures (b) and is dominant at 300°C (a). The lighter phase appears as a matrix surrounding micron-sized crystallites of the darker phase and is prevalent at the highest growth temperature employed, 425°C (d). For samples grown with $J_{\mathrm{Sb/Mn}} = 2$, a similar pattern emerges, with the darker crystallites becoming fully overgrown by the lighter matrix at higher temperatures (panel g). It is interesting to note that at all temperatures, the coverage of the lighter matrix is greater for low BEP ratio samples. There is a temperature offset of approximately 90°C between surfaces of similar com-

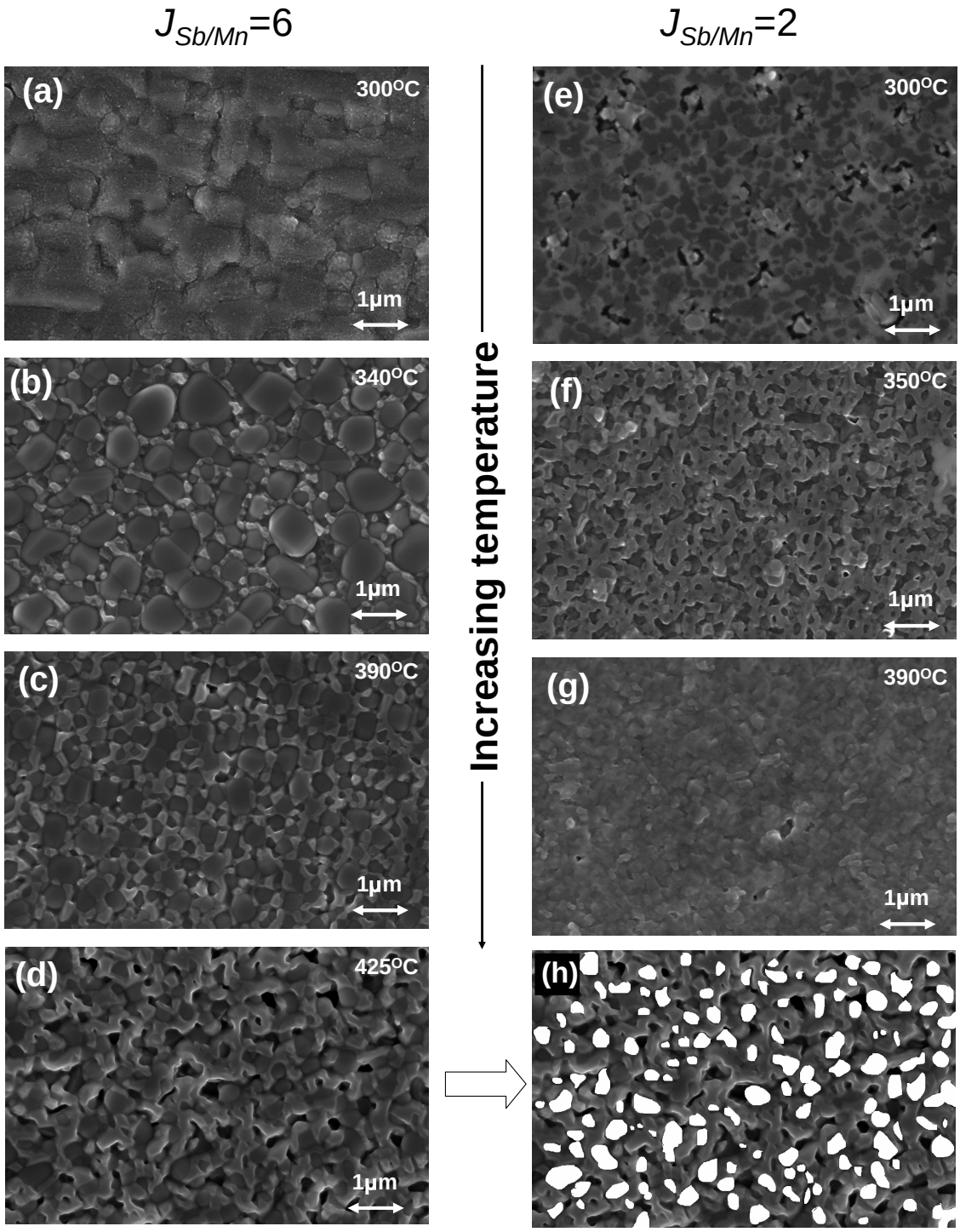

Figure 5.7: Plan view SEM images of MnSb over-layers grown at different temperatures and BEP ratios. Panels (a)-(d) are grown with BEP ratio $J_{\mathrm{Sb/Mn}} = 6$ and (e)-(g) at $J_{\mathrm{Sb/Mn}} = 2$. Panel h shows the painted version of panel d used to measure the coverage of phase B.

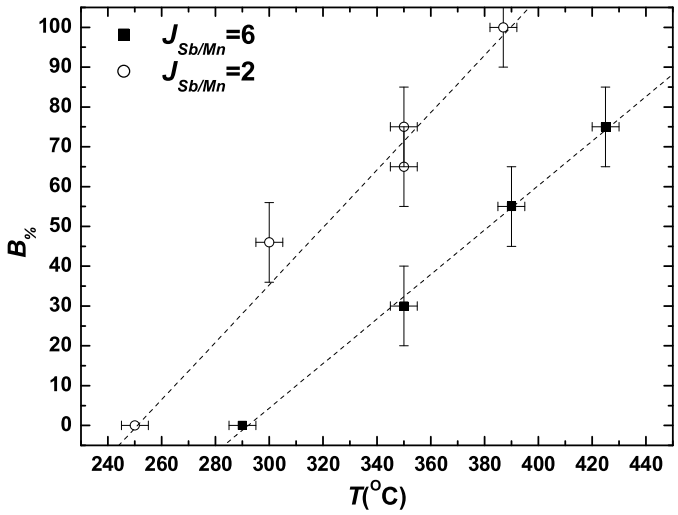

Figure 5.8: Surface coverage of phase B ($B_{\%}$) for samples grown at different substrate temperatures and BEP ratios determined from painted plan view SEM images and a threshold procedure.

positions for the $J_{\mathrm{Sb/Mn}} = 6$ and $J_{\mathrm{Sb/Mn}} = 2$ samples. As an example, panels c and e show similar coverages of the two phases, and crystallites of similar sizes. In the same fashion, panels d and g are comparable. Panel g shows a surface fully covered by the lighter matrix with no sign of the crystallites, which may be either buried or very small.

By comparison with the temperature dependence of the RHEED patterns, the darker crystallites are identified as phase A and the lighter matrix as phase B. From the SEM images it is apparent that phase B is generally flatter than the crystallites of phase A, and as such may be expected to give better RHEED patterns. The rounded shape of the crystallites could be the cause of the poor and inconsistent RHEED patterns obtained for phase A. From Figure 5.7a, it is evident that there are two preferential directions for the boundary between coalescing phase A crystallites. These directions are perpendicular to one another, and suggest orthogonal or nearly orthogonal crystallographic planes perpendicular to the growth direction. As with the RHEED observations, this is consistent with a MnSb($1\bar{1}00$) growth plane.

In order to accurately measure the coverage of the two growth phases, a threshold program was used to analyse the images in order to distinguish between the darker phase (phase A) and the lighter phase (phase B). Initial calculations with this program were hampered by the difficulties of choosing a suitable threshold to give a reasonable

representation of the coverage. Although the grey scale in the SEM images does contain some elemental information, it is primarily affected by the surface roughness and geometry. As a result of the low absolute contrast between the two phases and high roughness of the surface, further image processing "by eye" was required. The images were all manually altered before thresholding, by 'painting' areas of phase A, creating a large contrast between the two phases. This was found to produce more consistent and realistic coverage measurements. The coverage of phase B ($B_{\%}$) as a function of growth temperature is shown in Figure 5.8. A painted version of panel d is shown in panel h of Figure 5.7.

Figure 5.8 highlights the observation that for $J_{\mathrm{Sb/Mn}} = 2$ samples, phase B begins to dominate at a lower substrate temperature. The coverage of phase B for both sets of samples appears to increase linearly from 0% to 100% in a temperature range of $\sim$140°C. From the plan view SEM images, it is impossible to comment upon how the total quantities of the two phases vary with temperature, only on the relative amount visible on the surface. While it appears that phase B grows at the expense of phase A, it may be that the amount of phase A is constant, and increasing amounts of phase B at high temperature overgrow the crystallites.

Cross sectional scanning electron microscopy

In order to determine the amount of material in the growth layer, cross sectional SEM images were studied. The cross sectional SEM allows for the determination of the thickness of the growth layers in addition to details of the interface condition on nm scales. In Chapter 3, this technique has been used to observe MnSb/GaAs layer thickness, from which growth rates were determined. For the MnSb/InP(001) samples, layer thickness L has been quoted rather than growth rate, which would be a misleading term when two different growth processes are occurring simultaneously. Since all MnSb/InP(001) samples were grown for 90 minutes, the two terms are actually analogous. A typical cleaved edge of MnSb/GaAs(111)B is shown in Figure 5.9d. Figure 5.9a-c shows the cleaved edge for three MnSb/InP(001) samples grown at $J_{\mathrm{Sb/Mn}} = 6$, with the growth temperature increasing from 250-425°C. Panel a shows a layer of approximately 300nm, with no indications of multiple phases. From the plan view SEM images (Figure 5.7), this is identified as phase A. The interface region shows visible

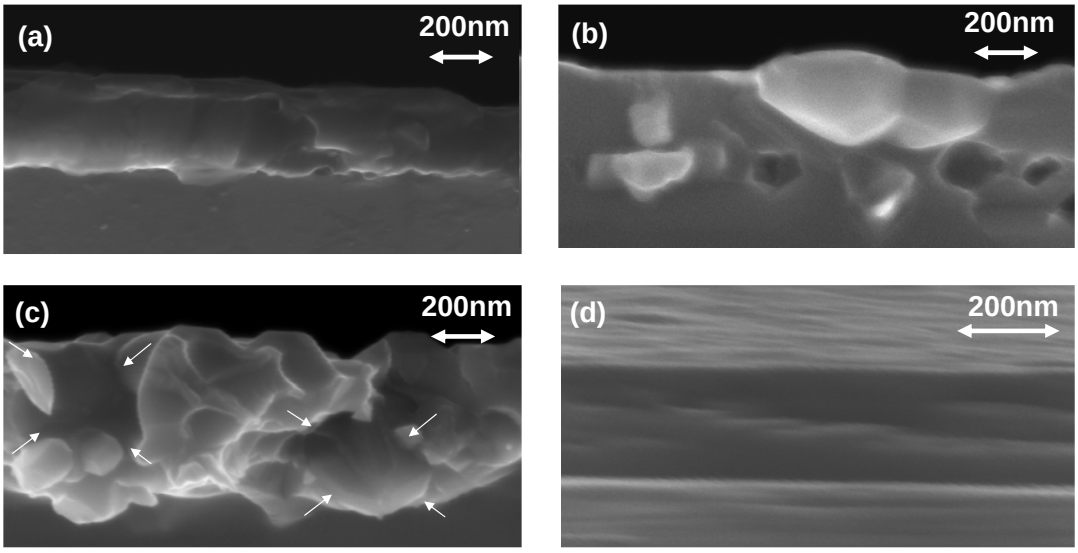

Figure 5.9: Cross section SEM images for MnSb samples grown on InP(001) with BEP ratio $J_{\mathrm{Sb/Mn}} = 6$ at substrate temperatures (a) 250°C (b) 340°C (c) 425°C. Panel d shows a typical MnSb over-layer grown on GaAs(001) at 300°C, $J_{\mathrm{Sb/Mn}} = 4$. The arrows in panel c indicate crystallites or voids where crystallites have been removed.

disruption compared to the sample grown on GaAs in panel d. The over-layer in panel b (grown at 340°C) is thicker and now shows two clearly different phases: the crystallites observed in Figure 5.7, in addition to the flatter, dark grey material surrounding it. These are identified as phases A and B respectively. There appear to be cavities in the lower sections of the growth layer, which are most likely caused by the removal of crystallites from the sample during the cleave. Panel c shows an even thicker layer grown at 425°C, with significantly different morphology to previous samples. The crystallites (phase A) or crevices indicating their removal are still observed in the growth layer (indicated by arrows), but are mostly overgrown by phase B, and the layer has a very rough interface. Panel d shows the cross sectional SEM images from a MnSb layer grown on GaAs(001) under similar growth conditions to panel a. The over-layer on GaAs has a sharp interface compared to all the layers grown on InP(001), indicating that the InP substrate is reacting with the growth material.

The over-layer thicknesses (L) for $J_{\mathrm{Sb/Mn}} = 2$ and $J_{\mathrm{Sb/Mn}} = 6$ samples grown at different temperatures, measured by cross sectional SEM are shown in Figure 5.10. The

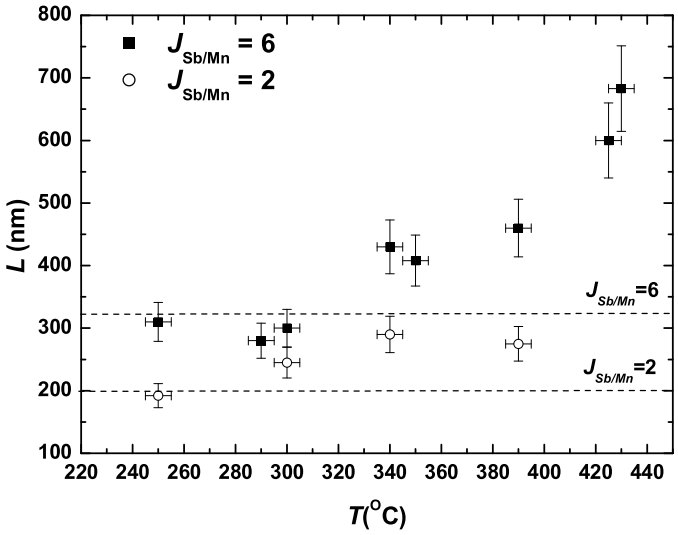

Figure 5.10: Growth layer thickness L for $J_{\mathrm{Sb/Mn}} = 2$ and $J_{\mathrm{Sb/Mn}} = 6$ as determined from cross sectional SEM. The dotted lines indicate the thickness expected from growth rates of MnSb/GaAs measured in Chapter 3.

cross sectional SEM images demonstrate that the growth layer is in excess of 180 nm for all samples, with no gaps. The dotted lines in Figure 5.10 shows the MnSb layer thickness predicted from growth rate studies carried out in Section 3.2.3. The layer thickness on GaAs(111)B was found to be independent of growth temperature at $J_{\mathrm{Sb/Mn}} = 8$, although this may not be accurate at lower BEP ratios. If there is any temperature dependence at lower BEP ratios, the growth rate is expected to decrease with increased temperature, as a result of the effective decrease in $J_{\mathrm{Sb/Mn}}$ due to increased Sb desorption (see Figure 3.7a). At low temperatures (100% phase A) the layer thicknesses grown on InP(001) agree fairly well with the predictions for both BEP ratios. As temperature is increased, the thickness for both BEP ratios increases, with the onset of this increase at 250°C and 300°C for $J_{\mathrm{Sb/Mn}} = 2$ and $J_{\mathrm{Sb/Mn}} = 6$ respectively. This onset appears to coincide with the initial appearance of phase B in the plan view SEM images (Figure 5.7). At low BEP ratios, over-layer thicknesses increases only a small amount, up to 300 nm and then plateaus. The thickness of $J_{\mathrm{Sb/Mn}} = 6$ samples increases to 700 nm at 425°C. For growth at $J_{\mathrm{Sb/Mn}} = 6$, the increase in over-layer thickness implies that phase B is forming in addition to phase A, while at low BEP ratios, the constant layer thickness after 300°C indicates competitive growth limited by Sb flux. This behaviour

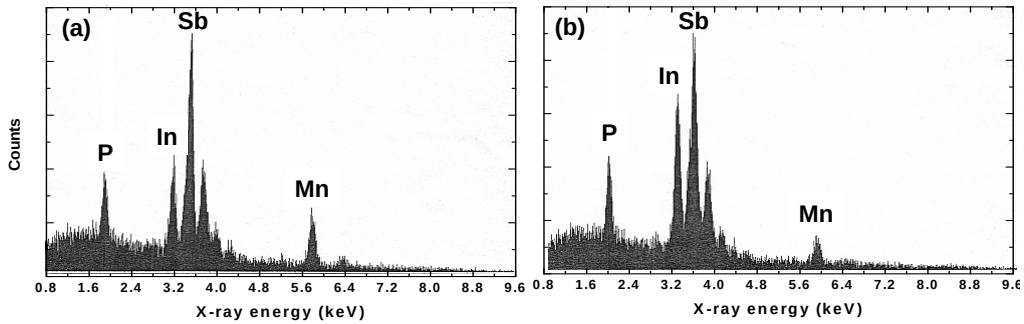

Figure 5.11: EDX spectra with the electron beam directed at (a) a dark grey crystallite (phase A) and (b) the light grey matrix (phase B).

is discussed in more detail in Section 5.4.3.

5.4.2 Chemical analysis of MnSb/InP(001)

Energy Dispersive Analysis of X-rays

While imaging the MnSb/InP(001) samples using the SEM, the energy dispersive analysis of X-rays (EDX) facility was used in order to begin identifying the two phases. The information gained by EDX on thin films is rather limited due to the large interaction volume ($\sim$ 600 nm in width) of the electron beam as described earlier (Section 1.4.5). This means that a large proportion of the signal obtained originates from the substrate. As a result, only semi-quantitative elemental information may be gained regarding the compositions of the two phases in the over-layer. Figure 5.11 shows spectra obtained for the same sample with the electron beam directed at the dark grey crystallites (phase A, Figure 5.11a) and the light grey matrix (phase B, Figure 5.11b). In, P, Mn and Sb are the only elements observed. Both In and P signals are observed for both phases, showing that the substrate is being detected as expected. Comparing the two spectra, two important differences are observed. The first is that the In peak increases in intensity by almost a factor of 2 between phase A and phase B. At the same time, the Mn peak halves in intensity. The Sb and P peak heights are approximately constant between the two phases. This behaviour was observed for all samples, and implies a Mn rich phase A and In rich phase B. In order to better determine the compositions of the two phases, the samples were studied using XPS.

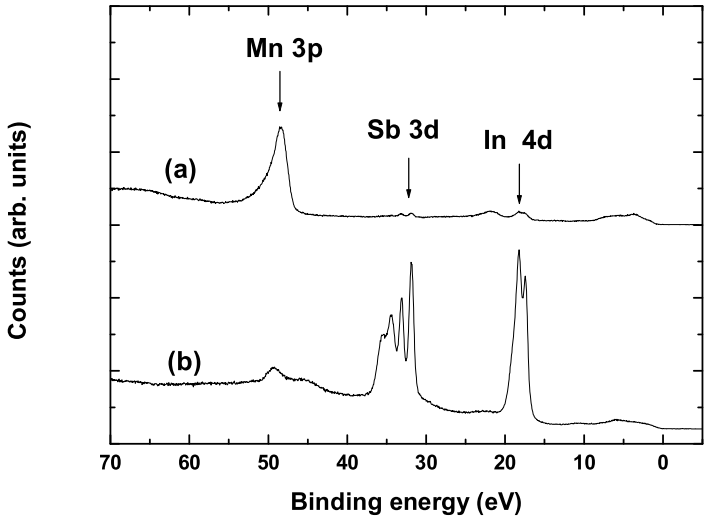

Figure 5.12: Raw XPS spectra for samples of (a) 100 % phase A ($J_{\mathrm{Sb/Mn}} = 2$, $T = 250$°C) and (b) 100 % phase B ($J_{\mathrm{Sb/Mn}} = 2$, $T = 380$°C).

X-ray Photoelectron spectroscopy

XPS was carried out using the VSW ESCA system at Warwick University and also the Scienta ESCA300 at the NCESS facility at Daresbury Laboratory, UK. As discussed in Section 2.7, the agreement for elemental peak ratio analysis is good between the two systems, and as such no distinction is made between the two data sets.

XPS has the advantage over EDX of only studying the top ∼4 nm of material and does not detect the substrate. However, as a consequence of this extreme surface specificity, the signal is dominated by the oxides and carbon on the surface due to contamination during transfer from the growth system to the XPS chamber. The assumption is made that the elemental ratios in this contamination layer are indicative of the populations in the surface region prior to contamination, and as such the O and C signals can effectively be ignored for the purpose of simple peak area analysis. This is a reasonable assumption since the sample has not been thermally treated after contamination and as such the diffusion length of the atoms will be low. The raw spectra for two samples grown at different substrate temperatures are shown in Figure 5.12. These samples correspond to $B_{\%} = 0$ and 100 respectively, and show the Mn 3p, Sb 4d and In 4d peaks. From this figure it is clear that phases A and B have distinctly different compositions, with phase A composed predominantly of Mn, and phase B mainly In and

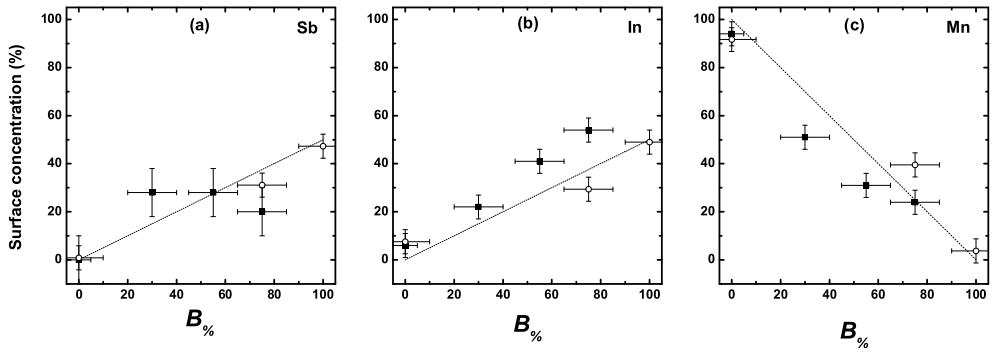

Figure 5.13: Relative surface concentrations of Sb, In and Mn as a function of area fraction of phase B for samples grown at $J_{\mathrm{Sb/Mn}} = 6$ (solid squares) and $J_{\mathrm{Sb/Mn}} = 2$ (open circles). These were determined from the Sb 3d, In 3d and Mn 2p XPS peak intensities. The dotted lines are linear extrapolations between the $B_{\%} = 0$ and 100 compositions.

Sb. In order to further characterise the samples, XPS spectra were obtained for samples grown under different conditions, and the relative concentrations of In, P, Mn and Sb were determined from the In 3d, P 2p, Mn 2p and Sb 3d peaks respectively. The signals were normalised according to atomic sensitivity and photoelectron mean free path [92] as described in Section 1.4.4.

The relative XPS signals for Mn, In and Sb have been plotted in Figure 5.13 against the appropriate value of $B_{\%}$ for samples grown with $J_{\mathrm{Sb/Mn}} = 6$ (solid squares) and $J_{\mathrm{Sb/Mn}} = 2$ (open circles). For XPS of a single phase, the ratios of the peaks areas indicate concentrations and depth profiles of the different elements. For mixed phases, it is expected that the peak ratios will predominantly vary with the relative coverage of the different phases. This will be true assuming the phase domains are considerably smaller than the analysis region of the XPS system (several mm^2), which is an accurate assumption for domains of ~ 1 μm^2 shown in Figure 5.7.

For a sample of two mixed phases A and B, the area of elemental peak p, A^p_{AB} will depend upon the signal expected for that peak in single phase samples, A^p_{A}, A^p_{B} as described by Equation 5.1

$$A^p_{\mathrm{AB}} = (100 - B_{\%})A^p_{\mathrm{A}} + B_{\%}A^p_{\mathrm{B}} \tag{5.1}$$

Here the percentage surface coverage of phase B, denoted by $B_{\%}$, is determined from the plan view SEM measurements, the results for which are shown in Figure 5.8. Lines

in Figure 5.13 show the predictions from this linear model using values for A^p_{A} and A^p_{B} taken from $B_{\%} = 0$ (Mn rich) and 100 (In + Sb) samples respectively.

The agreement between the linear model and the experimental data is generally very good, with all samples showing the correct gradient for both high and low BEP ratio samples. This shows that the composition is indeed varying with the coverage of the two phases, which in turn indicates that the phases have consistent compositions for all growth temperatures. The compositions of the two phases are identified as follows. Phase B shows a ratio of approximately 1:1, In:Sb, which is consistent with the previous assignment of InSb from the RHEED patterns. The presence of small amounts of Mn may indicate the $\mathrm{In}_{1-x}\mathrm{Mn}_x\mathrm{Sb}$ composition, although the Mn could equally be metallic Mn on the surface or small regions of phase A. It is difficult to distinguish the two Mn environments by XPS chemical shifts due to the difficulty in peak fitting Mn spectra [35]. The surface of phase A is highly Mn rich. This Mn rich MnSb surface has also been observed for Sb poor growth of MnSb/GaAs(111)B in Section 3.2.3 and so assignment of phase A as MnSb is reasonable.

5.4.3 Growth modes and phase compositions

Epitaxial growth of MnSb on InP(001) has proven to be rather difficult compared to the growth on GaAs. Over a large range of growth temperatures and BEP ratios multiple phase growth has been observed. At high temperatures, an In rich phase characterised by (4×1) RHEED patterns becomes dominant. From XPS and RHEED this phase, referred throughout this chapter as phase B, has been identified as InSb or $\mathrm{In}_{1-x}\mathrm{Mn}_x\mathrm{Sb}$ ($x \ll 1$). This presents the question of how In can be present in the thick ($>$ 100 nm) growth layers when only Mn and Sb molecular beams are incident on the sample. A second unusual feature of the MnSb/InP(001) growth is the behaviour of the sample thickness as a function of growth temperature. At high BEP ratios and temperatures, the conditions favorable for phase B formation, the sample thickness increases by more than a factor of 2 in a temperature range of only 125°C. In this section, these two anomalies are considered.

Compositional anomalies

There are several possible sources of In in the growth layer. Indium originating from the MBE chamber (which has an In effusion cell) has been ruled out by the absence of an In signal in XPS or EDX for MnSb/GaAs samples grown under identical conditions (Chapter 3). This also rules out In contamination from the XPS systems, the In solder (and eutectic solution) used to attach the sample wafers to the sample plates and any of the cleaning processes utilised. The source of the In in the growth layer can therefore only be attributed to the InP substrate. The simplest cause is that the XPS is detecting part of the substrate either due to gaps in the over-layer or analysis of an edge of the sample. These effects are ruled out by the absence of a P 2p signal at 135 eV in the XPS spectrum in addition to the thick continuous over-layers observed by cross sectional SEM. The In must therefore be diffusing out of the InP substrate, and becoming incorporated in the growth layer. This process will inevitably be thermally activated, which is consistent with the prevalence of the In rich phase B at high temperatures. Table 5.1 shows the enthalpies of formation for various materials of interest.

Material	ΔH_{f} (kJ/mole)	Ref.
MnSb	-35	[117]
MnIn	-11	[117]
InSb	-30.5	[118]
InP	-88.7	[118]

Table 5.1: Enthalpies of formation for various compounds

The first point to note is the high (negative) enthalpy of formation of InP, indicating a thermodynamically stable crystal. It is surprising therefore that the InP appears to deteriorate during the MnSb growth. In order to examine the mechanism for the formation of InSb, an InP(001) substrate cleaned by the modified IBA process (Section 5.2) was annealed at 400°C under an Sb flux for 90 minutes. The RHEED was observed and the resulting surface examined by SEM. Immediately after growth was initialised the (2×4) RHEED pattern disappeared, producing weak integer order streaks in both high symmetry directions. After a few seconds the RHEED became spotty, indicating transmission diffraction through small crystallites as illustrated in Figure 1.6.

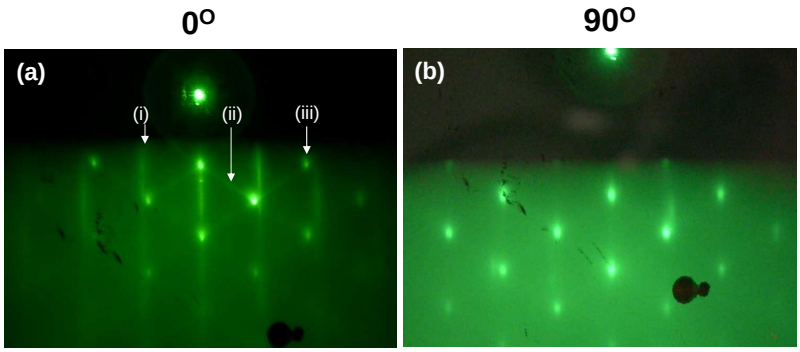

Figure 5.14: RHEED patterns obtained from InP(001) surfaces after 90 minutes annealing under an Sb flux.

Following the initial change to a transmission diffraction pattern, no further changes were observed during the exposure to Sb. The RHEED patterns in the two perpendicular high symmetry directions are shown in Figure 5.14, and show three distinct features. The streaks labelled i have the largest spacings, and correspond to a lattice spacing of 4.2 $\pm$ 0.2 Å, agreeing well with the InP primitive unit mesh spacing (4.149 Å). Feature ii shows streaks tilted at approximately $\pm 56^{\circ}$ to vertical indicating crystalline facets, while feature iii shows the spotty transmission diffraction. The facets and spots have the same periodicity, indicating a lattice spacing of 4.5 $\pm$ 0.2 Å, matching well with the $<110>$ spacing of InSb (4.58 Å). The facets were far more pronounced observed with the beam along the 0° direction.

The sample was examined using SEM, and is shown in Figure 5.15a. The surface was mostly flat and featureless with a small number of 3D islands ($\leq$250nm in all dimensions). The islands were rectangular in shape with the edges aligned along the $<110>$ and $<1\bar{1}0>$. There appears to be a preferential direction for the long axis of the rectangles along the [110] direction, corresponding to the 0° direction from the RHEED images. The inset of Figure 5.15a shows an enlarged image of one of the 3D islands. This shows distinct facets which have been determined as $\{111\}$ facets from the angles of the streaks in the RHEED (feature ii, Figure 5.14). These observations agree with those of Ferrer *et al.* [119] during heteroepitaxial growth of InSb 3D islands on InP(001). Figure 5.15b shows the cross sectional SEM image of the sample, which shows a surface with apparent undulations of the order of 10 nm. These are very small compared to the disruption regions in Figure 5.9, and are typical of an InP cleave. Atomically sharp edges are never observed using this simple cleave technique because of irregularities and

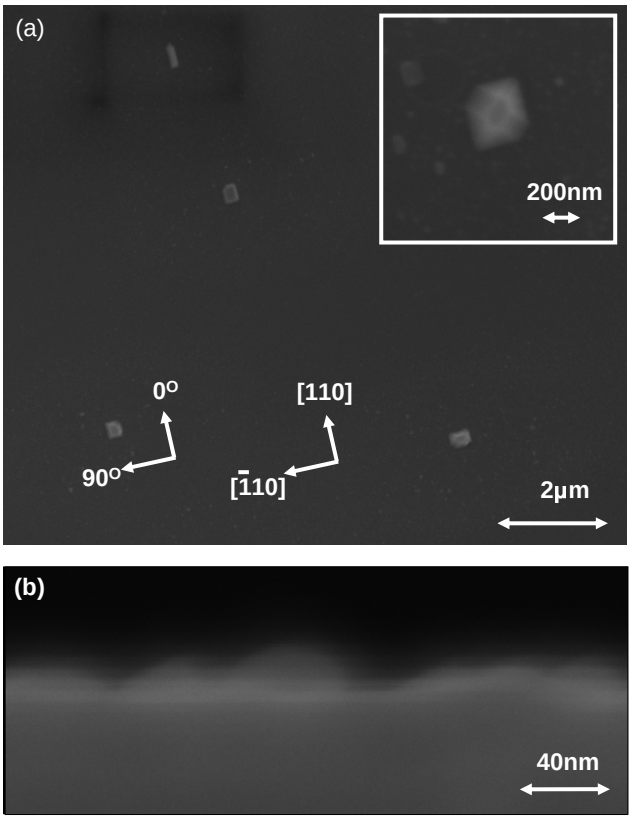

Figure 5.15: SEM obtained from InP(001) surfaces after 90 minutes annealing under an Sb flux. (a) plan view and (b) cross sectional view.

debris remaining at the corner defined by the intersection of {110} and {001} planes. Whatever the origin of the apparent undulations, there is clearly no development of large (∼100 nm) crystallites and no large-scale disruption of the sub-surface region.

Due to the low number density and size of the InSb islands, it is unlikely that any large scale In out-diffusion has occurred and certainly not to the extent observed during MnSb growth for an equivalent time at 400°C. Instead, these islands are probably formed by the reaction of Sb with residual In on the surface as a result of the preferential sputtering during the cleaning process. The low number density and size of these islands provides an indication of the disruption of the surface caused by the non-ideal modified IBA cleaning procedure. There is clearly some preferential sputtering, but only a small amount. Shortening of the ion bombarding time in the sample preparation stage may reduce residual In on the surface further.

The amount of In present on the surfaces is not sufficient for the formation

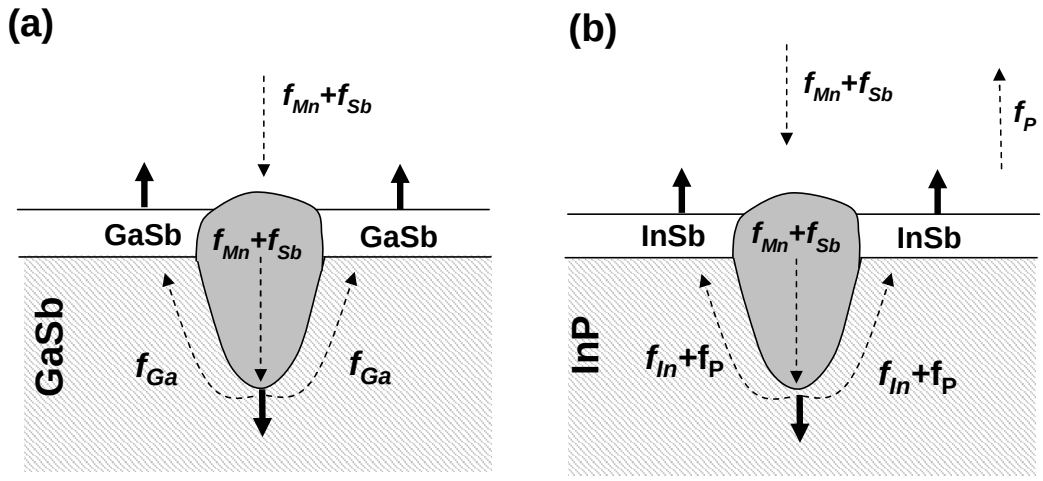

Figure 5.16: Model for endotaxy. (a) MnSb/GaSb proposed by Braun *et al.* [32] and (b) MnSb/InP using the same model. Dashed arrows indicate elemental fluxes and solid arrows the direction of a growth front. The dark crystallites in both cases are MnSb.

of the thick regions of InSb observed in the mixed phase MnSb/InP(001) samples. It is therefore apparent that the presence of In in the growth layer is not caused by Sb alone via a group V exchange reaction [120]. A recent study of InP(001) exposed to trimethylantimony in a metalorganic vapor phase epitaxy reactor [121] confirms this. Even at 600°C, a surface layer of InSb of maximum average thickness of only 7 Å was developed, with surface roughening of root mean square amplitude $<$4 Å.

The behaviour of the MnSb/InP(001) samples is in many ways analogous to the endotaxial growth of MnSb/GaAs(001), reported by Braun *et al.* [32]. In this study, well oriented MnSb crystallites grow *into* the surface. The flux of displaced Ga from the substrate diffuses to the surface and grows further GaSb surrounding the MnSb crystallites. This process is illustrated in Figure 5.16a. A similar model may be applied to MnSb/InP, although this system will be inherently more complex as there are no common elements between the over-layer and substrate. The model of Braun has been extended to the InP substrate in Figure 5.16b. In this model, In and P are displaced from the substrate by the growth of MnSb into the substrate. In can then react with the incoming Sb flux, while P desorbs into the vacuum. Formation of MnP would also

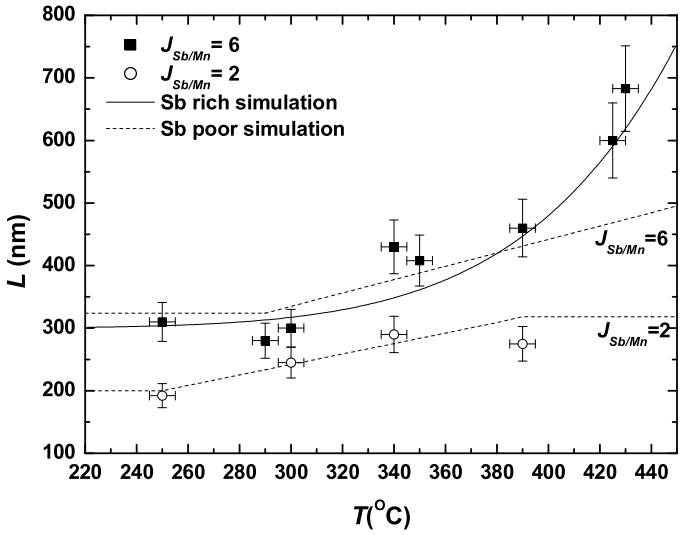

Figure 5.17: Growth layer thickness L for $J_{\mathrm{Sb/Mn}} = 2$ and $J_{\mathrm{Sb/Mn}} = 6$ as determined from cross sectional SEM. The dotted lines indicate the Sb poor simulation and the solid line an Sb rich simulation fitted to the $J_{\mathrm{Sb/Mn}} = 6$ data.

seem possible, although there is no evidence of this in the experiments. While this model is speculative, it matches the features in the cross sectional SEM (Figure 5.9), and accounts for the presence of In in the growth layer.

Thickness anomalies

The second anomalous feature of the InP growth is the increase in layer thickness with temperature for both $J_{\mathrm{Sb/Mn}} = 2$ and $J_{\mathrm{Sb/Mn}} = 6$ samples, with the behaviour more exaggerated for the high BEP ratio samples. At low temperatures the sample thickness for both BEP ratios agrees well with the growth rate found experimentally in Section 3.2.3. Both show a slight increase in thickness with temperature, the onset of which occurs at the same time as the initial observation of phase B in the plan view SEM. The $J_{\mathrm{Sb/Mn}} = 6$ samples then continue to increase in thickness while the $J_{\mathrm{Sb/Mn}} = 2$ sample thickness plateaus.

It has already been concluded that two growth phases occur at higher growth temperatures, namely InSb and MnSb. It is therefore reasonable to define an In flux (f_{In}) from the substrate, in addition to fluxes of Mn (f_{Mn}) and Sb (f_{Sb}) from the effusion cells. The growth may then be separated into two different growth regimes depending

upon the relative fluxes. Since Sb combines with both In and Mn, the two regimes are: the Sb poor regime ($f_{\mathrm{Mn}} + f_{\mathrm{In}} > f_{\mathrm{Sb}}$) in which InSb and MnSb grow competitively, and the Sb rich regime ($f_{\mathrm{Mn}} + f_{\mathrm{In}} < f_{\mathrm{Sb}}$) in which there is sufficient Sb to combine with both In and Mn.

Under the Sb poor conditions, the thickness of the growth layer is predicted to only depend upon f_{Sb}, and naively expected to be constant with increased temperature. While it is true that the quantity of material in the growth layer will be independent of temperature in the Sb poor regime, the actual thickness of the layer depends upon the volume per formula unit (V) of the phase. MnSb and InSb have values of V_{MnSb} = 42.7 $\mathring{A}^3$ and V_{InSb} = 68.0 $\mathring{A}^3$. The thickness $L_{\mathrm{Sb\ poor}}$ of the growth layer in the Sb poor regime is therefore expected to vary as

$$L_{\mathrm{Sb\ poor}} \sim N(B_{\%}V_{\mathrm{InSb}} + (100 - B_{\%})V_{\mathrm{MnSb}}) \tag{5.2}$$

Here N is the number of atoms of Sb deposited (a constant which can be determined from the layer thickness at $B_{\%} = 0$). $B_{\%}$ is found experimentally from the linear fit to the SEM coverage data in Figure 5.8. A caveat to this is that the surface coverage of phase B may not accurately represent the volume percentage of phase B in the layer. For the purpose of this simple model this difference is disregarded. Sb poor models for $J_{\mathrm{Sb/Mn}} = 2$ and 6 are indicated in Figure 5.17 by dashed lines. For $J_{\mathrm{Sb/Mn}} = 2$, the simulation shows good agreement with the experimental data. The observation of metallic droplets on the surface is also consistent with an Sb poor model, since excess Mn or In would remain on the surface, with no Sb to react with. The behaviour indicates that InSb is formed preferentially to MnSb, although this is not an obvious result from the enthalpies of formation shown in Table 5.1. However, the enthalpies are very similar for the two materials and therefore other effects may dominate. For the $J_{\mathrm{Sb/Mn}} = 6$ samples, the agreement is poor. At lower temperatures the simulation appears reasonable, but at the highest temperature, the thickness of the samples are almost a factor of 2 greater than the value from the model. This indicates that the Sb poor model is not accurate for the $J_{\mathrm{Sb/Mn}} = 6$ samples. This is confirmed by the absence of metallic droplets on the surface for samples grown at higher temperatures.

Under Sb rich growth it is possible for both InSb and MnSb phases to grow simultaneously without competition. The layer thickness is now dependent only upon

the cation flux. While the Mn flux is constant, the effective In flux from the substrate depends on disruption of the InP lattice (possibly due to endotaxial growth of MnSb into the InP substrate) and migration of In atoms to the surface. The processes involved are likely to be rather complex. However, if the rate limiting process is thermally activated (as indicated by the increased InSb formation at higher temperatures) then the In flux may be expressed by a single effective activation enthalpy ΔH_{eff}.

$$f_{\mathrm{In}} = A\exp\left(\frac{-\Delta H_{\mathrm{eff}}}{RT}\right) \tag{5.3}$$

in which A is a constant, and the other symbols have their usual meaning. The layer thickness, of the form $L \sim f_{\mathrm{Mn}} + f_{\mathrm{In}}$ then takes the following temperature dependent form.

$$L_{\mathrm{Sbrich}} \sim V_{\mathrm{MnSb}} f_{\mathrm{Mn}} + V_{\mathrm{InSb}} A\exp\left(\frac{-\Delta H_{\mathrm{eff}}}{RT}\right) \tag{5.4}$$

This Sb rich equation has been fitted to the $J_{\mathrm{Sb/Mn}} = 6$ experimental data, and is shown in Figure 5.17 by a solid line. The fit is better than that for the Sb poor simulation, but still does not fit the data particularly well. Experimentally obtained values for ΔH_{eff} were difficult to obtain accurately, and ranged from 40 to 70 kJ mol^{-1}. These values are all less than the enthalpy of formation of InP (88 kJ mol^{-1}), which again implies that the MnSb growth or Mn flux is somehow catalyzing the break down of InP. The behaviour of the high BEP ratio samples matches the broad features of this Sb rich regime, although the evidence from the growth of GaAs(111)B was that $J_{\mathrm{Sb/Mn}} = 6$ is only just in the Sb rich growth regime.

5.5 Summary

Growth of MnSb/InP(001) has been investigated at a range of BEP ratios and growth temperatures. Multiple phase growth was observed at temperatures greater than 300°C. The low temperature phase (phase A) has been identified as MnSb, with a rectangular surface structure indicating a growth plane such as $(1\bar{1}00)$. XPS shows that the MnSb is highly Mn rich at the surface, which is consistent with the Sb poor growth of MnSb on GaAs(111)B from Chapter 3. At higher temperatures, the second phase (phase B) was identified as InSb or $\mathrm{In}_{1-x}\mathrm{Mn}_x\mathrm{Sb}$ with $x \ll 1$. This phase was characterised by a consistent (4×1) RHEED pattern and approximately 1:1 ratio of In

and Sb at the surface determined from XPS spectra. The presence of this second phase was observed in plan view SEM images, and the sample thickness directly observed by cross sectional SEM. The layer thickness was found to depend upon the growth regime: either Sb limited with changing volume effects under Sb poor growth conditions ($J_{\mathrm{Sb/Mn}} = 2$), or Mn and In limited under Sb rich growth conditions ($J_{\mathrm{Sb/Mn}} = 6$). In all cases the presence of In is attributed to thermally activated In out-diffusion from the InP substrate, possibly due to endotaxial growth of MnSb. This disruption of the InP substrate is observed to result in interfacial roughness in excess of 50 nm for all growth conditions.

These results have considerable implications for lattice matched growth of MnSb/InP(001). Although the reactivity of MnSb with the substrate is reduced at temperatures of $\sim$ 300°C, some reaction is still apparent from the rough interface. Growth at even lower temperatures appears to result in poor quality over-layers. There are a number of ways in which this reactivity may be prevented, such as multi-stage growth (i.e. low temperature buffer layer, then high temperature growth) or substrate passivation (i.e. by sulphur). These processes have not been investigated to date.

Chapter 6

Conclusions and future work

6.1 Overview

In this thesis a range of in situ and ex situ techniques have been used to optimise and study MnSb layers grown by MBE on a variety of III-V substrates. As the first project on a newly commissioned MBE-STM system, Chapter 2 concerns the tests and calibrations carried out in order to assess the capabilities and limitations of the system. The effusion cell BEPs were found to be highly controllable, stable and sufficiently constant across the samples for uniform growth. The cells were successfully used for homoepitaxial growth of InSb (001), (111)A and (111)B surfaces, and reconstruction maps for these substrates were obtained. Determination of surface periodicity and lattice parameters were demonstrated by measurement of the integer order RHEED streak spacings and this process optimised, allowing for in-plane lattice parameter determination to an accuracy of ± 0.2 Å.

Chapter 3 reports the growth of MnSb/GaAs, and represents the first heteroepitaxy study of MnSb using the MBE-STM system. The GaAs(111)B substrate was investigated as a result of its structural similarity with the hexagonal MnSb(0001) surface, although the high lattice mismatch of -3.2% means that this combination is not ideal for high quality interface formation. The observation of the surface structure by RHEED was used in addition to growth rate measurements to choose a set of standard conditions corresponding to Mn limited growth with a repeatable, sharp (2×2) surface reconstruction. These conditions resulted in a growth orientation of MnSb(0001)/GaAs(111)B. This orientation has been confirmed using XRD, and the expected ferromagnetic and metallic properties of the over-layers have been observed using magnetometery and XPS respectively. A study using RHEED and STM of the initial growth mode for MnSb/GaAs(111)B has indicated that growth begins by the nucleation and then coalescence of flat topped

MnSb islands. The heteroepitaxial growth of MnSb on GaAs(001) has also been studied, and the growth orientation determined to be MnSb($1\bar{1}01$)/GaAs(001) from the RHEED images.

Surfaces of MnSb are rather different from those of III-V semiconductors, and have been studied in Chapter 4 by consideration of idealised bulk terminated MnSb, together with experimental STM images of MnSb surfaces. These studies demonstrated that MnSb(0001) surfaces are terminated by only one element, separated by MnSb mono-layer steps, although there are indications that alternating terraces may have different bonding orientations rotated by 60°. On the MnSb(0001) surface, a range of surface reconstructions are observed as a function of Mn or Sb deposition and substrate temperature. From Mn rich to Sb rich, these are: ($\sqrt{3} \times \sqrt{3}$)R30°, ($2\sqrt{3}$×2 $\sqrt{3}$)R30°, (2×2), (1×1) and triple domain (1×4), of which only the (2×2) and (1×1) have been reported in the literature for MnSb or MnAs. A modified electron counting rule has been applied to a number of model structures for MnSb(0001) (2×2) and triple domain (1×4), and a number of more probable surface reconstructions indicated. The ($1\bar{1}01$) surface is considerably more complex, and comparisons of the idealised bulk terminations and STM images of the ($1\bar{1}01$) surface were rather inconclusive. This surface demonstrated two previously unreported reconstructions. These were a (1×2) and a distorted (4×2). The distorted (4×2) reconstruction is approximately the size of a (4×2), but rotated and distorted slightly.

In Chapter 5, a third substrate was investigated. InP is closely lattice matched to MnSb, and as such is expected to be preferable to GaAs for the formation of high quality interfaces with MnSb. Growth of MnSb/InP(001) over a range of conditions was observed to result in multiple phase formation in the over-layer. At high temperatures, $In_{1-x}Mn_xSb$(001) ($x \ll 1$) formed preferentially to MnSb as a result of In diffusion from the substrate. At lower temperatures, MnSb was formed, although the surfaces were rough, and RHEED patterns were faint and difficult to interpret. There were indications that the growth orientation was MnSb($1\bar{1}00$)/InP(001), although this was hard to confirm due to the poor quality RHEED patterns. The formation of $In_{1-x}Mn_xSb$(001) as well as MnSb has been compared to endotaxial growth of MnSb/GaSb, in which the over-layer grows *into* the substrate, displacing substrate material which then reacts with the incoming beam fluxes.

In conclusion, MnSb growth has been demonstrated on GaAs(111)B and (001) substrates, with high quality surfaces and the anticipated ferromagnetic and metallic properties. The surface structures and reconstructions observed on the MnSb surfaces are of great interest. As a fundamental surface science study they are interesting for their complex surface structure and bonding configurations, in addition to their possible relevance to more complicated materials such as NiMnSb, which has some MnSb terminated surfaces. These surfaces are also important for understanding the formation of high quality inverse hetero interfaces. Finally, growth of MnSb on InP substrates has been studied, and is found to be hindered by the high chemical reactivity of the materials, despite the high degree of lattice matching.

6.2 Future work

The work in this thesis can be conveniently separated into three main areas: commissioning and calibrating the MBE-STM system, growth and characterisation of MnSb over-layers and MnSb surface structures and reconstructions. For each of these areas there are numerous possibilities for future work. At present, the MBE-STM system has the necessary facilities required for growth and study of MnSb, although the lack of in situ chemical analysis is a severe hinderance. Appendix C shows a list of the future improvements to be made to the system.

MnSb was successfully grown on GaAs substrates, but beyond preliminary XRD and magnetic measurements on MnSb(0001)/GaAs(111)B presented in Chapter 3, little bulk characterisation has been possible. Detailed XRD should be carried out in order to determine the crystalline quality of the growth layers (by analysis of the diffraction peak FWHM), in addition to identification of the extra diffraction peaks observed in this work. Similarly, the magnetic properties should be investigated in more detail, and the apparent in-plane magnetic field orientation dependence of the saturation magnetisation checked. A detailed investigation of these two properties may lead to further optimisation of the growth conditions on GaAs(111)B. To date, no XRD or magnetic measurements have been carried out on the MnSb($1\bar{1}01$)/GaAs(001) samples, and this is crucial for unambiguous identification of the growth material and orientation. Since it is the interface which is of most relevance for spin injection purposes, this is an in-

teresting aspect of the MnSb/GaAs system to study. The 3D island formation observed in Chapter 3 should certainly be investigated in more depth, studying how the island nucleation and growth is affected by the growth conditions. This will provide invaluable understanding of how the interface is formed, and potentially how to reduce island density, which in turn may reduce the dislocation density. These STM studies should be accompanied by TEM in order to observe more directly the interface structure, including the lateral thickness of any inter-diffusion region and dislocation density at the interface. One of the more puzzling results in this thesis is the presence of a large Mn layer on the surface of MnSb over-layers grown at low BEP ratios. A more detailed XPS study of this phenomena at the NCESS facility (Daresbury Laboratory, UK) has recently been proposed by this group. Also in the NCESS proposal, a study of MnSb surface preparation after contamination is planned. Determination of an ex situ surface preparation protocol will be important for future ex situ study of MnSb layers such as ion scattering in addition to multiple growth stages in different chambers.

The growth of MnSb on InP resulted in low quality growth due to the chemical reactivity of the MnSb and InP. Further to this work, it would be interesting to study possible methods of reducing or preventing entirely this intermixing. Suggested methods for this include sulphur termination/passivation of the substrate, low temperature growth or multiple stage growth. It would no doubt also be informative to study the initial stages of growth (as demonstrated for MnSb/GaAs(111)B using STM and XPS in this thesis) for the MnSb/InP combination.

The final area for future work is study of the previously unreported surface reconstructions on MnSb surfaces. Only a small number of published papers exist on the surface structures of Mn pnictides, and the majority of these concern MnAs. The NiAs (e.g. MnSb and MnAs) surface structures and reconstruction mechanisms are not well understood, and there is considerable scope for novel work. The MBE-STM system described in this thesis is ideally suited for this investigation since the procedures for preparing the reconstructions have been established, and together the in situ STM, RHEED and XPS will provide considerable information about the reconstructions. The combination of chemical and geometrical information from these techniques should allow more informed models to be proposed. In addition to these experimental techniques, a planned collaboration with Dr S. Jenkins at the University of Cambridge should allow

DFT calculations of any proposed structures.

Bibliography

[1] R.H.O. *Journal of the Franklin Institute*, 246:438, 1948, Accessible with Science Direct.

[2] M. N. Baibich, J. M. Broto, A. Fert, F. Nguyen Van Dau, and F. Petroff. *Phys. Rev. Lett.*, 61(21):2472, 1988.

[3] J. Barnaś, A. Fuss, R. E. Camley, P. Grünberg, and W. Zinn. *Phys. Rev. B*, 42(13):8110, 1990.

[4] R. C. Sousa and I. L. Prejbeanu. *C. R. Physique*, 6:1013, 2005.

[5] S. A. Wolf, D. D. Awschalom, R. A. Buhrman, J. M. Daughton, S. von Molnár, M. L. Roukes, A. Y. Chtchelkanova, and D. M. Treger. *Science*, 294:1488, 2001.

[6] D. Hägele, M. Oestreich, W. W. Rühle, N. Nestle, and K. Eberl. *Appl. Phys. Lett.*, 73(11):1580, 1998.

[7] J. M. Kikkawa and D. D. Awschalom. *Nature*, 397:139, 1999.

[8] S. Datta and B. Das. *Appl. Phys. Lett.*, 56:665, 1990.

[9] M. Ramsteiner, H. Y. Hao, A. Kawaharazuka, H. J. Zhu, M. Kästner, R. Hey, L. Däweritz, H. T. Grahn, and K. H. Ploog. *Phys. Rev. B*, 66:081304, 2002.

[10] H. J. Zhu, M. Ramsteiner, H. Kostial, M. Wassermeier, H.P. Schönherr, and K. H. Ploog. *Phys. Rev. Lett.*, 87(1):016601, 2001.

[11] M. Oestreich, J. Hübner, D. Hägele, P. J. Klar, W. Heimbrodt, , W. W. Rühle, D. E. Ashenford, and B. Lunn. *Appl. Phys. Lett.*, 74(9):1251, 1999.

[12] R. J. Soulen Jr., M. S. Osofsky, B. Nadgorny, T. Ambrose, P. Broussard, S. F. Cheng, J. Byers, C. T. Tanaka, J. Nowack, J. S. Moodera, G. Laprade, A. Barry, and M. D. Coey. *J. Appl. Phys.*, 85(8):4589, 1999.

[13] J.G. Braden, J. S. Parker, , P. Xiong, S. H. Chun, and N. Samarth. *Phys. Rev. Lett.*, 91(5):056602, 2003.

[14] H. Arabia, A. Pourghazi, F. Ahmadian, and Z. Nourbakhsh. *Physica B*, 373:16, 2006.

[15] L. Chioncel, M. I. Katsnelson, R. A. de Groot, and A. I. Lichtenstein. *Phys. Rev B*, 68:144425, 2003.

[16] R. Coehoorn, C. Haas, and R. A. de Groot. *Phys. Rev B*, 31(4):1980, 1985.

[17] R. A. de Groot, F. M. Mueller, P. G. van Engen, and K. H. J. Buschow. *Phys. Rev. Lett.*, 50(25):2024, 1983.

[18] T. Dietl, H. Ohno, F. Matsukura, J. Cibert, and D. Ferrand. *Science*, 287:1019, 2000.

[19] B. T. Jonker, Y. D. Park, , B. R. Bennett, H. D. Cheong, G. Kioseoglou, , and A. Petrou. *Phys. Rev. B*, 62(12):8180, 2000.

[20] R. Fiederling, M. Keim, G. Reuscher, W. Ossau, G. Schmidt, A. Waag, and L. W. Molenkamp. *Nature*, 402:787, 1999.

[21] T. Jungwirth, K. Y. Wang, J. Mašek, K. W. Edmonds, Jürgen König, Jairo Sinova, M. Polini, N. A. Goncharuk, A. H. MacDonald, M. Sawicki, A. W. Rushforth, R. P. Campion, L. X. Zhao, C. T. Foxon, , and B. L. Gallagher. *Phys. Rev. B*, 72:165204, 2005.

[22] J. R. Waldrop and R. W. Grant. *Appl. Phys. Lett.*, 34(10):630, 1979.

[23] M. Nogami, m. Sekinobu, and H. Doi. *Jpn. J. Appl. Phys.*, 3(10):572, 1964.

[24] E. Fred Schubert. *Doping in III-V Semiconductors*. Cambridge University Press, The Pitt Building, Trumpington Street, Cambridge, CB2 1RP, UK, 86th edition, 1993.

[25] G. Schmidt and L. W. Molenkamp. *Semicond. Sci. Technol.*, 17:310, 2002.

[26] R. L. Park and H. H. Madden. *Surf. Sci.*, 11:188, 1968.

[27] E. A. Wood. *J. Appl. Phys.*, 35(4):1306, 1964.

[28] J. F. O'Hanlon. *A User's Guide to Vacuum Technology*. John Wiley & Sons Inc, Hoboken, New Jersey, 2003.

[29] A. Y. Cho and J. R. Arthur. *Prog. Solid State Chem.*, 10:157, 1975.

[30] D. P. Woodruff and T. A. Delchar. *Modern Techniques of Surface Science*. Cambridge University Press, The Edinburgh Building, Cambridge, CB2 2RU, UK, 2nd edition, 1994.

[31] M. A. Herman and H. Sitter. *Molecular Beam Epitaxy- Fundamentals and Current Status*. Springer-Verlag, Berlin, Heidelberg, Germany, 1989.

[32] W. Braun, A. Trampert, V. M. Kaganer, B. Jenichen, D. K. Satapathy, and K. H. Ploog. *MBE2006 conference proceedings: Private comunication, ThB3-2*, 2006.

[33] I. Bonev. *Acta Cryst. A*, 28:508, 1972.

[34] K. Barnham and D. Vvedensky. *Low-Dimensional semiconductor structures- Fundamentals and device applications*. Cambridge University Press, The Edinburgh Building, Cambridge, UK, 2001.

[35] S.A. Hatfield, T.D. Veal, C.F. McConville, G.R. Bell, K.W. Edmonds, R.P. Campion, C.T. Foxon, and B.L. Gallagher. *Surf. Sci*, 585:66, 2005.

[36] D. A. Shirley. *Phys. Rev. B*, 5:4709, 1972.

[37] http://www.phy.cuhk.edu.hk/ surface/XPSPEAK/. accessed 29 Nov 2006.

[38] C. J. Chen. *Introduction to scanning tunneling microscopy*. Oxford University Press, Great Clarendon Street, Oxford, UK, 1993.

[39] V. P. LaBella, H. Yang, D. W. Bullock, P. M. Thibado, Peter Kratzer, and Matthias Scheffler. *Phys. Rev. Lett.*, 83(15):2989, 1999.

[40] P. John, T.Miller, and T.C.Chiang. *Phys. Rev. B*, 39:1730, 1989.

[41] Akihiro Ohtake and Jun Nakamura. *Surf. Sci.*, 396:394, 1998.

[42] M. Björkqvist, M. Göthelid, L. Ö. Olsson, J. Kanski, and U. O. Karlsson. *J. Vac. Sci. Technol. B*, 14(2):957, 1996.

[43] M. Nishizawa, T. Eguchi, T. Misima, J. Nakamura, and T. Osaka. *Phys. Rev. B*, 57:6317, 1998.

[44] C. Kumpf, L. D. Marks, D. Ellis, D. Smilgies, E. Landemark, M. Nielsen, R. Feidenhans'l, J. Zegenhagen, O. Bunk, J. H. Zeysing, Y. Su, and R. L. Johnson. *Phys. Rev. Lett.*, 86:3586, 2001.

[45] T. D. Mishima, N. Naruse, S. P. Cho, T. Kadohira, , and T. Osaka. *Phys. Rev. Lett.*, 89(27):276105, 2002.

[46] M. D. Pashley. *Phys. Rev. B*, 40(15):10481, 1989.

[47] A. Ohtake, J. Nakamura, S. Tsukamoto, N. Koguchi, and A. Natori. *Phys. Rev. Lett.*, 89(20):206102, 2002.

[48] H. F. Franzen, C. Haas, and F. Jellinek. *Phys. Rev. B*, 10(4):1248, 1974.

[49] M. Tanaka, J. P. Harbison, M. C. Park, Y. S. Park, T. Shin, and G. M. Rothberg. *J. Appl. Phys.*, 76(10), 1994.

[50] C. Kittel. *Introduction to Solid State Physics*. John Wiley & Sons Inc, New York, 7th edition.

[51] Jeongyong Choi, Sungyoul Choi, M.H. Sohn, Hyoyeol Park, Yongsup Park, Hyun-Min Park, S.C. Hong, and Sunglae Cho. *J. Magn. Magn. Mater.*, 304:e112, 2006.

[52] F. C. Nascimento, A. O. dos Santos, A. de Campos, S. Gama, and L. P. Cardoso. *Mater. Res.*, 9(1):111, 2006.

[53] R Coehoorn and R A de Groot. *J. Phys. F*, 15:2135, 1985.

[54] Jin-Cheng Zheng and James W. Davenport. *Phys. Rev B*, 69:144415, 2004.

[55] L. Däweritz, F. Schippan, A. Trampert, M. Kästner, G. Behme, Z.M. Wang, M. Moreno, P. Schützendübe, and K.H. Ploog. *J. Cryst. Growth*, 227-228:834, 2001.

[56] F. Schippan, G. Behme, L. Däweritz, K. H. Ploog, B. Dennis, K.-U. Neumann, and K. R. A. Ziebeck. *J. Appl. Phys.*, 88(5):2766, 2000.

[57] M. Tanaka, J. P. Harbison, M. C. Park, Y. S. Park, T. Shin, and G. M. Rothberg. *Appl. Phys. Lett.*, 65(15):1964, 1994.

[58] L. Däweritz, M. Kästner, T. Hesjedal, T. Plake, B. Jenichen, and K.H. Ploog. *J. Cryst. Growth*, 251:297, 2003.

[59] M. Kästner, F. Schippan, P. Schützendübe, L. Däweritz, and K.H. Ploog. *Surf. Sci*, 460:144, 2000.

[60] S. Miyanishi, H. Akinaga, and K. Tanaka. *Appl. Phys. Lett.*, 68:2890, 1996.

[61] H. Tatsuoka, H. Kuwabara, M. Oshita, T. Nakamura, H. Fujiyasu, and Y. Nakanishi. *J. Cryst. Growth*, 166:754, 1996.

[62] B. L. Low, C. K. Ong, J. Lin, A. C. H. Huan, H. Gong, and T. Y. F. Liew. *J. Appl. Phys.*, 85(10), 1999.

[63] M. Kästner, L . Däweritz, and K.H. Ploog. *Surf. Sci.*, 511:323, 2002.

[64] Kanta Ono, Masaki Shuzo, , Masaharu Oshima, and Hiro Akinaga. *Phys. Rev. B*, 64:085328, 2001.

[65] A. Ouerghi, M. Marangolo, M. Eddrief, S. Guyard, V. H. Etgens, and Y. Garreau. *Phys. Rev. B*, 68:115309, 2003.

[66] Oliver Rader, Akio Kimura, Nozomu Kamakura, Ki-Seok An, Akito Kakizaki, Shintaro Miyanishi, Hiroyuki Akinaga, Masafumi Shirai, Kenya Shimada, and Atsushi Fujimori. *J. Electron Spectrosc. Relat. Phenom.*, 88-91:225, 1998.

[67] Yoshito Ashizawa, Shin Saito, and Migaku Takahashi. *J. Appl. Phys.*, 91(10):8096, 2002.

[68] M. Yokoyama, S. Ohya, and M. Tanaka. *App. Phys. Lett.*, 88(012504), 2006.

[69] Y. Morishita, K. Iida, A. Tsuboi, H. Taniguchi, and K. Sato. *J. Cryst. Growth*, 187:228, 1998.

[70] S.X. Liu, S.M. Bedair, and N.A. El-Masry. *Matt. Lett.*, 42:121, 2000.

[71] H. Tatsuoka, H. Kuwabara, M. Oshita, Y. Nakanishi, T. Nakamura, and H. Fujiyasu. *Appl. Surf. Sci.*, 92:382, 1996.

[72] F. Schippan, M. Kästner, L. Däweritz, and K. H. Ploog. *Appl. Phys. Lett.*, 76(7):834, 2000.

[73] L. Däweritz, C. Herrmann, J. Mohanty, T. Hesjedal, K. H. Ploog, E. Bauer, A. Locatelli, S. Cherifi, R. Belkhou, A. Pavlovska, and S. Heun. *J. Vac. Sci. Technol. B*, 23(4):1759, 2005.

[74] A. Ouerghi, M. Marangolo, M. Eddrief, B. B. Lipinski, V. H. Etgens, M. Lazzeri, H. Cruguel, F. Sirotti, A. Coati, and Y. Garreau. *Phys. Rev. B*, 74:155412, 2006.

[75] S. Dushman and A. H. Young. *Phys. Rev.*, 68:278, 1945.

[76] L.C. Cai, H. Chen, C.L. Bao, Q. Huan, and J.M. Zhou. *J. Cryst. Growth*, 197:364, 1999.

[77] J. Sadowski, J. Kanski, L. Ilver, and J. Johansson. *Appl. Surf. Sci.*, 166:247, 2000.

[78] A. J. Noreika, M. H. Francombe, and C. E. C. Wood. *J. Appl. Phys.*, 52(12):7416, 1981.

[79] Kunishige Oe, Seigo Ando, and Koichi Sugiyama. *Jap. J. Appl. Phys.*, 19(7):L417, 1980.

[80] WK. Liu and M.B. Santos. *Surf. Sci.*, 319:172, 1994.

[81] J. Wever, H.L.Meyerheim, W.Moritz, V.Jahns, D.Wolf, H.Schulz, L.Seehofer, and R.L.Johnson. *Surf. Sci.*, 321:L225, 1994.

[82] M.O. Schweitzer, F.M. Leibsle, T. S. Jones, C.F. McConville, and N.V. Richardson. *Surf. Sci*, 280:63, 1993.

[83] C. F. McConville, T. S. Jones, F. M. Leibsle, S. M. Driver, T. C. Q. Noakes, M. O. Schweitzer, and N. V. Richardson. *Phys. Rev. B*, 50(20):14965, 1994.

[84] A.A. Cafolla, C. McGinley, E. McLaughlin, G. Hughes, P. Moriarty, A.W. Dunn, Y.-R. Ma, D. Teehan, B. Murphy, S. Downes, and D.A. Woolf. *Surf. Sci.*, 377-379:130, 1997.

[85] A. U. Mac Rae. *Surf. Sci.*, 4:247, 1966.

[86] W. Ranke and K. Jacobi. *Surf. Sci.*, 63:33, 1977.

[87] N. W. Ashcroft and N. D. Mermin. *Solid State Physics*. CBS Publishing, West Washington Square, Philadelphia, PA 19105, 1988.

[88] J. R. Hook and H. E. Hall. *Solid State Physics*. J. Wiley and Sons, Baffins Lane, Chichester, West Sussex, PO19 1UD, 2nd edition, 2001.

[89] S. A. Chambers, T. Droubay, T. C. Kaspar, and M. Gutowski. *J. Vac. Sci. Technol. B*, 22(4):2205, 2004.

[90] Y. Hirota and K. Sumitomo. *J. Appl. Phys.*, 79(10):7785, 1996.

[91] H. Akinaga, S. Miyanishi, W. Van Roy, and L. H. Kuo. *Appl. Phys. Lett*, 70(18):2472, 1997.

[92] http://www.nist.gov/srd/nist71.htm. accessed 29 Nov 2006.

[93] P. Drathen, W. Ranke, and K. Jacobi. *Surf. Sci.*, 77:L167, 1978.

[94] Q. Xue, T. Hashizume, J. M. Zhou, T. Sakata, T. Ohno, and T. Sakurai. *Phys. Rev. Lett.*, 74:3177, 1995.

[95] H. Akinaga, S. Miyanishi, W. Van Roy, J. De Boeck, and G. Borghs. *Appl. Phys. Lett.*, 73(22):3285, 1998.

[96] R.M. Stroud, A.T. Hanbicki, Y. D. Park, G. Kioseoglou, A.G. Petukhov, , B.T. Jonker, G. Itskos, and A. Petrou. *Phys. Rev. Lett.*, 89(16):166602, 2002.

[97] Igor Žutić, Jaroslav Fabian, and S. Das Sarma. *Rev. Mod. Phys.*, 76:323, 2004.

[98] C. D. Lee, Y. Dong, R. M. Feenstra, J. E. Northrup, and J. Neugebauer. *Phys. Rev. B*, 68(205317), 2003.

[99] D. K. Biegelsen, R. D. Bringans, J. E. Northrup, and L. E. Swartz. *Phys. Rev. Lett.*, 65:452, 1990.

[100] A.R. Smith, R.M. Feenstra, D.W. Greve, M.-S. Shin, M. Skowronski, J. Neugebauer, and J.E. Northrup. *Surf. Sci*, 423:70, 1999.

[101] T. Abukawa, M. Sasaki, F. Hisamatsu, M. Nakamura, Toyohiko Kinoshita, A. Kakizaki, T. Goto, and S. Kono. *J. Electron Spectrosc. Relat. Phenom.*, 80:233, 1996.

[102] S. J. Jenkins. *Phys. Rev. B*, 70:245401, 2004.

[103] O Rader, M Ležaić, S Blügel, A Fujimori, A Kimura, N Kamakura, A Kakizaki, S Miyanishi, and H Akinaga. *New Journal of Physics*, 7:111, 2005.

[104] P.M. Thibado, B.R. Bennett, B.V. Shanabrook, and L.J. Whitman. *J. Cryst. Growth*, 175:317, 1997.

[105] H. W. Nesbitt and M. Reinke. *Am. Mineral.*, 84:639, 1999.

[106] Takeshi Kikawa, Isao Ochiai, and Shinichiro Takatani. *Surf. Sci.*, 316:238, 1994.

[107] H. Bando, H. Yoshinoa, H. Okamotoa, and K. Iizuka. *J. Cryst. Growth*, 278:464, 2005.

[108] J.B. Malherbe and W.O. Barnard. *Surf. Sci.*, 255:309, 1991.

[109] T. Chassé, H. Peisert, P. Streubel, and R. Szargan. *Surf. Sci.*, 331-333:434, 1995.

[110] J. Jin and L. J. Lewis. *Surf. Sci.*, 325:251, 1995.

[111] M.M. Sung, C. Kim, H. Bu, D.S. Karpuzov, and J.W. Rabalais. *Surf. Sci.*, 322:116, 1995.

[112] C. D. MacPherson, R. A. Wolkow, C. E. J. Mitchell, and A. B. McLean. *Phys. Rev. Lett.*, 77(4):691, 1996.

[113] W. G. Schmidt and F. Bechstedt. *Surf. Sci.*, 409:474, 1998.

[114] Xavier Wallart. *Surf. Sci.*, 506:203, 2002.

[115] T. Wojtowicz, W.L. Lim, X. Liu, G. Cywiéski, M. Kutrowskia, L.V. Titova, K. Yee, M. Dobrowolska, J.K. Furdyna, K.M. Yu, W. Walukiewicz, G.B. Kim, M. Cheon, X. Chen, S.M. Wang, H. Luo, I. Vurgaftman, and J.R. Meyer. *Physica E*, 20:325, 2004.

[116] S. Yanagi, K. Kuga, T. Slupinski, and H. Munekata. *Physica E*, 20:333, 2004.

[117] F. R. de Boer, R. Boom, and A. R. Miedema. *Physica B*, 113:18, 1982.

[118] *CRC handbook of chemistry and physics*. Taylor and Francis, London, UK, 86th edition, 2005.

[119] J. C. Ferrer, F. Peiro, A. Cornet, J. R. Morante, T. Uztmeier, G. Armelles, and F. Briones. *Appl. Phys. Lett.*, 69:3887, 1996.

[120] A. Godefroy, S. Ababou, B. Lépine, A. Guivarc'h, and G. Jézéquel. *J. Cryst. Growth*, 179:349, 1997.

[121] Y. Sun, S.F. Cheng, G. Chen, R.L. Woo, and R.F. Hicks. *J. Appl. Phys.*, 97:103512, 2005.

Appendix A

Growth rate equation

In order to theoretically obtain the growth rate for a material, a modified version of the rate equation presented by Woodruff and Delchar [30] is used. The modification arises from the highly uni-directional velocity distribution of a beam flux. The rate of arrival of a gas, density n, with average velocity in the x direction $< v_x >$ is given by

$$r = n < v_x > \tag{A.1}$$

For an isotropic gas, as described by Woodruff and Delchar, with equal x, y and z distribution of velocity.

$$< v_x >= \frac{< v >}{4} \tag{A.2}$$

However, in the case of molecular beam fluxes, the movement of the atoms are taken to be almost exclusively in the positive x direction, and hence

$$< v_x >=< v > \tag{A.3}$$

The average velocity v may be expressed as an integral over the velocity distribution function $f(v)$, which is itself described by a Maxwell Boltzmann distribution

$$< v >= \int_0^\infty v f(v) dv \tag{A.4}$$

$$< v >= \int_0^\infty 4\pi \left(\frac{m}{2\pi k_{\mathrm{B}} T} \right)^{3/2} v^3 \exp\left(\frac{-mv^2}{2k_{\mathrm{B}} T} \right) dv \tag{A.5}$$

This can be solved by changing variable to $u = v^2$ and integrating by parts. The result is

$$< v >= \left(\frac{8k_{\mathrm{B}} T}{m\pi} \right)^{1/2} \tag{A.6}$$

The final equation required is the ideal gas law

$$P = nk_{\mathrm{B}} T \tag{A.7}$$

Combining equations A.1, A.3, A.6 and A.7

$$r(m^{-2}s^{-1}) = \frac{4}{\sqrt{2\pi}} \frac{P}{\sqrt{k_{\mathrm{B}}Tm}} \tag{A.8}$$

This differs by only a factor of 4 from the isotropic version of Woodruff and Delchar, indicating that for the same BEP measured by an ion gauge, the arrival rate at the sample is higher since the majority of the molecules are travelling towards the sample.

For a material which depends upon the arrival rate of only one species which has a BEP $= P$, the growth rate (GR) may be expressed

$$GR = rV_0 \tag{A.9}$$

Here V_0 is the volume per formula unit. Hence

$$GR = \frac{4}{\sqrt{2\pi}} \frac{PV_0}{\sqrt{k_{\mathrm{B}}Tm}} \tag{A.10}$$

In which all values are in SI units. A more convenient form of the equation is

$$GR = 10.9 \times 10^7 \frac{V_0 P_{\mathrm{mbar}}}{\sqrt{T_{\mathrm{K}} M_{\mathrm{amu}}}} [\mathrm{nm\ min^{-1}}] \tag{A.11}$$

where V_0 is in $\mathring{A}^3$.

Appendix B

RHEEDprofile.m

```
%RHEEDprofile.m
%by STUART HATFIELD
%Sept 2006
%Program for Matlab 6.1
%Program for measuring RHEED streak spacing from jpg images
%INSTRUCTIONS FOR USE
%Place jpg image in location
%C:\MATLAB6p5\work\imageprofileimages\IMAGE.jpg
%or change location in program as appropriate.
%1). Run program
%2). On image, click with mouse three times. The first click
% defines the center of the line scan(horizontal position)
% and the height of the first line scan (vertical position),
% while the second and third indicate the left and right ends
% of the reference distance
%3). The RHEED profile will appear. Zoom into relevant area with mouse,
%then press return.
%4). Click on four peaks in order. Output gives the distance
%between consecutive peaks (d1-d3), and the average (dav) in mm.


clear;
%VARIABLES
%Program sums over a number of consecutive linescans. Set number here
scanno=40
%Program uses a reference distance in the image for calibration. Set the
```

```
%calibration distance here (in mm). Value of 150mm set is for the diameter
%of the RHEED screen flange
featureref=150


%The program
%Reads in jpg image at a location
%C:\MATLAB6p5\work\imageprofileimages\IMAGE.jpg
%Change as applicable
I= imread('C:\MATLAB6p5\work\imageprofileimages\IMAGE.jpg');
%Shows image
figure(1); subplot(1,1,1); imshow(I);
%Calculates the size of the file
widthtemp=size(I); width=widthtemp(2);
 heighttemp=size(I); height=widthtemp(1);
%Allows for three mouse operated inputs. Click on the
%screen three times
%Click 1=Sets Centre (horizontal position) and
%height (vertical distance) of the line scan
%Click 2=left end of the reference distance
%Click 3=right end of reference distance
[x,y]=ginput(3);
%Sets the relevant positions
linestart=fix(y(1)); zero=fix(x(1))
%calculates the reference distance
ref=abs(x(3)-x(2));

%Extracts the consecutive line scans. Program only
%scans the middle third to improve speed
for scan=1:scanno
    line= linestart+scan
    for i=fix(width/3):fix(width*2/3)
```

```
%Converts from uint8 to double precision and puts
% intensities at each point in the nxmx3 matrix RGB
         for c=1:3;
             Iline=I(line,i,c);
             RGB(i,c)=double(Iline);
         end
    end
     %Extracts the green component of the image
    for i=fix(width/3):fix(width*2/3)
        intensity(scan,i,2)=RGB(i,2);
    end
    %Calibrates the x axis
    for i=fix(width/3):fix(width*2/3)
        intensity(scan,i,1)=(i-zero)*featureref/ref;
    end
end
%Sums all the scans
 for i=fix(width/3):fix(width*2/3)
     intensitysum(i,2)=sum(intensity(:,i,2));
     intensitysum(i,1)=intensity(1,i,1);
 end

%Plots the scan.
figure(2);
 hold on;
  plot(intensity(1,fix(width/3):fix(width*2/3),1)
  ,intensitysum(fix(width/3):fix(width*2/3),2));

hold off
%Pause the program to allow the image to be zoomed. Resume by pressing
%enter
pause
```

```
%Four more mouse outputs. Click on the peaks in order. Program calculates
%the distance between consecutive clicks, and an average dav. These numbers
%are shown on the output
[x,y]=ginput(4); d1=abs(x(2)-x(1)) d2=abs(x(3)-x(2))
d3=abs(x(4)-x(3)) dav=(d1+d2+d3)/3
```

Appendix C

MBE-STM system tasks

The following tasks require attention on the MBE-STM system.

Vacuum system

- Safety interlocks and valves should be set up to protect the system against power cuts, venting and loss of water cooling.
- The bakeout procedures and filament degassing should be optimised, to improve base pressures of the chambers.
- Methods of sample transfer to/from the vacuum system under nitrogen should be developed.

MBE chamber

- Cell shutters require strengthening to prevent them from bending during pneumatic operation. The pneumatic shutter control should be implemented and automated.
- The substrate heater design needs modifying. At present the filament has a very short lifetime. In addition, light pollution onto the RHEED screen is considerable, and should be reduced.
- A fourth effusion cell needs adding (Ni or Cr).
- An Sb_4 cell with cracker (Sb_2 and Sb) should be designed and built.

STM chamber

- The XPS system should be fixed. Currently no counts are obtained despite all components being checked individually. The X-ray gun is suspected.

- Improved sample storage needs to be designed.
- Build and fit heating and cooling bays for sample plates to allow for new sample treatment and rapid quenching to be achieved to prevent STM drift.